



저작자표시-비영리-동일조건변경허락 2.0 대한민국

이용자는 아래의 조건을 따르는 경우에 한하여 자유롭게

- 이 저작물을 복제, 배포, 전송, 전시, 공연 및 방송할 수 있습니다.
- 이차적 저작물을 작성할 수 있습니다.

다음과 같은 조건을 따라야 합니다:



저작자표시. 귀하는 원저작자를 표시하여야 합니다.



비영리. 귀하는 이 저작물을 영리 목적으로 이용할 수 없습니다.



동일조건변경허락. 귀하가 이 저작물을 개작, 변형 또는 가공했을 경우에는, 이 저작물과 동일한 이용허락조건하에서만 배포할 수 있습니다.

- 귀하는, 이 저작물의 재이용이나 배포의 경우, 이 저작물에 적용된 이용허락조건을 명확하게 나타내어야 합니다.
- 저작권자로부터 별도의 허가를 받으면 이러한 조건들은 적용되지 않습니다.

저작권법에 따른 이용자의 권리는 위의 내용에 의하여 영향을 받지 않습니다.

이것은 [이용허락규약\(Legal Code\)](#)을 이해하기 쉽게 요약한 것입니다.

[Disclaimer](#)

공학박사학위논문

**디젤 엔진의 배기재순환가스 분포의
불균일성을 고려한 연소 모델 개발**

**The Flamelet Combustion Model for Stratified EGR
Distribution in a Diesel Engine**

2013 년 8 월

서울대학교 대학원

기계항공공학부

박 원 아

디젤 엔진의 배기재순환가스 분포의 불균일성을 고려한 연소 모델 개발

The Flamelet Combustion Model for Stratified EGR
Distribution in a Diesel Engine

지도교수 민 경 덕

이 논문을 공학박사 학위논문으로 제출함

2013년 8월

서울대학교 대학원

기계항공공학부

박 원 아

박원아의 공학박사 학위논문을 인준함

2013년 8월

위원장 고 상 근 (인)

부위원장 민 경 덕 (인)

위 원 윤 영 빈 (인)

위 원 송 한 호 (인)

위 원 이 진 욱 (인)

Acknowledgements

This project on my Ph.D thesis would not be happened without the advices and helps of following people.

First and foremost, I would like to express my respect and gratitude to my advisor, Professor Kyoungdoug Min. During the graduate course, my knowledge and personality were grown up with his invaluable advices. He gave the inspirations of this study and his guidance and encouragement were the source of power overcoming many difficulties during the project.

I would like to special thanks to the project members who offered assistance, valuable discussions and beautiful memories of friendship. Joohan Kim and Gyujin Kim assisted lots of the study. Dr. Sangyul Lee also gave basic knowledge and inspirations as a senior. This work would never have been achieved without their efforts and patients. Also, I'd like to thanks to all of my graduate schoolmates for unforgettably joyful lab life.

I would like to present my deepest respect and gratitude to my parents, Jinwoo Park and Sungyeon Kim, for their great sacrifice, thoughtful consideration, unimaginable patience, and endless love. My sister and brothers, Haein Park, Hojin Park, and Jaebok Kim, were my emotional anchor. And my adorable nephew, Jeongheon Kim, gave me the pleasure of life during the run-up to thesis. It was, it is, and it will be the greatest happiness in my life to be with my family.
I love you.

Abstract

The Flamelet Combustion Model for Stratified EGR Distribution in a Diesel Engine

Wonah Park

Department of Mechanical and Aerospace Engineering

The Graduate School

Seoul National University

Numerous researches have been devoted to reducing NO_x and soot simultaneously in Diesel engines. New combustion concepts to minimize NO_x and soot are low temperature combustion and in-cylinder EGR stratification. Among variable research tools, 3-D CFD has been an essential tool in the engine researches as it can describe combustion processes which are not directly accessible from experiments, on a physical basis.

To study the potential emission reduction from the new combustion concepts by adopting the CFD analysis, it is important to make an accurate prediction of the emission formation. Therefore, a combustion model which can consider the local equivalence ratio caused by the non-uniform EGR distribution and the chemical mechanism for a fuel and formation of emissions in a Diesel engine is needed. A flamelet model is a good tool for better NO_x and soot prediction as it can use chemical mechanisms but it cannot consider the non-uniform EGR distribution such as in-cylinder EGR stratification. Therefore, in this study, a new combustion model -Flamelet for Stratified EGR (FSE) model-

was developed to consider the non-uniform in-cylinder gas distribution based on the chemical kinetics. Then, the FSE model was used to investigate the potential of in-cylinder EGR distributions for simultaneous reduction of NO_x and soot.

The concept of the FSE model is utilizing multiple flamelet models based on the multi-zone concept. To describe this non-uniform gas distribution, the combustion chamber is divided into several zones by oxygen concentration at SOI. Then, the flamelet equations are solved at the boundary of each zone. Final species mass fraction of each cell is calculated by linear interpolation between two results from the boundaries. Consequently, the FSE model has the advantages of the flamelet model for emission prediction; moreover, the FSE model can describe the non-uniform EGR distribution which cannot be described by the conventional flamelet model. The FSE model was validated under variable engine operating conditions including in-cylinder EGR stratification conditions and the model showed good agreement with the experimental results.

The potential of in-cylinder EGR stratification for emission reduction was also studied by using the FSE model. The objective of the EGR stratification was to reduce the NO_x and soot simultaneously in a Diesel engine by separating the external EGR gas and fresh air in the combustion chamber. Therefore, in this study, the combustion systems such as intake ports, chamfers, and a piston were optimized to achieve the favourable EGR distribution and to enhance the effect of in-cylinder EGR stratification. To investigate the potential of the in-cylinder EGR stratification flow and combustion simulations were carried out using the FSE model and the optimized geometries. The effect of the in-cylinder EGR stratification on NO_x and soot emission reduction was verified under the various injection timings, engine speeds, and loads. Although the levels of emission reduction were different, both NO_x and soot were simultaneously reduced under

the stratified EGR condition. From these results, the potential of in-cylinder EGR stratification for the simultaneous NO_x and soot reduction was confirmed.

Keywords: non-uniform EGR distribution, in-cylinder EGR stratification, flamelet model, NO_x emission, soot emission, Diesel engine

Student Number: 2007-22981

Chapter 1. Introduction	1
1.1 Background and Motivation.....	1
1.1.1 Emission regulations.....	1
1.1.2 Previous researches for reducing emissions	2
1.2 In-cylinder EGR Stratification.....	9
1.2.1 Concept of in-cylinder EGR stratification	9
1.2.2 Previous research about in-cylinder EGR stratification.....	10
1.2.3 Numerical approach as an engine development tool	11
1.3 The Need of the Combustion Model for Stratified EGR Distribution	17
1.4 Objectives	23
 Chapter 2. Combustion and Emission Models Review.....	 24
2.1 Turbulence Model.....	24
2.1.1 Governing equations	24
2.1.2 Turbulence model	25
2.2 Laminar Flamelets	28
2.2.1 Laminar flamelet model.....	28
2.2.2 RIF model	30
2.3 Models for Liquid Droplets	34
2.3.1 Lagrangian multi-phase model	34
2.3.2 Droplet break-up model.....	35
2.4 Models for Chemical Mechanics and Emissions	38

2.4.1 Fuel mechanism	38
2.4.2 NOx model.....	38
2.4.3 Soot model.....	38
Chapter 3. Combustion Model for Stratified EGR Distribution in a Diesel Engine.....	47
3.1 Concept of the FSE Model.....	47
3.1.1 Concept of the FSE model	47
3.1.2 Strategy for dividing zones	49
3.1.3 Optimization and validation of the zone strategy	51
3.2 Verification of the Flamelet Model.....	60
3.2.1 Experimental and computational setup.....	60
3.2.2 Results and discussion	62
3.2.3 Comparison between the FSE model and the flamelet model	63
3.3 Verification of the FSE Model	79
3.3.1 Experimental and computational setup.....	79
3.3.2 Results and discussion	80
Chapter 4. Application of the FSE Model	89
4.1 Implementation of In-cylinder EGR Stratification to a Diesel Engine	89
4.2 Hardware Optimization.....	98
4.2.1 Intake port optimization.....	98
4.2.1 Piston optimization	100
4.3 Potential of In-cylinder EGR stratification.....	118

4.3.1 Computational Setup.....	118
4.3.2 Results and Discussion	118
Chapter 5. Conclusions	135
References.....	138
초 록	146

List of Tables

Table 1.1.1 EU Emission Standards for Passenger Cars [17].	4
Table 2.1.1 Coefficients of the RNG $k - \varepsilon$ Turbulence Model [61].	27
Table 2.4.1 Reactions for n-heptane [75].	41
Table 2.4.2 Reactions for NO _x [77].	44
Table 3.2.1 Engine specifications.	65
Table 3.2.2 FIE specifications.	65
Table 3.2.3 The principle of measurement by the emission analyzer.	66
Table 3.2.4 The specifications of the smoke meter.	66
Table 3.2.5 The specifications of the DMS-500.	67
Table 3.2.6 The specifications of the AFR analyzer.	68
Table 3.2.7 The specifications of the in-cylinder pressure transducer.	68
Table 3.2.8 The specifications of the intake port pressure transducer.	69
Table 3.2.9 The specifications of analog inputs of DAQ board.	69
Table 3.2.10 The sub-models for CFD simulations [61].	70
Table 3.2.11 The conditions for validation.	70
Table 3.3.1 Engine Specifications [28, 90].	81

Table 3.3.2 FIE (Fuel injection equipment) Specifications [28, 90].	81
Table 3.3.3 Dynamometer specifications [28, 90].....	82
Table 4.3.1 The sub-models for CFD simulations.....	122
Table 4.3.2 The conditions for calculation.	122

List of Figures

Figure 1.1.1 Trend and comparison of worldwide exhaust emission standards [18].....	5
Figure 1.1.2 Diesel combustion: conceptual model.	6
Figure 1.1.3 NO and soot formation mechanism in a Diesel engine during mixing controlled combustion phase [5].....	7
Figure 1.1.4 The effects of EGR on NO _x and soot emissions in Diesel engines.	8
Figure 1.2.1 Desired in-cylinder EGR stratification and spray targeting [23]. ..	15
Figure 1.2.2 Concept of NO _x -soot simultaneous reduction by stratified EGR [22].....	16
Figure 1.3.1 Schematic diagram of EGR system in a turbocharged Diesel engine (a) High pressure loop EGR and (b) Low pressure loop EGR [59].	19
Figure 1.3.2 The deviation of cylinder by cylinder EGR rate [60].....	20
Figure 1.3.3 EGR distribution in the combustion chamber under conventional engine intake system.....	21
Figure 1.3.4 EGR distribution in the combustion chamber under EGR stratification system.	22
Figure 2.2.1 Mixing behind a splitter plate for a two-feed system [71]	31
Figure 2.2.2 Surface of stoichiometric mixture in a turbulent jet [46].....	32

Figure 2.2.3 Structure of the RIF model.....	33
Figure 2.4.1 Schematic diagram of the steps in the soot formation process [80].	45
Figure 2.4.2 Schematic of the ten-step phenomenological soot model.	46
Figure 3.1.1 Combustion chamber which is divided zones by oxygen concentration.....	53
Figure 3.1.2 The procedure of calculating the combustion model for non- uniform EGR distribution.	54
Figure 3.1.3 Measured NO _x according to the oxygen concentration under conventional Diesel engine operating conditions.	55
Figure 3.1.4 Predicted NO _x according to the oxygen concentration under variable EGR rate at the condition of 2000 rpm bmep 6 bar.	56
Figure 3.1.5 Artificially distributed oxygen in the combustion chamber for optimizing the number of zones.....	57
Figure 3.1.6 Pressure, Temperature, and NO _x according to CAD under variable number of zones.....	58
Figure 3.1.7 Calculation time during 60 CAD of simulation, total elapsed time (calculation time for STAR-CD and FSE code) and CFD time (calculation time for STAR-CD).....	59
Figure 3.2.1 A four-cylinder Diesel engine.	71

Figure 3.2.2 The Computational grid with the two-step piston at BDC (1/8 sector).	72
Figure 3.2.3 Pressure curves as a function of the CAD of the predicted result and measured data.	73
Figure 3.2.4 Comparison of the predicted results with measured data: NO.....	74
Figure 3.2.5 Comparison of the predicted results with measured data: soot mass density (top) and soot number density (bottom).	75
Figure 3.2.6 The computational grid (a) at BDC with intake and exhaust ports (b) at TDC without ports.	76
Figure 3.2.7 Oxygen distribution in the combustion chamber at 10 ° BTDC.	77
Figure 3.2.8 CO ₂ , NO _x , and soot distributions of the FSE model and the flamelet model.	78
Figure 3.3.1 Single cylinder Diesel engine [28, 90].	83
Figure 3.3.2 Picture (left) and simple figure (right) of intake runner [28, 90]. ..	84
Figure 3.3.3 EGR supply methods: conventional EGR (B-EGR, up) and stratified EGR (S-EGR, down) [28, 90].	85
Figure 3.3.4 The Computational grid with the two-step piston at BDC.	86
Figure 3.3.5 Comparison of the predicted results with measured data: NO _x (top) and soot mass density (bottom).	87
Figure 3.3.6 Comparison of the predicted results with measured data: the effect of in-cylinder EGR stratification.	88

Figure 4.1.1 Top view of Diesel engine and the EGR supply method [22].	92
Figure 4.1.2 Shape of one over seven sector mesh (a) conventional piston (b) two-step piston [22].	93
Figure 4.1.3 EGR distributions of each EGR case: (a) conventional piston, (b) two-step piston [22].	94
Figure 4.1.4 NO and soot reduction under Ideal S-EGR condition [22].	95
Figure 4.1.5 Change of the chamfer [90]	96
Figure 4.1.6 Droplet distributions: (a) the conventional piston and (b) the two-step piston [22].	97
Figure 4.2.1 The concept of intake ports optimization.	103
Figure 4.2.2 Velocity distribution at ABDC 90 °.	104
Figure 4.2.3 Parameters of ports and chamfers optimization.	105
Figure 4.2.4 Geometries of the intake ports (a) helix shape (b) non-helix shape.	106
Figure 4.2.5 CO ₂ (EGR) distributions at 10 ° BTDC (helix shape port).	107
Figure 4.2.6 Velocity distribution at 270 ° BTDC (helix shape port).	108
Figure 4.2.7 CO ₂ (EGR) distributions at 10 ° BTDC (non-helix shape port).	109
Figure 4.2.8 EGR distributions of (a) conventional piston and (b) two-step piston [22, 90].	110

Figure 4.2.9 Comparison of the swirl ratio [23].....	111
Figure 4.2.10 Parameters of the piston optimization.....	112
Figure 4.2.11 Piston Geometries (a) Standard Piston, (b) Piston A, (c) Piston B, and (d) Piston C.....	113
Figure 4.2.12 CO ₂ (EGR) distributions at 10 ° BTDC.....	114
Figure 4.2.13 Comparisons of the swirl ratio.....	115
Figure 4.2.14 The method of Air and EGR supply: (a) B-EGR, (b) S-EGR.	116
Figure 4.2.15 Effect of pistons on emission reduction.....	117
Figure 4.3.1 The optimized computational grid: (a) at BDC with intake and exhaust ports, (b) at TDC without ports.....	123
Figure 4.3.2 EGR distributions at 10 ° BTDC: (a) B-EGR, (b) S-EGR.....	124
Figure 4.3.3 In-cylinder pressure curves of B-EGR and S-EGR.....	125
Figure 4.3.4 Averaged in-cylinder temperature curves of B-EGR and S-EGR.	126
Figure 4.3.5 Temperature distributions at 15 ° after SOI (10° ATDC).....	127
Figure 4.3.6 NO distributions at 15 ° after SOI (10° ATDC).....	128
Figure 4.3.7 Comparison of predicted emissions of B-EGR and S-EGR at EGR 25 % condition.....	129
Figure 4.3.8 Soot mass density curves of B-EGR and S-EGR at EGR 25 % condition.	130

Figure 4.3.9 Comparison of predicted emissions of B-EGR and S-EGR at EGR 35 % condition.....	131
Figure 4.3.10 Soot mass density curves of B-EGR and S-EGR at EGR 35 % condition.....	132
Figure 4.3.11 Comparison of predicted emissions of B-EGR and S-EGR under variable injection timings.....	133
Figure 4.3.12 EGR distribution at 10 ° BTDC at S-EGR.....	134
Figure 4.3.13 Comparison of predicted emissions of B-EGR and S-EGR under variable speed and load conditions.....	134

Acronym

AFR	Air Fuel Ratio
ATDC	After Top Dead Center
BDC	Bottom Dead Center
B-EGR	Base EGR
BMEP	Brake Mean Effective Pressure
BTDC	Before Top Dead Center
CAD	Crank Angle Degree
CFD	Computational Fluid Dynamics
DI	Direct Injection
DPF	Diesel Particulate Filter
ECU	Engine Control Unit
EGR	Exhaust Gas Recirculation
FIE	Fuel Injection Equipment
HSDI	High Speed Direct Injection
IVC	Intake Valve Close
IVO	Intake Valve Open
LTC	Low Temperature Combustion
PM	Particulate Matter
S-EGR	Stratified EGR
SND	Soot number density
TDC	Top Dead Center
U-EGR	Uniform EGR

Chapter 1. Introduction

1.1 Background and Motivation

1.1.1 Emission regulations

Current engine research is focused on reducing exhaust emissions and improving fuel economy, due to increased environmental concerns and strict government regulations on exhaust emission standards, and increased prices of petroleum-based fuels. A high speed direct injection (HSDI) Diesel engine is gaining recognition due to potential for realization of low emissions and high fuel conversion efficiency. Recent HSDI Diesel engine achieved higher specific power and fuel conversion efficiency than previous engines by using advanced injection and charge system such as common rail system, piezo injector, turbocharger, and intercooler [1-3]. However, the HSDI Diesel engine exhausts more pollutants particularly nitrogen oxides (NO_x) and soot; such that consumers and environmental groups have requested stronger regulations on the legal emissions. In response, governments are introducing stricter environmental regulations as shown in Figure 1.1.1. The representative regulation is European emissions legislation called Euro. The suggested Euro VI will put the law into effect in 2014. According to Euro VI, NO_x should be reduced by 55.6 %, while soot has to be maintained compared to the Euro V level (Table 1.1.1).

There are two methods to reduce emissions: using after-treatment systems and lessening engine-out emissions. Spark ignition (SI) engines could solve the most problems using 3-way catalyst system. Unlike SI engines, 3-way catalyst cannot be applied to Diesel engines, because of its lean combustion conditions. There are several after-treatment systems for Diesel engines reducing NO_x and soot, such as a

Diesel Particulate Filter (DPF), Lean NOx Trap (LNT), NOx Storage Catalyst (NSC), and Selective Catalytic Reduction (SCR). These after-treatment systems can increase the cost of the vehicle, complicate the exhaust system and increase the weight of the vehicle [4]. Therefore, the second method is more efficient at reducing emissions with little or no additional cost or systems required. Therefore, it is important to find a way to reduce NOx and soot in the combustion chamber.

1.1.2 Previous researches for reducing emissions

NOx and soot emissions of Diesel engines form due to high flame temperature and nonhomogeneous distribution of fuel spray. Most of NOx emissions produce by thermal NOx reaction in the high-temperature burned gas region as shown in Figure 1.1.2 and Figure 1.1.3. Moreover, its formation rate is the highest near the stoichiometric region ($\phi = 1$), and depends strongly on the flame temperature and oxygen concentration. Because NOx reaction rate is slower than combustion reaction rate, NOx can be reduced with keeping combustion gas temperature low after combustion process. On the other hand, soot is made in the fuel-rich and oxygen-lean region ($\phi = 4 \sim 5$). After that, soot is oxidized as air mixed with the soot rich region, and soot oxidation rate also depends on the gas temperature. For this reason, there is trade-off relation between NOx and soot at conventional Diesel engines [5].

Exhaust Gas Recirculation (EGR) is one of the key factors that influence on the emission characteristics of Diesel engines because the EGR changes the combustion parameters such as ignition delay, flame temperature, combustion speed, etc. The effects of EGR can be explained as follows [6-10].

- The thermal effect: The heat capacity of in-cylinder charge increases by using EGR due to higher specific heat capacity of re-circulated CO₂ and H₂O than O₂ and N₂. So, the flame temperature is lowered during the combustion.

- The dilution effect: EGR dilute in-cylinder charge because it drops Air to Fuel Ratio (AFR). All of the combustion process is delayed with diluted in-cylinder gas (ignition delay, premixed combustion, diffusion and late diffusion combustion). The prolonged ignition delay increases the proportion of the premixed combustion. Moreover, the gas quantity that absorbs the heat release is increasing, resulting in a lower the burned gas temperature.

- The chemical effect: The re-circulated H_2O and CO_2 are dissociated during the combustion, modifying the combustion process in particular, the endothermic dissociation of H_2O decreases flame temperature.

Therefore, EGR is an effective way for reducing NO_x emission at conventional Diesel engines, which lowers the combustion temperature. However, the amount of soot formation increases because EGR reduces the oxygen concentration, burned gas temperature, and generates local rich area in conventional engine operating conditions (Figure 1.1.4).

Although there have been many studies on reducing Diesel engine emissions, it is difficult to diminish NO_x and soot simultaneously in conventional Diesel engines. To overcome this problem, Low Temperature Combustion (LTC) concepts have been studied, including Homogeneous Charge Compression Ignition (HCCI) [11-14], the smokeless-rich Diesel combustion [15], and the modulated kinetics (MK) combustion [16]. There are some differences in adapting the LTC concept, but creating a low combustion temperature through high EGR and obtaining the premixed condition through particular injection strategies are common characteristics. The LTC concept has a high potential to reduce NO_x and soot, but there are also many limitations to commercialization due to narrow operating ranges and difficulties in ignition control. The problems of LTC concept come from using high EGR ratio. Therefore, new combustion concept which can control AFR and flame temperature is necessary to reduce NO_x and soot emissions simultaneously.

Table 1.1.1 EU Emission Standards for Passenger Cars [17].

Stage	Date	CO	HC+NO _x	NO _x	PM	PN
		g/km				#/km
Euro 1†	1992.07	2.72 (3.16)	0.97 (1.13)	-	0.14 (0.18)	-
Euro 2, IDI	1996.01	1.0	0.7	-	0.08	-
Euro 2, DI	1996.01 ^a	1.0	0.9	-	0.10	-
Euro 3	2000.01	0.64	0.56	0.50	0.05	-
Euro 4	2005.01	0.50	0.30	0.25	0.025	-
Euro 5a	2009.09 ^b	0.50	0.23	0.18	0.005 ^d	-
Euro 5b	2011.09 ^c	0.50	0.23	0.18	0.005 ^d	6.0×10 ¹¹
Euro 6	2014.09	0.50	0.17	0.08	0.005 ^d	6.0×10 ¹¹

† Values in brackets are conformity of production (COP) limits

a. until 1999.09.30 (after that date DI engines must meet the IDI limits)

b. 2011.01 for all models

c. 2013.01 for all models

d. 0.0045 g/km using the PMP measurement procedure

Global Regulation Timeline by Region							
	2008	2009	2010	2011	2012	2013	2014
U.S.	Locomotive & Marine Tiers 0-2	CA CVS Retrofit**	US-10 CVS On-highway Motorcycle Rule Tier 22	US off-road diesel Tier-4A*	Locomotive & Marine Tier 3 CA LEV 3	US Tier 3 LVS** Locomotive & Marine Tier 4	US off-road diesel Tier-4B*
EUROPE	EU Euro-5 CVS	EU Euro-5 LVS*	Netherlands Marine OE/Retrofit	EU off-road Stage 3B*	EU CO ₂ /GHG 120g PM # LVS	EU-6 CVS**	EU off-road Stage 4 EU Euro-6 LVS*
CHINA	Euro-3 Two-wheel Beijing Euro-4 LVS	Beijing CVS Yellow Label		Euro-4 LVS/ CVS	Euro-5 LVS*		Euro-5 CVS*
JAPAN	Cold-start restrictions LVS	Japan-09 LVS/ CVS		NOx reductions LVS		JP-13 CVS	

*Phase in
**Proposed
CVS – Commercial Vehicle Systems
LVS – Light Vehicle Systems

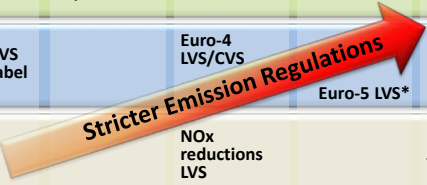


Figure 1.1.1 Trend and comparison of worldwide exhaust emission standards [18].

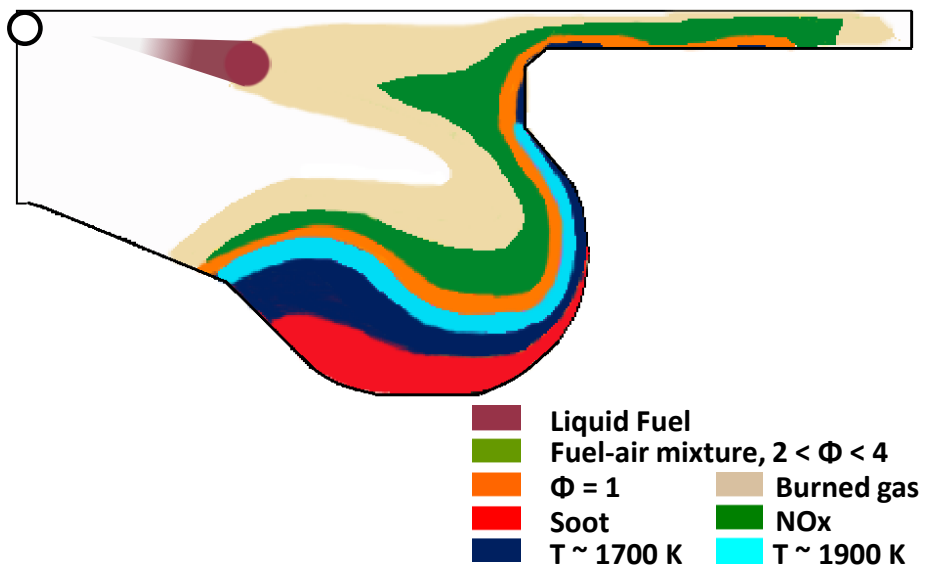


Figure 1.1.2 Diesel combustion: conceptual model.

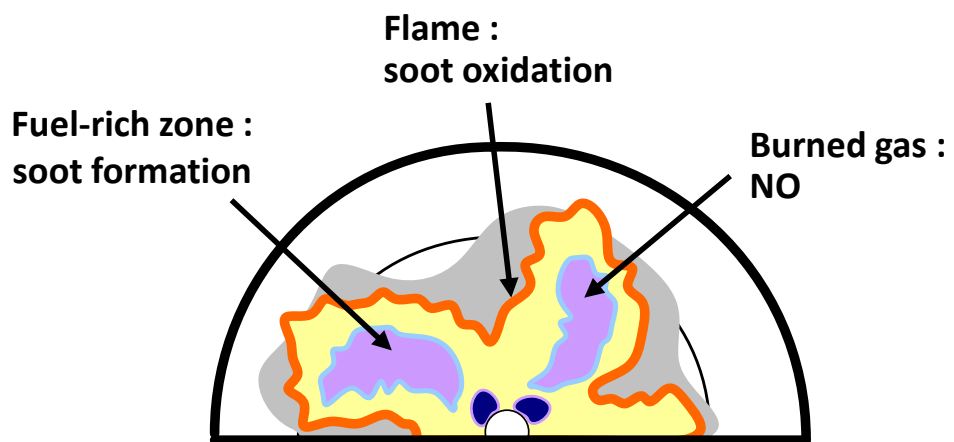


Figure 1.1.3 NO and soot formation mechanism in a Diesel engine during mixing controlled combustion phase [5].

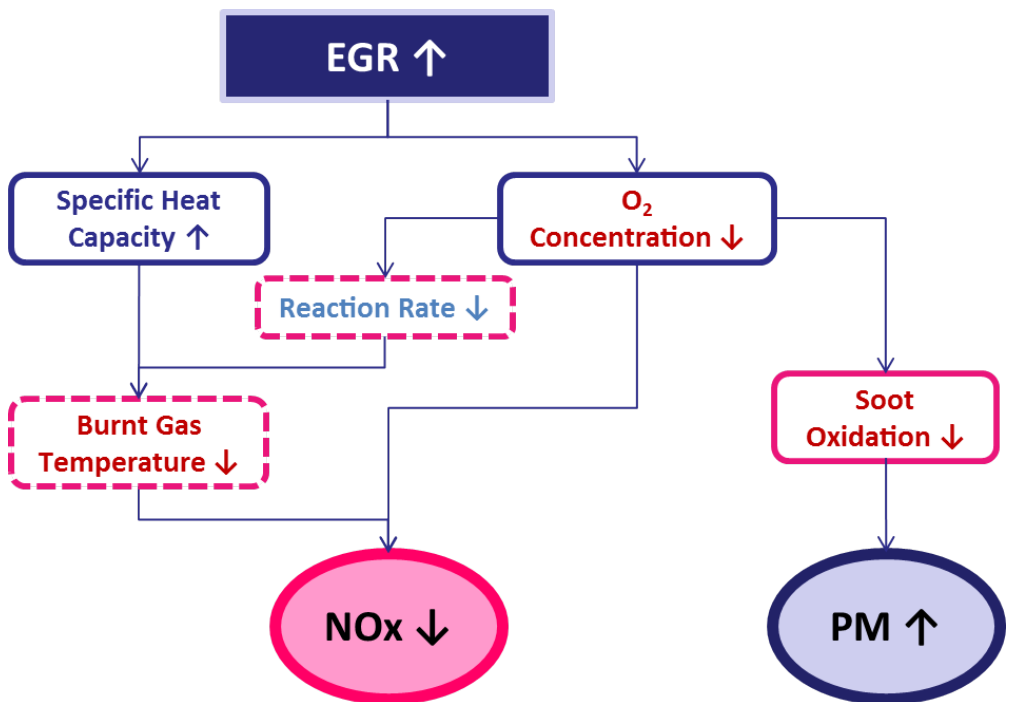


Figure 1.1.4 The effects of EGR on NO_x and soot emissions in Diesel engines.

1.2 In-cylinder EGR Stratification

1.2.1 Concept of in-cylinder EGR stratification

Thus far, engine intake systems have been designed to increase the mixing of fresh air and external EGR to create a uniform in-cylinder EGR distribution because EGR uniformity can reduce NO_x and soot variations cycle by cycle [19, 20]. Therefore, a non-uniform distribution of EGR is rarely used in Diesel engines. In-cylinder EGR stratification, is a technique that simultaneously reduces NO_x and soot using non-uniform EGR distribution in the combustion chamber [21].

If the EGR distribution can be controlled as desired, it is possible to create specific regions in the combustion chamber of locally high EGR concentrations and other regions of locally high O₂ concentrations. Then, fuel is injected into the high EGR region, and combustion starts there. NO_x is decreased because the locally high EGR reduces the O₂ concentration and lowers the combustion gas temperature. Soot can be oxidized during the expansion stroke by mixing with fresh air at the locally high O₂ region [22].

Figure 1.2.1 shows an example of the desired in-cylinder EGR distribution and spray targeting. Figure 1.2.2 explains the detailed mechanism of the effects of the in-cylinder EGR stratification on combustion and emissions. Because combustion starts in the high EGR region, the ignition delay becomes longer, and the initial reaction rate slows down. Moreover, because of the low combustion temperature and O₂ concentration, NO_x emission is reduced. Soot formation could increase modestly due to the locally high EGR region, but the locally high O₂ concentration region participates in soot oxidation at the end of combustion. Therefore, soot oxidation is accelerated during the early expansion stroke. Eventually, NO_x and soot can be reduced at the same time [22, 23].

1.2.2 Previous research about in-cylinder EGR stratification

There were some attempts to stratify EGR gas in the cylinder in spark ignition engines [24-27]. For example, Xu et al. [27] use in-cylinder EGR stratification to reduce the pumping loss and NO_x emission without disadvantages for using EGR such as combustion incompleteness, instability, or misfire. However, in-cylinder EGR stratification has been rarely tried in Diesel engines.

Fuyuto et al. introduced in-cylinder EGR stratification in Diesel engines to reduce emissions [21]. The exhaust emission tests showed that there was less soot emission under medium load conditions when the EGR gas was delivered to the inner part of the piston cavity. The mechanism of this soot reduction was investigated using Computational Fluid Dynamics (CFD) simulation. It was shown that, at the beginning of the combustion, the higher concentration of EGR gas in the inner part of the cavity lowers the combustion gas temperature and reduces the soot formation rate. Air, which exists in the outer part of the cavity at the start of fuel injection, enhances the oxidation of the soot cloud in the piston cavity periphery in the latter half of the combustion period. However, the results showed only soot reduction by using the in-cylinder EGR stratification.

Park et al. improved the concept of in-cylinder EGR stratification using CFD analysis [22]. The 2-step piston was developed to improve the EGR and fuel distributions in the combustion chamber. An ideally-distributed EGR in the cylinder results showed that the locally high EGR region effectively influences the combustion characteristics, and thus, horizontally and centrally stratified EGR has the potential to reduce NO and soot emissions at the same time. In this study, combustion model interworking chemical mechanism was not used.

Choi et al. validated the effect of in-cylinder EGR stratification at a single cylinder engine experiment [28]. A proper in-cylinder swirl with stratified EGR

showed maximum 7 % of NO_x and 23 % of soot reduction simultaneously. Moreover, the robustness of stratified EGR was evaluated under various operating conditions and injection strategies. In this study, the modified intake port and piston was used, but the modification was restricted.

1.2.3 Numerical approach as an engine development tool

CFD has been an essential tool in engine research thanks to the advancement in computational power and accuracy of numerical models during the last decade [29-32]. In CFD, the parameters of engine operating conditions could be set freely, and the isolation of dependent and independent variables could be easily done. Furthermore, the results of CFD analysis provide a set of detailed information on the physical and thermodynamic variables, and an arbitrary number of measurement points could be located in the analysis domain without any perturbations on the fluid field. In addition, the experiments with extreme conditions could be performed without any risks and virtual production of prototypes with arbitrary configuration is possible with low cost.

Classically, engine combustion models have been clearly divided into premixed combustion models for SI engines and non-premixed combustion models for Diesel engines. There are two modes for premixed combustion. A premixed charge of air and fuel can auto-ignite after an auto-ignition delay essentially controlled by temperature, pressure, fuel/air equivalence ratio and residual gases fraction. This type of combustion, from now on called auto ignition, controls the beginning of combustion in Diesel engines and can also be found in SI engines as an undesirable combustion commonly called knock. The second premixed combustion mode is the premixed propagation flame used in SI engines. In this case the combustion chamber is filled with a premixed charge of fuel and air. A spark plug generates a small spherical propagation flame between the electrodes which afterwards propagates in the combustion chamber until it has totally

consumed the premixed fresh charge. The combustion mode for the non-premixed combustion also called diffusion flame. Here, fuel and air are separated by a thin reaction zone in which burned gases are formed. As a first approximation, the chemical time in the reactive zone is usually considered much smaller than the diffusion time involved in the diffusion of fuel and air towards the flame region. This is why this combustion mode is also called mixing controlled combustion [33].

Adaptive models describing diffusion flames have been developed over time. Spalding developed the eddy break up model [34], and it was modified by Magnussen et al. [35]. Magnussen et al. presented a model, based on the eddy break-up concept, which relates the rate of combustion to the rate of dissipation of eddies and expresses the rate of reaction by the mean mass fraction of a reacting species, the turbulence kinetic energy and the rate of dissipation. The main principles behind these models involve replacing the chemical time scale of an assumed one-step reaction with the turbulent time scale. Abraham et al. presented a laminar-and-turbulent characteristic-time combustion model for spark ignition engines [36]. Patterson et al. extended this concept to model Diesel engines [37].

Recently, the ECFM-3Z model was proposed to model auto-ignition and diffusion flames by considering only the dimensions of mixing, represented by the mean mixture fraction and its fluctuation, and the dimension of reaction advancement, represented by the mean progress variable and its fluctuation. The ECFM is a model, which allows the simulation of the two premixed combustion modes, premixed propagation flame combustion in SI engines as well as knock and pollutant formation [38]. Based on this model, the unified Diesel/SI combustion model ECFM-3Z was proposed. In this model, the unburned/burned gas zones description of the ECFM model is kept, as well as the premixed flame description based on the flame surface density equation. In order to account for diffusion flame and mixing processes, each computational cell is split into three mixing zones: a pure fuel zone, a pure air plus possible residual gases zone and a mixed zone [33, 39, 40].

The most important physical sub-processes during the combustion, which are directly related to chemical processes are the auto-ignition, the chemical conversion, and the formation of pollutants such as NO_x and soot [41]. However, the eddy break up model and the ECFM-3Z model do not solve detailed chemical kinetics, therefore they usually describe these sub-processes simple, mainly semi-empirical. Therefore, even though the eddy break up model and the ECFM-3Z model shows good prediction in engine researches [42-45], they have limitations to describe the chemical kinetics.

On the other hand, the flamelet approach was developed by Peters et al. [46-50]. In this model, the reaction rate is tabulated for a laminar diffusion flame in mixture fraction space for different values of the scalar dissipation rate. The flamelet model is capable of describing those sub-processes based on detailed chemical reaction kinetics. As flamelet modelling has the advantage of separating the numerical effort associated with the resolution of fast chemical time scales from the fluid dynamics' scales occurring in the 3-D computation of the engine combustion cycle. 3-D scalar field equations have to be solved in the 3-D engine code, while the entire chemistry consisting of up to 1000 or more chemical reactions is simultaneously treated in a separate 1-D code describing the flamelet structure [41]. The flamelet approach has many variations such as two-dimensional flamelet [51, 52], simplified two-dimensional flamelet [53, 54], multiple flamelet [55, 56], and regenerative multiple flamelet model [57, 58], and it was applied to engine researches successfully.

For example, Hamosfakidis et al. suggested regenerative multiple flamelet (RMF) model to describe HCCI and partially premixed compression ignition (PPCI) combustion [57, 58]. The model is based on a 2-D flamelet concept and uses two conserved scalars. The reactive scalars (species mass fractions and enthalpy) are expressed as a function of time and the two conserved scalars.

In order to study in-cylinder EGR stratification, it is necessary to examine the effects of EGR distributions in the combustion chamber on combustion and emission characteristics. However, in-cylinder gas distributions cannot be directly measured by experimental method. Moreover, to observe spray behavior, velocity field, temperature distribution and location of emission formation, it requires a lot of cost and exhaustive efforts experimentally. In CFD, not only those variables but also species distribution could be observed by solving the governing equations. Therefore, CFD analysis is essential tool for studying in-cylinder EGR stratification. Moreover, as in-cylinder EGR stratification concept is focused to emission reduction, CFD analysis based on the chemical kinetics is important to predict the emission formation. However, the conventional flamelet model cannot consider the non-uniform EGR gas distribution as the model can solve the flamelet equations with regard to only one initial condition including scalar concentrations.

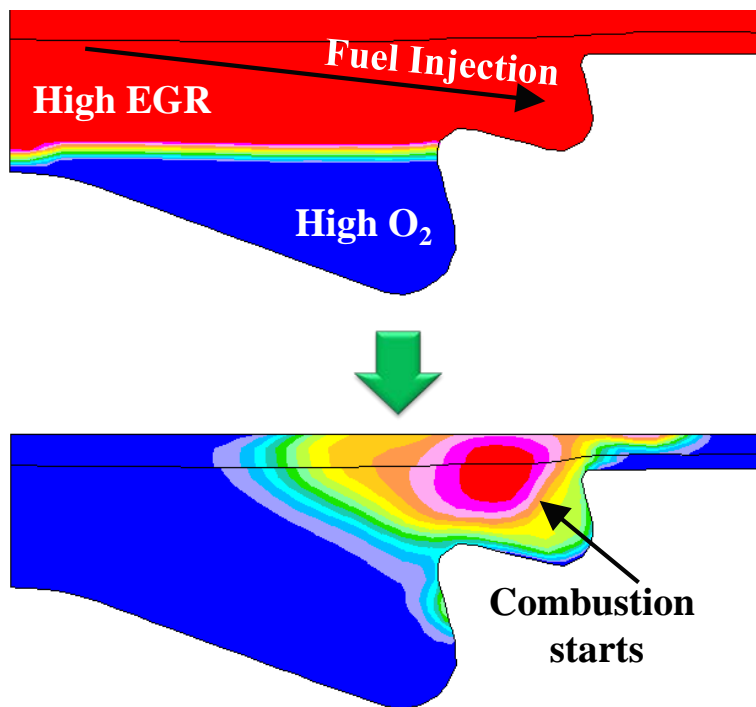


Figure 1.2.1 Desired in-cylinder EGR stratification and spray targeting [23].

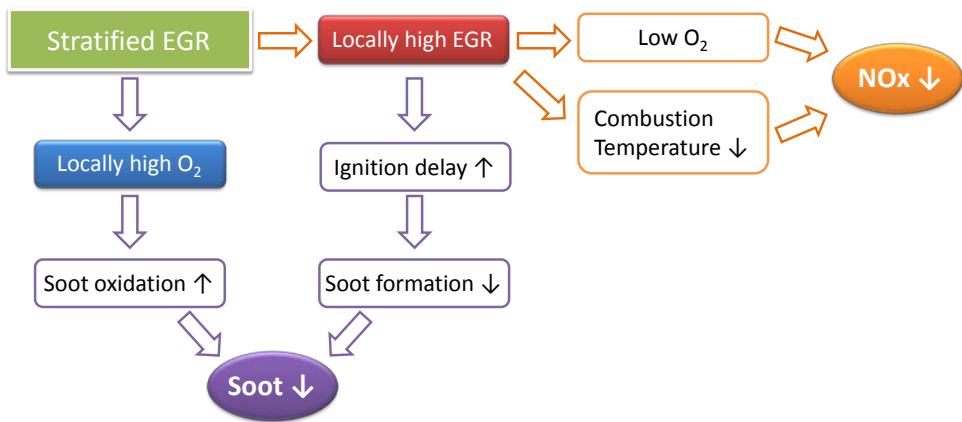


Figure 1.2.2 Concept of NO_x-soot simultaneous reduction by stratified EGR [22].

1.3 The Need of the Combustion Model for Stratified EGR Distribution

The conventional flamelet model has advantages of describing processes during the combustion such as the auto-ignition, the chemical conversion, and the emission formation based on detailed chemical reaction kinetics. Until now, the flamelet approach in the Diesel engine simulation assume that the EGR gas and air are well mixed during the intake and compression stroke then distribute uniformly in the combustion chamber as the flamelet model can solve the flamelet equations with regard to only one initial condition including scalar concentrations.

However, EGR gas is non-uniformly distributed in the combustion chamber because of the incomplete mixing between air and external EGR through the intake port and residual gas (which remains the combustion chamber after an exhaust process). Figure 1.3.1 shows a schematic diagram of EGR system, high pressure loop EGR (HP-EGR) and low pressure loop EGR (LP-EGR) [59]. The HP-EGR system is widely used in the turbocharged Diesel engines as the pressure of turbine inlet (P3) is higher than that of compressor outlet (P2). In HP-EGR, a mixing length of the air and external EGR gas is not enough to make uniform air and external EGR mixture. Figure 1.3.2 shows the deviation of cylinder by cylinder EGR rate [60]. The deviation occurs because the air and external EGR gas are not mixed enough in the intake manifold.

On the other hand, in LP-EGR, the external EGR gas is supplied from the turbine outlet (P4) to the compressor inlet (P1) as shown in Figure 1.3.1 (b). In LP-EGR, mixing between air and external EGR gas increases as a mixing length of the air and external EGR gas is lengthened by passing some additional parts i.e. an intercooler. Therefore, cylinder by cylinder EGR variation is reduced [9, 19]. However, even LP-EGR case the non-uniform EGR distribution exists due to residual gas.

Figure 1.3.3 shows the prediction results of in-cylinder EGR distribution at 10° before top dead center (BTDC) under conditions of 1500 rpm, bmep 4 bar, and EGR 35 %. The air and external EGR gas are supplied uniformly through the intake port assuming well-mixed condition (similar condition with the LP-EGR). However, the maximum EGR rate is 42.3 % and the minimum EGR rate is 36.1 %, where the overall EGR rate is 39.4 % (the overall EGR rate, 39.4 % is higher than supplied external EGR rate, 35 % because of the residual gas). Therefore, the assumption of the flamelet model for Diesel combustion has a limitation intrinsically.

Moreover, in case of in-cylinder EGR stratification, the non-uniformity of in-cylinder EGR is increase as shown in Figure 1.3.4. To increase the degree of EGR stratification which means the difference between locally maximum EGR rate and locally minimum EGR rate, the air and external EGR gas is supplied separately. In this case, the maximum EGR rate is 50.1 % and the minimum EGR rate is 32.4 %, where the overall EGR rate is 39.4 %.

In order to study in-cylinder EGR stratification, it is necessary to examine the effects of EGR distributions in the combustion chamber on combustion and emission characteristics. However, in-cylinder gas distributions cannot be directly measured by experimental method. Moreover, to observe spray behavior, velocity field, temperature distribution and location of emission formation, it requires a lot of cost and exhaustive efforts experimentally. In CFD, not only those variables but also species distribution could be observed by solving the governing equations. Therefore, CFD analysis is essential tool for studying in-cylinder EGR stratification. Moreover, as in-cylinder EGR stratification concept is focused to emission reduction, CFD analysis based on the chemical mechanism is important to precisely predict the emission formation. However, the conventional flamelet approach which can solve the chemical mechanism cannot apply to non-uniform EGR distribution conditions. Therefore, another combustion model based on the chemical kinetics is needed.

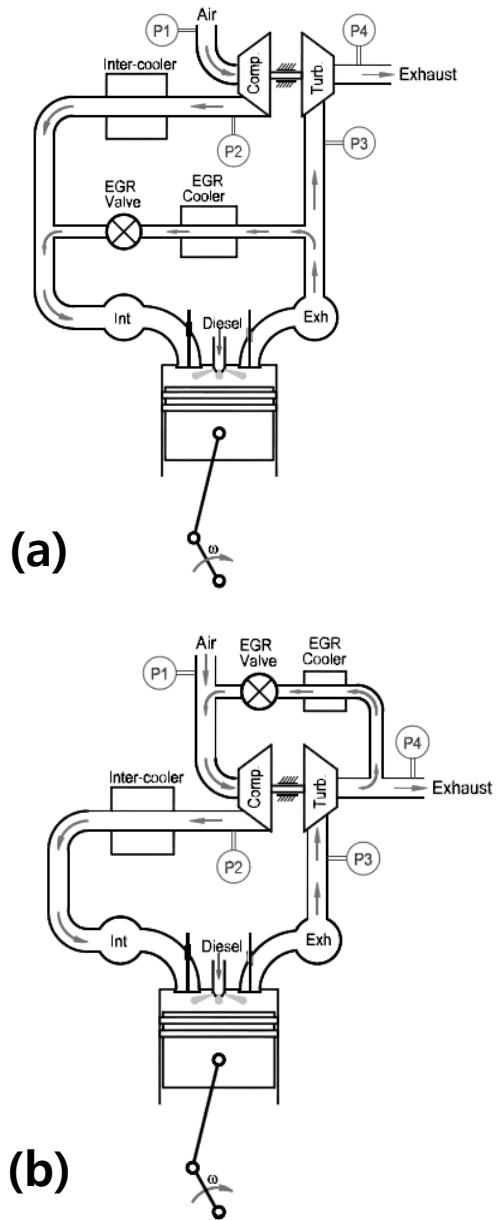


Figure 1.3.1 Schematic diagram of EGR system in a turbocharged Diesel engine (a) High pressure loop EGR and (b) Low pressure loop EGR [59].

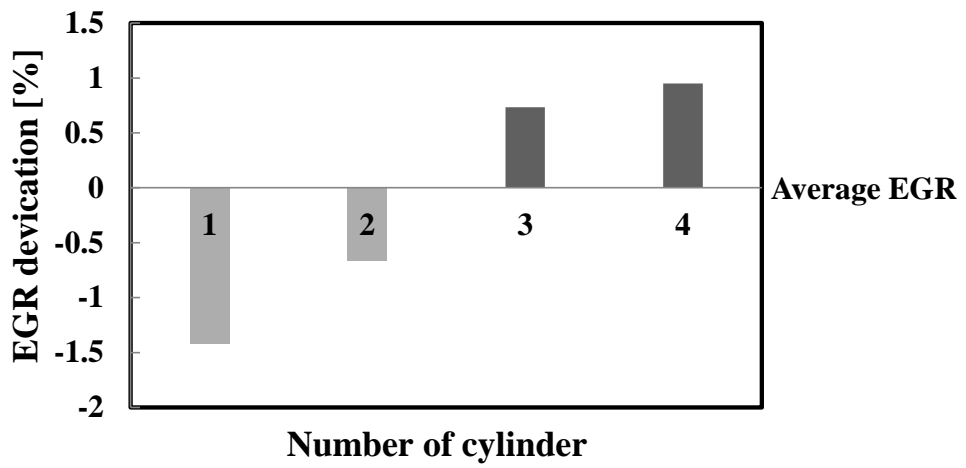


Figure 1.3.2 The deviation of cylinder by cylinder EGR rate [60].

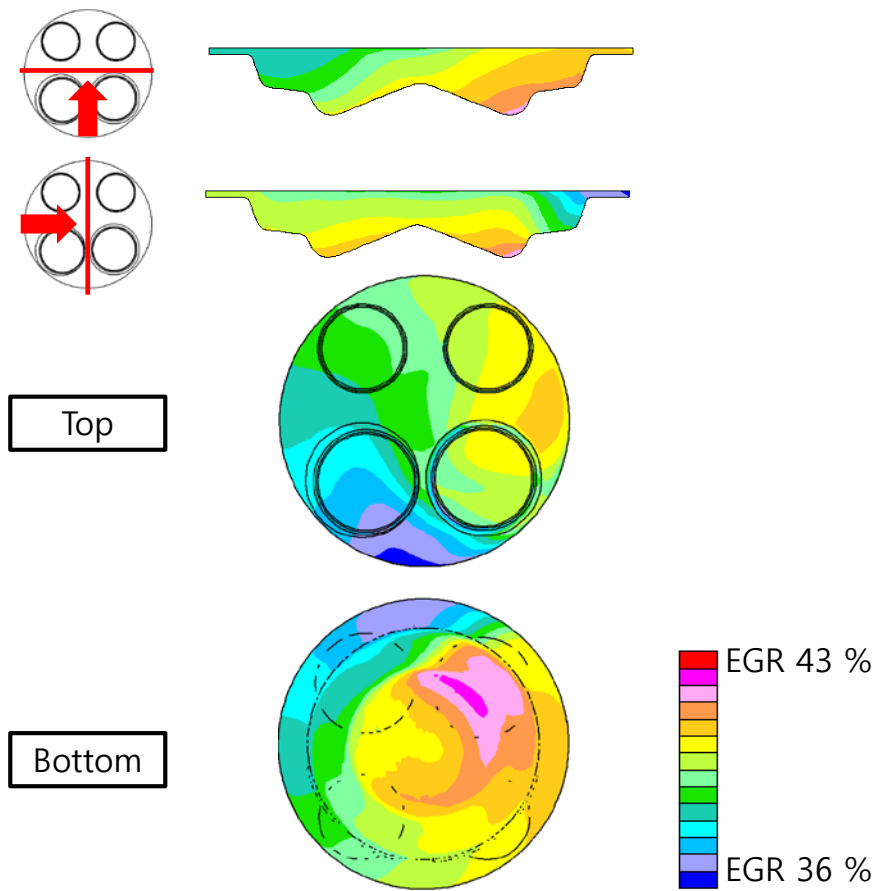


Figure 1.3.3 EGR distribution in the combustion chamber under conventional engine intake system.

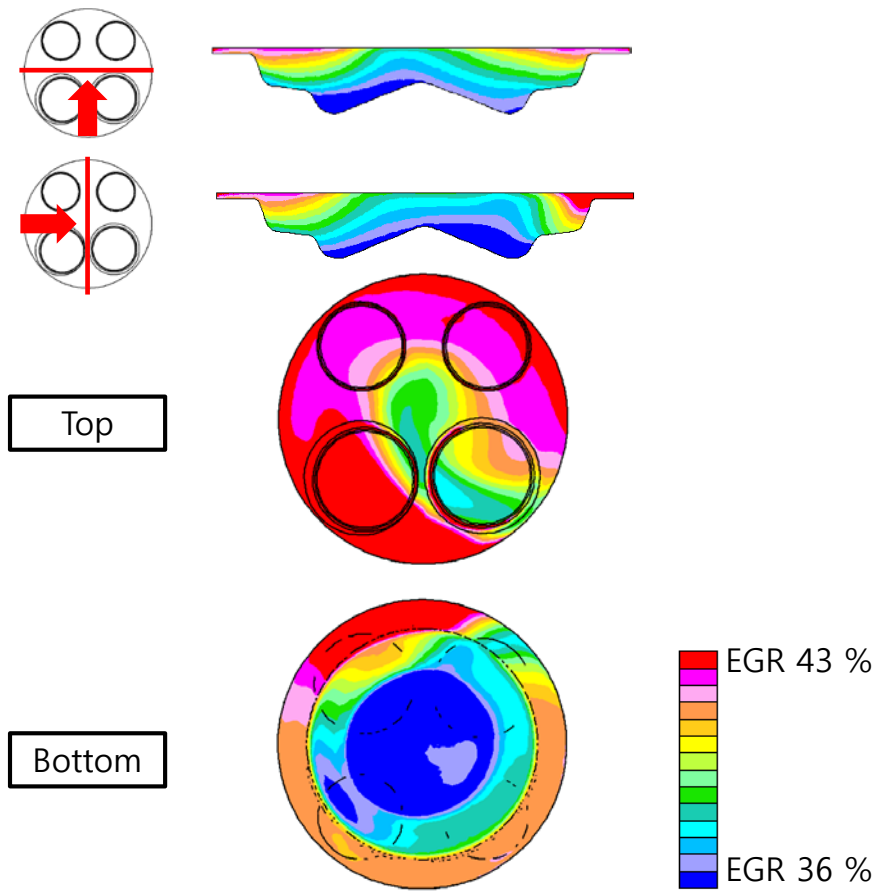


Figure 1.3.4 EGR distribution in the combustion chamber under EGR stratification system.

1.4 Objectives

In this study, the Flamelet for Stratified EGR Distribution (FSE) model was developed to consider the non-uniform in-cylinder EGR distribution, and then the potential of in-cylinder EGR stratification for reducing emissions in Diesel engines was investigated.

The detailed objectives of this study are:

1. Developing the combustion model based on chemical kinetics to consider the non-uniform in-cylinder EGR distribution,
2. Optimizing the combustion system for enhancing the effect of in-cylinder EGR stratification, and
3. Investigating the potential of simultaneous reduction of NO_x and soot in the combustion chamber.

Chapter 2. Combustion and Emission Models Review

2.1 Turbulence Model

2.1.1 Governing equations

The mass and momentum conservation equations for compressible fluid flows are in Cartesian tensor notation [61, 62] :

$$\frac{\partial \rho}{\partial t} + \frac{\partial(\rho v_\alpha)}{\partial x_\alpha} = s_m \quad (2.1.1)$$

$$\frac{\partial(\rho v_\alpha)}{\partial t} + \frac{\partial(\rho v_\alpha v_\beta - \tau_{\alpha\beta})}{\partial x_\alpha} = -\frac{\partial p}{\partial x_\alpha} + s_\alpha \quad (2.1.2)$$

Where, t : time

x_α : Cartesian coordinate ($\alpha = 1, 2, 3$)

v_α : absolute fluid velocity component in direction x_α

p : piezometric pressure

ρ : density

$\tau_{\alpha\beta}$: stress tensor components

s_m : mass source

s_α : momentum source components.

In CFD analysis, Newtonian fluid is assumed as

$$\tau_{\alpha\beta} = \mu \left(\frac{\partial v_\alpha}{\partial x_\beta} + \frac{\partial v_\beta}{\partial x_\alpha} \right) + \delta_{\alpha\beta} \lambda \frac{\partial v_\gamma}{\partial x_\gamma}, \quad \lambda = -\frac{2}{3} \mu \quad (2.1.3)$$

Where, μ is the dynamic viscosity and $\delta_{\alpha\beta}$ is the Kronecker delta.

2.1.2 Turbulence model

Since various sizes of scales exist in this turbulence, equation (2.1.1) and (2.1.2) should be solved in the smallest time and length scale. It is called as direct numerical simulation (DNS) but it is impossible to solve these equations at the case of engine simulations which have complicated engine geometry and high Reynolds number in the smallest mesh size and time step practically due to the computational power. Therefore, the other solutions to solve these equations are needed, and the simplest method is modeling a small motion. Although modeling the small motion could abandon the minor information, it saves the computational cost without loss of important information. The general reduction method is an averaging the original equations [63].

The RNG (Re-Normalization Group) $k - \varepsilon$ model is modified version of the standard $k - \varepsilon$ model [64, 65]. The model shows good results in engine combustion simulations. From the RNG model turbulent kinetic energy and dissipation can be written like below.

$$\frac{\partial \bar{\rho} \tilde{k}}{\partial t} + \frac{\partial}{\partial x_\alpha} \left[\bar{\rho} \tilde{v}_\alpha \tilde{k} - \left(\mu + \frac{\mu_t}{\sigma_\gamma} \right) \frac{\partial \tilde{k}}{\partial x_\alpha} \right] = \mu_t (P + P_B) - \bar{\rho} \tilde{\varepsilon} - \frac{2}{3} \left(\frac{\partial \tilde{v}_\beta}{\partial x_\beta} + \rho \tilde{k} \right) \frac{\partial \tilde{v}_\beta}{\partial x_\beta} \quad (2.1.13)$$

$$\begin{aligned} \frac{\partial \bar{\rho} \tilde{\varepsilon}}{\partial t} + \frac{\partial}{\partial x_\alpha} \left[\bar{\rho} \tilde{v}_\alpha \tilde{\varepsilon} - \left(\mu + \frac{\mu_t}{\sigma_\gamma} \right) \frac{\partial \tilde{\varepsilon}}{\partial x_\alpha} \right] &= C_{\varepsilon 1} \frac{\tilde{\varepsilon}}{\tilde{k}} \left[\mu_t P - \frac{2}{3} \left(\mu_t \frac{\partial \tilde{v}_\beta}{\partial x_\beta} + \bar{\rho} \tilde{k} \right) \frac{\partial \tilde{v}_\beta}{\partial x_\beta} \right] \\ &+ C_{\varepsilon 2} \frac{\tilde{\varepsilon}}{\tilde{k}} \mu_t P_B - C_{\varepsilon 3} \bar{\rho} \frac{\tilde{\varepsilon}^2}{\tilde{k}} + C_{\varepsilon 4} \bar{\rho} \frac{\partial \tilde{v}_\beta}{\partial x_\beta} - \frac{C_\mu \eta^3 (1 - \eta / \eta_0) \bar{\rho}}{1 + \phi \eta^3} \frac{\tilde{\varepsilon}^2}{\tilde{k}} \end{aligned} \quad (2.1.14)$$

Where, $P \equiv S_{\alpha\beta} \frac{\partial \tilde{v}_\alpha}{\partial x_\beta}$, $P_B \equiv -\frac{\bar{g}_\alpha}{\sigma_{h,t}} \frac{1}{\bar{\rho}} \frac{\partial \bar{\rho}}{\partial x_\alpha}$, $\eta = S \frac{\tilde{k}}{\tilde{\varepsilon}}$ and C , η_0 , and ϕ are empirical coefficients listed in Table 2.1.1.

Table 2.1.1 Coefficients of the RNG $k - \varepsilon$ Turbulence Model [61].

C_μ	σ_k	σ_ε	σ_h	$C_{\varepsilon 1}$	$C_{\varepsilon 2}$	$C_{\varepsilon 3}$	$C_{\varepsilon 4}$	η_0	β
0.085	0.719	0.719	0.9	1.42	1.68	0.0 or 1.42*	-0.33	4.38	0.012

* $C_{\varepsilon 3} = 1.44$ for $P_B > 0$ and is zero otherwise

2.2 Laminar Flamelets

In engine simulation, several physical processes, such as turbulent flows, fuel spray injection, droplet evaporation, and combustion, are interacting with each other. Therefore, to describe the accurate combustion processes, a detailed chemistry model and consideration of turbulence effects on chemical reactions are needed. At the same time, the computational cost has to be of an acceptable level [61]. In the flamelet model, a turbulent flame is considered to be an ensemble of laminar flamelets. As the chemical time scale is very short compared to the turbulent time scales, combustion occurs within thin layers embedded in the turbulent flow, i.e. within flamelets [66]. The flamelet model decouples turbulent flow fields and chemistry. Therefore, detailed chemistry can be applied to the flamelet model within an acceptable level of the computational cost.

2.2.1 Laminar flamelet model

The reactive-diffusive structure of the flamelet is determined by the equation for the species mass fraction, Y_i , and temperature as [67]:

$$\rho \frac{\partial Y_i}{\partial t} + \rho \bar{v} \cdot \nabla Y_i = \frac{1}{Le_i} \nabla \cdot (\rho D \nabla Y_i) + \dot{m}_i \quad (i=1,2,\dots, n) \quad (2.2.10)$$

$$\rho c_p \frac{\partial T}{\partial t} + \rho c_p \bar{v} \cdot \nabla T = \nabla \cdot (\rho c_p D_T \nabla Y_i) - \sum_{k=1}^n h_k \dot{m}_k + q_R + \frac{\partial p}{\partial t} \quad (2.2.11)$$

where, \dot{m}_k and h_k denote the chemical source term and enthalpy of species k , respectively, and $\sum_{k=1}^n h_k \dot{m}_k$ denotes the heat release rate. Lewis numbers for all species, $Le_i = \lambda / \rho c_p D_i = D_T / D_i$ are assumed to be constant. Moreover, it is assumed that the mass fraction Z and the surface of the stoichiometric mixture can

be determined from Eq. (2.2.9) and Eq. (2.2.8). The surface of the stoichiometric mixture is shown in Figure 2.2.2.

To simplify the equations of mass fraction and temperature, a local coordinate system (x_1, x_2, x_3 , and t) was introduced. As shown in Figure 2.2.2, the orthogonal coordinate system attached to the surface of stoichiometric mixture, where x_1 points normal to the surface $Z(x_\alpha, t) = Z_{st}$ and x_2 , and x_3 lie within the surface. The coordinate x_1, x_2, x_3 , and t is replaced Z, Z_2, Z_3 , and τ respectively. By definition, the new coordinate Z is locally normal to the surface of stoichiometric mixture. If it is assumed that the flamelet is thin in Z direction, the terms containing Z_2, Z_3 can be neglect. Then the one dimensional species and temperature equation are obtained like below.

$$\rho \frac{\partial Y_i}{\partial t} = \frac{\rho \chi}{2} \frac{\partial^2 Y_i}{\partial Z^2} + \dot{m}_i \quad (2.2.17)$$

$$\rho \frac{\partial T}{\partial t} = \frac{\rho \chi}{2} \left(\frac{\partial^2 T}{\partial Z^2} + \frac{1}{c_p} \frac{\partial c_p}{\partial Z} \frac{\partial T}{\partial Z} - \frac{\partial T}{\partial Z} \sum \frac{c_{p,k}}{c_p} \frac{\partial Y_k}{\partial Z} \right) - \frac{1}{c_p} \left(\sum h_k \dot{m}_k - \frac{\partial p}{\partial t} \right) \quad (2.2.18)$$

Here, χ is the scalar dissipation rate, as an important quantity in flamelet equations. It is defined by

$$\chi = 2D \sum \left(\frac{\partial Z}{\partial x_\alpha} \right)^2. \quad (2.2.19)$$

However, this quantity is difficult to extract from a calculation of a turbulent flow since it requires the instantaneous value of Z . In addition, it is important that the gradual homogenization of the mixture is reflected in the scalar dissipation rate [68]. As the scalar dissipation rate increases, the heat transfer from the reaction zone to the surrounded inertia increases which causes an increase in the ignition delay time.

The Z-dependence of the scalar dissipation rate, χ , for a laminar, stationary counter flow diffusion flame with constant density and diffusion coefficient is [69] :

$$\chi(Z) = \frac{a}{\pi} \exp\{-2[\text{erfc}^{-1}(2Z)]^2\} \approx 4aZ^2[\text{erfc}^{-1}(2Z)]^2 \quad (2.2.21)$$

where a is the strain rate and erfc^{-1} is the inverse of the complementary error function.

2.2.2 RIF model

Unlike the laminar flamelet equations in one-dimensional mixture fraction space, the turbulent flow and mixing field equations are formulated in three-dimensional physical space [51]. The representative interactive flamelet (RIF) model couples the solutions of the turbulent flow and mixing field and the solutions of the laminar flamelet [70]. Figure 2.2.3 shows the coupling between the CFD code and the flamelet code schematically. In this study, the commercial CFD code, STAR-CD v. 4.16 was used for calculating the turbulent flow and mixing. STAR-CD provides a facility for the customization of the solver via FORTRAN 77 subroutines the so-called “user subroutines”. The flamelet code was produced by using this user subroutine. At each time step, the CFD code calculates the transport equations of the mixture fraction, mixture fraction variance, boundary conditions and the stoichiometric scalar dissipation rate. Based on the results from the CFD code, the flamelet code calculates the species and temperature distributions in the mixture fraction coordinate. The flamelet code takes dozens of time steps within one CFD time step, depending on the chemistry and mixing time scales. In this way, the time scales of fluid dynamics and the chemistry are decoupled. Then the flamelet code calculates the species mass fractions $Y_i(Z, t)$. The results are delivered to the CFD code in the Favre averaged form for the turbulent flow. Finally, The CFD code calculates the temperature of each cell based on the flamelet results.

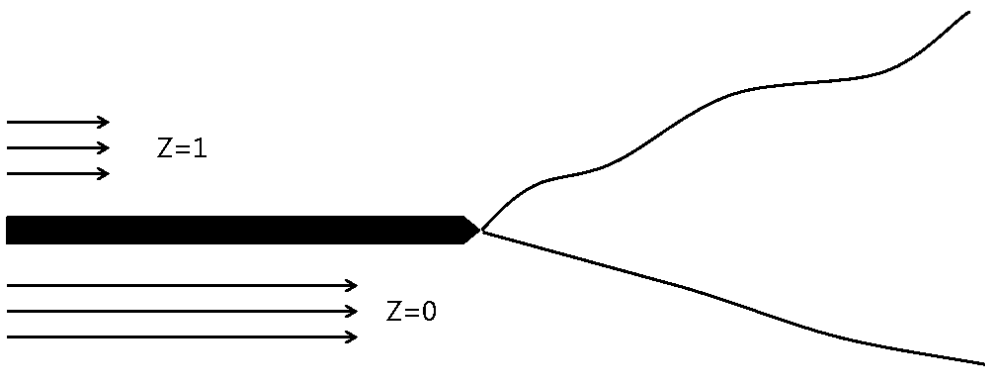


Figure 2.2.1 Mixing behind a splitter plate for a two-feed system [71]

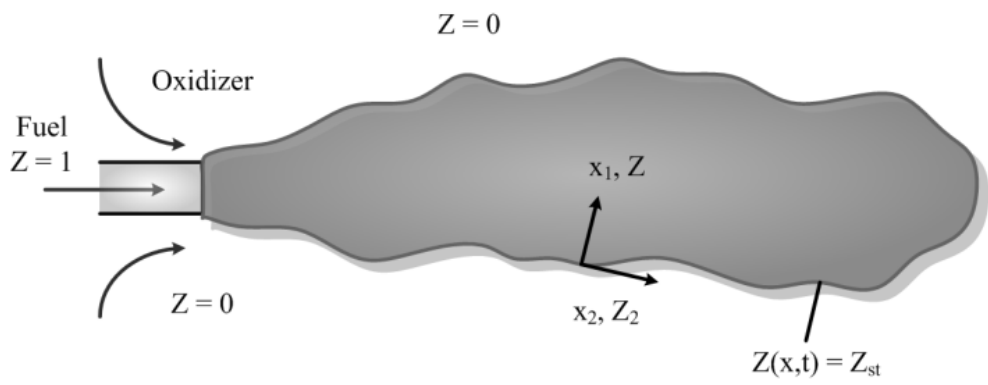


Figure 2.2.2 Surface of stoichiometric mixture in a turbulent jet [46].

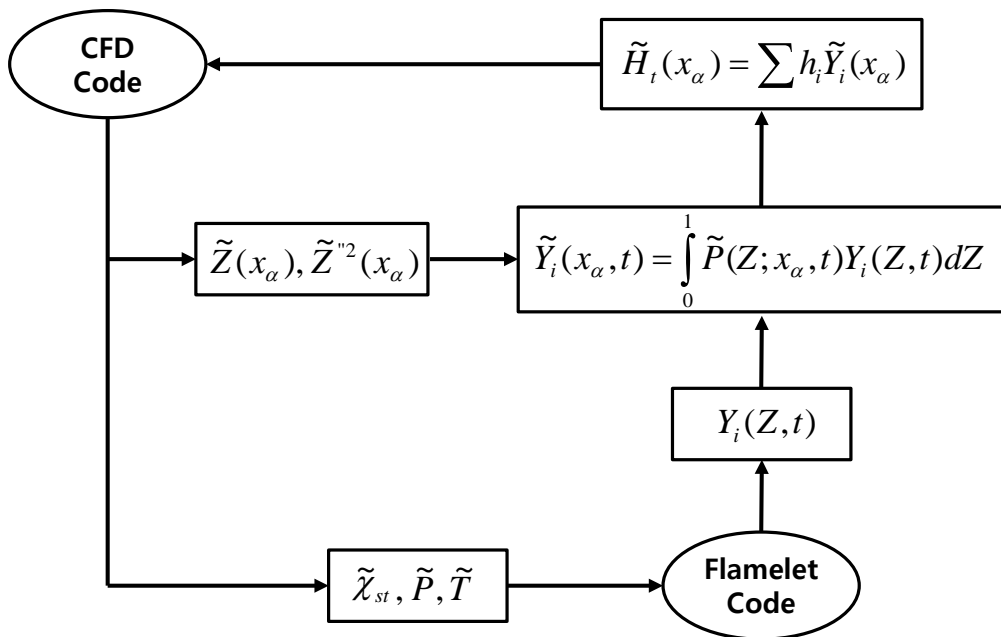


Figure 2.2.3 Structure of the RIF model.

2.3 Models for Liquid Droplets

The essential processes of the Diesel engine combustion are fuel injection, atomization, vaporization, and fuel-air mixing. The liquid fuel atomizes into small droplets through nozzles in the injector tip and penetrates into the combustion chamber. Then, the fuel vaporizes and mixes with the high temperature in-cylinder gas [5].

2.3.1 Lagrangian multi-phase model

A velocity, displacement, size, and temperature of dispersed phases such as liquid droplets in a continuous phase like air can be calculated by solving the conservation equations for droplets in the Lagrangian framework. The basic conservation equations are as follows [61]:

- **Momentum**

The momentum equation for a droplet is

$$m_d \frac{d\bar{u}_d}{dt} = \bar{F}_{dr} + \bar{F}_p + \bar{F}_{am} + \bar{F}_b \quad (2.4.1)$$

where, m , u , and F are mass, velocity, and force respectively, and subscript d denotes the droplet phase.

- **Mass**

The droplet mass rate of change is given by

$$\frac{dm_d}{dt} = -A_s F_m \quad (2.4.5)$$

where, F_m is mass transfer rate per unit surface area and A_s is the droplet surface area.

• Energy

The droplet energy balance takes into account the mechanisms of surface heat transfer rates per unit surface area and loss/gain due to phase change, thus:

$$m_d c_{p,d} \frac{dT_d}{dt} = -A_s q_d'' + h_{fg} \frac{dm_d}{dt} \quad (2.4.7)$$

where, $c_{p,d}$, h_{fg} , and q_d'' means the droplet specific heat, the latent heat of phase change, and surface heat flux respectively.

2.3.2 Droplet break-up model

The break-up of liquid fuel is a complex physical phenomenon which is associated with the aerodynamic liquid-gas interaction, the physical and thermal properties of the fuel and the surrounding gases [72]. In this study, the Reitz and Diwakar break-up model [73, 74] was used to describe the spray break-up process.

According to this model, droplet break-up due to aerodynamic forces occurs in one of following modes: bag break-up and stripping break-up. Bag break-up occurs due to the non-uniform pressure field around the droplet, which expand in the low-pressure wake region. The droplet breaks up when the surface tension force are overcome. Stripping break-up is a process in which smaller droplet is sheared or stripped form the droplet surface. The instantaneous droplet diameter D_d can be

determined by using the stable droplet diameter $D_{d,stable}$ and characteristic time scale

τ_b of the break-up process like below:

$$\frac{dD_d}{dt} = \frac{(D_d - D_{d,stable})}{\tau_b} \quad (2.4.8)$$

- **Bag break-up**

The instability is determined by a critical value of the Weber number, We .

$$We = \frac{\rho |\vec{u} - \vec{u}_d|^2 D_d}{2\sigma_d} \geq C_{b1} \quad (2.4.9)$$

Where, σ_b is the surface tension coefficient, and C_{b1} is an empirical coefficient having a value in the range of 3.6 to 8.4. [74] and the value of 6 was used in this study. The characteristic time is

$$\tau_b = \frac{C_{b2} \rho_d^{1/2} D_d^{3/2}}{4\sigma_d^{1/2}} \quad (2.4.10)$$

where, π was used for the coefficient C_{b2} .

- **Stripping break-up**

The criterion for the onset of the stripping break-up is

$$\frac{We}{\sqrt{Re_d}} \geq C_{s1} \quad (2.4.11)$$

where, Re_d is the droplet Reynolds number and C_{s1} is a coefficient with the value 0.5 [74]. The characteristic time is

$$\tau_b = \frac{C_{s2}}{2} \left(\frac{\rho_d}{\rho} \right)^{1/2} \frac{D_d}{|\vec{u} - \vec{u}_d|} \quad (2.4.12)$$

where C_{s2} is the empirical constant in the range of 2 to 20 [74] and the value of 20 was used in this study.

2.4 Models for Chemical Mechanics and Emissions

2.4.1 Fuel mechanism

In this study, reduced reaction mechanism for n-heptane was used to simulate Diesel fuel chemistry. The reaction mechanism consist of 29 species and 52 reactions and the reactions are listed in Table 2.4.1 [75]. This mechanism was validated under both constant-volume and engine conditions, and the results show that the mechanism gives similar predictions of a comprehensive mechanism (179 species, 1642 reactions [76]) with reducing 50~70 % of CPU time than a comprehensive mechanism.

2.4.2 NO_x model

To predict NO and NO₂ production four additional species (N, NO, NO₂, N₂O) and nine reactions were added to the n-heptane chemistry mechanism [77] and the reactions are listed in Table 2.4.2. The Gas Research Institute (GRI) NO mechanism (22 species, 101 reactions [78]) were reduced by using SENKIN. The reactions include the Zeldovich reactions and thermal NO_x formation through NO₂ and N₂O reactions pathways. The NO₂ and N₂O reactions were considered due to the fact that the LTC favors the formation of these two NO_x species over NO formation [79].

2.4.3 Soot model

Soot is formed from unburned fuel, which nucleates from a gas phase to a solid phase in fuel rich regions at elevated temperatures [80]. Figure 2.4.1 shows a schematic diagram of the steps in the soot formation process. There are six commonly identified processes: pyrolysis, nucleation, coalescence, surface growth,

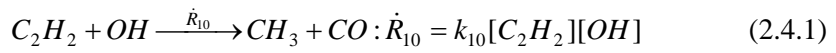
agglomeration, and oxidation and those soot formation processes can be grouped two, gas phase reaction and solid phase reaction [80]. Among the species relevant to soot formation, acetylene plays an important role by participating the precursor formation and the surface growth of soot particles.

Daly and Nag developed detailed soot model based on detailed kinetic mechanisms for hydrocarbon oxidation by Westbrook et al. [80-86] and soot formation and oxidation by Frenklach et al. [80, 87, 88]. To provide the gas phase species relevant to soot formation and oxidation such as PAH and C_2H_2 , the complex reaction mechanism is needed. Therefore, the big problem of this detailed soot model is difficulty of implementation to CFD codes. For example, Daly and Nags soot model involves 614 species and 2883 reactions.

Phenomenological soot models are more useful for multidimensional modeling than the detailed soot model as the detailed soot model is computationally expensive. Tao et al. suggested the nine-step phenomenological soot model for Diesel engine [89]. The nine steps of Tao's model are: (1) acetylene formation from fuel pyrolysis; (2) soot precursor formation from acetylene; (3) particle inception from soot precursors; (4) soot particle coagulation; (5) surface growth from acetylene; (6) oxidation by O_2 ; (7) oxidation by OH; (8) acetylene oxidation by O_2 ; (9) precursor oxidation by OH. The validation results show good agreement with the experimental results; however a fundamental weakness still exists due to the inability to predict differences in soot formation for fuels of different composition and structure [80]. From the model, acetylene forms from fuel pyrolysis using single reaction and it is oxidized by O_2 and the concentration of OH is estimated from a $H_2-O_2-CO_2$ system. Moreover, comparisons between predicted results and measured results were conducted only soot mass density.

In this study, soot model was modified for better prediction based on the Tao's nine-step phenomenological soot model. The nine step soot model is extended to ten-step phenomenological model by adding a step of (10) the acetylene oxidation by OH. The total steps for soot formation is shown in the Figure 2.4.2.

STEP 10. Acetylene oxidation



where, $k_{10} = 3.2 \times 10^{15} \exp(-0.6 \times 10^4 / T)$ ($\text{mole}^{-1} \text{cm}^3 \text{s}^{-1}$).

Unlike the nine-step soot model, the OH concentration is obtained from the n-heptane mechanism which was described in Chapter 2.4.1 in the ten-step soot model. Moreover, rate constants are changed by comparing with the experimental results.

Table 2.4.1 Reactions for n-heptane [75].

NO.	REACTIONS	A	b	E
1	$nC_7H_{16}+H=C_7H_{15-2}+H_2$	4.38E+07	2	4760
2	$nC_7H_{16}+OH=C_7H_{15-2}+H_2O$	4.50E+09	1.3	1090
3	$nC_7H_{16}+HO_2=C_7H_{15-2}+H_2O_2$	1.65E+13	0	16950
4	$nC_7H_{16}+O_2=C_7H_{15-2}+HO_2$	2.00E+15	0	47380
5	$C_7H_{15-2}+O_2=C_7H_{15}O_2$	1.56E+12	0	0
6	$C_7H_{15}O_2+O_2=C_7ket_{12}+OH$	1.35E+14	0	18232.7
7	$C_7ket_{12}=C_5H_{11}CO+CH_2O+OH$	3.53E+14	0	41100
8	$C_5H_{11}CO=C_2H_4+C_3H_7+CO$	9.84E+15	0	40200
9	$C_7H_{15-2}=C_2H_5+C_2H_4+C_3H_6$	7.05E+14	0	34600
10	$C_3H_7=C_2H_4+CH_3$	9.60E+13	0	30950
11	$C_3H_7=C_3H_6+H$	1.25E+14	0	36900
12	$C_3H_6+CH_3=C_3H_5+CH_4$	9.00E+12	0	8480
13	$C_3H_5+O_2=C_3H_4+HO_2$	6.00E+11	0	10000
14	$C_3H_4+OH=C_2H_3+CH_2O$	1.00E+12	0	0
15	$C_3H_4+OH=C_2H_4+HCO$	1.00E+12	0	0
16	$CH_3+HO_2=CH_3O+OH$	5.00E+13	0	0
17	$CH_3+OH=CH_2+H_2O$	7.50E+06	2	5000
18	$CH_2+OH=CH_2O+H$	2.50E+13	0	0
19	$CH_2+O_2=HCO+OH$	4.30E+10	0	-500
20	$CH_2+O_2=CO_2+H_2$	6.90E+11	0	500
21	$CH_2+O_2=CO+H_2O$	2.00E+10	0	-1000

22	$\text{CH}_2+\text{O}_2=\text{CH}_2\text{O}+\text{O}$	5.00E+13	0	9000
23	$\text{CH}_2+\text{O}_2=\text{CO}_2+\text{H}+\text{H}$	1.60E+12	0	1000
24	$\text{CH}_2+\text{O}_2=\text{CO}+\text{OH}+\text{H}$	8.60E+10	0	-500
25	$\text{CH}_3\text{O}+\text{CO}=\text{CH}_3+\text{CO}_2$	1.57E+14	0	11800
26	$\text{CO}+\text{OH}=\text{CO}_2+\text{H}$	8.99E+07	1.4	5232.9
27	$\text{O}+\text{OH}=\text{O}_2+\text{H}$	4.00E+14	-0.5	0
28	$\text{H}+\text{HO}_2=\text{OH}+\text{OH}$	1.70E+14	0	875
29	$\text{OH}+\text{OH}=\text{O}+\text{H}_2\text{O}$	6.00E+08	1.3	0
30	$\text{H}+\text{O}_2+\text{m}=\text{HO}_2+\text{m}$	3.60E+17	-0.7	0
31	$\text{H}_2\text{O}_2+\text{m}=\text{OH}+\text{OH}+\text{m}$	4.30E+16	0	45500
32	$\text{H}_2+\text{OH}=\text{H}_2\text{O}+\text{H}$	1.17E+09	1.3	3626
33	$\text{HO}_2+\text{HO}_2=\text{H}_2\text{O}_2+\text{O}_2$	2.00E+12	0	0
34	$\text{CH}_2\text{O}+\text{OH}=\text{HCO}+\text{H}_2\text{O}$	5.56E+10	1.1	-76.5
35	$\text{CH}_2\text{O}+\text{HO}_2=\text{HCO}+\text{H}_2\text{O}_2$	3.00E+12	0	8000
36	$\text{HCO}+\text{O}_2=\text{HO}_2+\text{CO}$	3.30E+13	-0.4	0
37	$\text{HCO}+\text{m}=\text{H}+\text{CO}+\text{m}$	1.59E+18	0.9	56712.3
38	$\text{CH}_3+\text{CH}_3\text{O}=\text{CH}_4+\text{CH}_2\text{O}$	4.30E+14	0	0
39	$\text{C}_2\text{H}_4+\text{OH}=\text{CH}_2\text{O}+\text{CH}_3$	6.00E+13	0	960
40	$\text{C}_2\text{H}_4+\text{OH}=\text{C}_2\text{H}_3+\text{H}_2\text{O}$	8.02E+13	0	5955
41	$\text{C}_2\text{H}_3+\text{O}_2=\text{CH}_2\text{O}+\text{HCO}$	4.00E+12	0	-250
42	$\text{C}_2\text{H}_3+\text{HCO}=\text{C}_2\text{H}_4+\text{CO}$	6.03E+13	0	0
43	$\text{C}_2\text{H}_5+\text{O}_2=\text{C}_2\text{H}_4+\text{HO}_2$	2.00E+10	0	-2200
44	$\text{CH}_4+\text{O}_2=\text{CH}_3+\text{HO}_2$	7.90E+13	0	56000

45	$\text{OH} + \text{HO}_2 = \text{H}_2\text{O} + \text{O}_2$	7.50E+12	0	0
46	$\text{CH}_3 + \text{O}_2 = \text{CH}_2\text{O} + \text{OH}$	3.80E+11	0	9000
47	$\text{CH}_4 + \text{H} = \text{CH}_3 + \text{H}_2$	6.60E+08	1.6	10840
48	$\text{CH}_4 + \text{OH} = \text{CH}_3 + \text{H}_2\text{O}$	1.60E+06	2.1	2460
49	$\text{CH}_4 + \text{O} = \text{CH}_3 + \text{OH}$	1.02E+09	1.5	8604
50	$\text{CH}_4 + \text{HO}_2 = \text{CH}_3 + \text{H}_2\text{O}_2$	9.00E+11	0	18700
51	$\text{CH}_4 + \text{CH}_2 = \text{CH}_3 + \text{CH}_3$	4.00E+12	0	-570
52	$\text{C}_3\text{H}_6 = \text{C}_2\text{H}_3 + \text{CH}_3$	3.15E+15	0	85500

$$k = AT^b \exp(-E / RT)$$

A units mole-cm-sec-K, E units cal/mole

Table 2.4.2 Reactions for NOx [77].

NO.	REACTIONS	A	b	E
1	$N+NO=N_2+ O$	1.90E+11	0	3400
2	$N+O_2=NO + O$	1.80E+14	0	76100
3	$N_2O+O=2NO$	9.00E+09	1	6500
4	$N_2O+OH=N_2+ HO_2$	9.64E+14	0	148300
5	$N_2O + m=N_2 + O + m$	3.00E+11	0	65000
6	$HO_2+ NO=NO_2+ OH$	1.26E+12	0	62620
7	$NO+ O + m=NO_2 + m$	1.00E+14	0	28200
8	$NO_2+ O=NO + O_2$	6.92E+13	0	26630
9	$NO_2+ H=NO + OH$	1.00E+13	0	20000

$$k = AT^b \exp(-E / RT)$$

A units mole-cm-sec-K, E units cal/mole

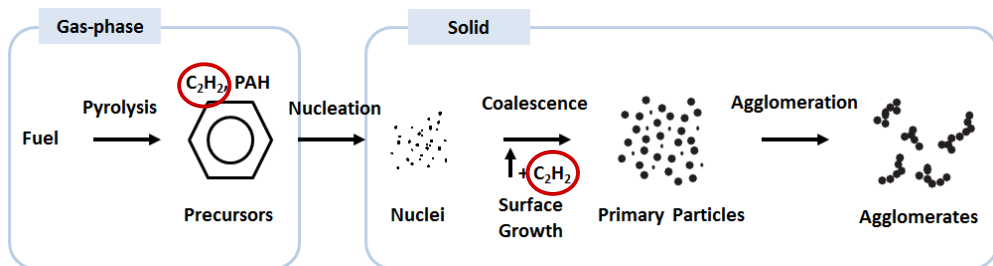


Figure 2.4.1 Schematic diagram of the steps in the soot formation process [80].

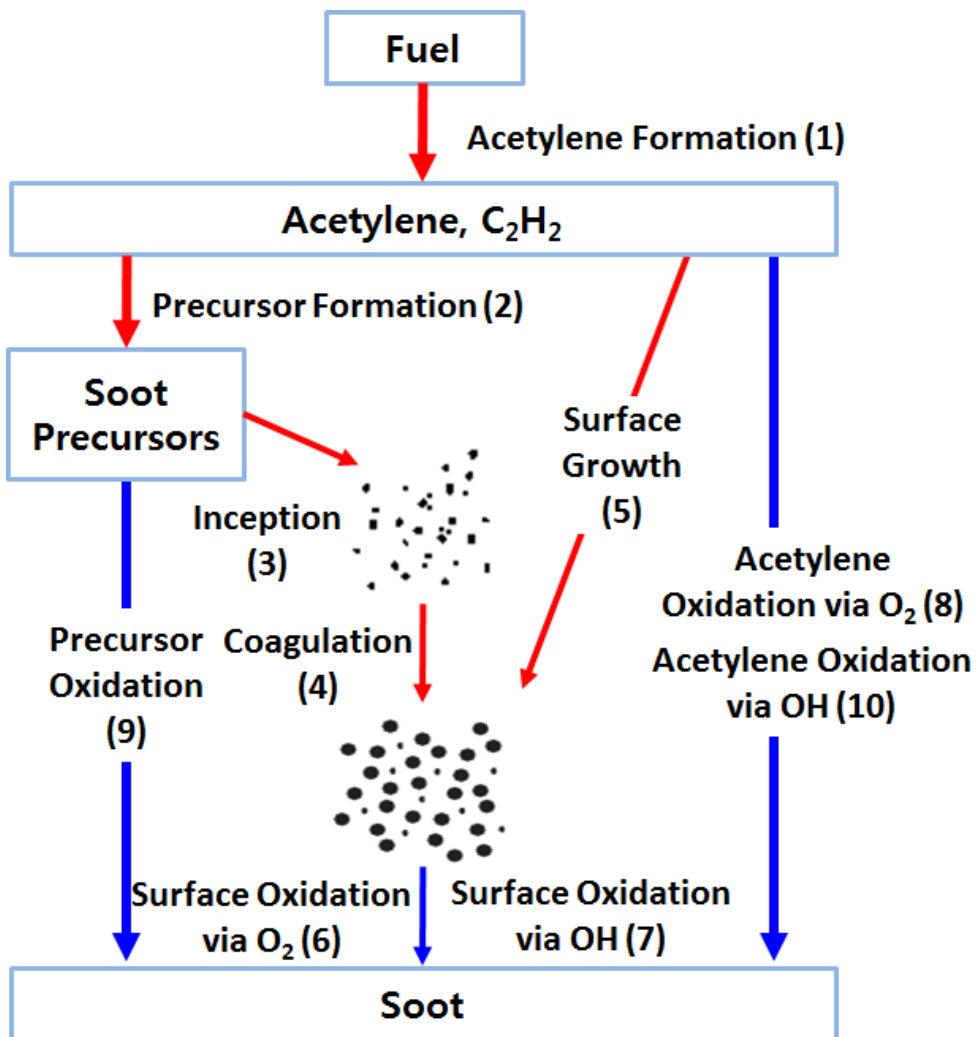


Figure 2.4.2 Schematic of the ten-step phenomenological soot model.

Chapter 3. Combustion Model for Stratified EGR Distribution in a Diesel Engine

3.1 Concept of the FSE Model

3.1.1 Concept of the FSE model

The concept of the combustion model for stratified EGR distribution is using multiple flamelet models based on the multi zone concept. This model is named to the Flamelet for Stratified EGR (FSE) model.

As shown in Figure 1.3.3 and Figure 1.3.4, EGR is distributed non-uniformly in the combustion chamber at the end of the compression stroke. To solve this non-uniform (stratified) gas distribution, the combustion chamber is divided several zones, as shown in Figure 3.1.1, by oxygen concentration at start of injection (SOI). In this study, the oxygen concentration is selected as a standard of dividing zones. Although EGR rate is most important factor at in-cylinder EGR stratification, EGR rate is not suitable as the standard of dividing zone because the composition of EGR gas is changed according to the AFR. The composition of EGR gas, when $\phi \leq 1$, can be obtained as [5]

$$O_{2,EGR} = \frac{1 - \phi}{(1 - \varepsilon)\phi + 1 + \psi} \quad (3.2.1)$$

$$N_{2,EGR} = \frac{\psi}{(1 - \varepsilon)\phi + 1 + \psi} \quad (3.2.2)$$

$$CO_{2,EGR} = \frac{\varepsilon\phi}{(1-\varepsilon)\phi + 1 + \psi} \quad (3.2.3)$$

$$H_2O_{EGR} = \frac{2(1-\varepsilon)\phi}{(1-\varepsilon)\phi + 1 + \psi} \quad (3.2.4)$$

where ψ is the molar N/O ratio of the air, 3.773 and ϕ is fuel/air equivalence ratio. ε is calculated as follows:

$$\varepsilon = \frac{4}{4 + y} \quad , \quad (3.2.5)$$

where y is the molar H/C ratio of the fuel and it has the value 1.8 in Diesel fuel.

The composition of in-cylinder gas, which is calculated from fresh air, external EGR, and residual gas by using Eq. (3.2.6), is different according to the AFR even the same EGR rate condition.

$$X_i = (1 - X_b) \times X_{i,Air} + X_b \times X_{i,X_b} \quad (3.2.6)$$

where X_i is the volume fractions and i denotes O_2 , CO_2 , H_2O , and N_2 respectively. And X_b is the burned gas fraction of the combustion chamber as

$$X_b = \frac{m_{EGR} + m_r}{m_{total}} = \left(\frac{EGR}{100} \right) (1 - X_r) + X_r \quad (3.2.7)$$

where X_r , m_{EGR} , m_r , and m_{total} correspond to the residual gas fraction, the EGR mass, the residual mass, and the total mass of the in-cylinder gas, respectively.

Figure 3.1.2 shows the procedure of calculating the FSE model. When injection starts, the oxygen concentration of each cell is saved and the code estimate minimum and maximum oxygen concentration. Then, cells are grouped several zones according to the each cell's oxygen concentration at SOI. Zoning

process is performed at SOI only once and the oxygen concentration of SOI plays a role as a conserved scalar. Flamelet equation is solved at each boundary of the zone therefore the total number of (N+1) flamelet equations will be solved if there is the total number of N zones. So, the total number of (N+1) solutions of species mass fraction, $Y_{i,n}$ is obtained. The flamelet calculation is carried out at every time step and the data exchange processes between flamelet code and CFD code are the same with the RIF model. Final species mass fraction of each cell is calculated by linear interpolating between the solutions of each zone's boundary. Then the code returns the species mass fraction of each cell to the STAR-CD, and STAR-CD calculate the temperature of each cell.

The key point of this FSE model is to determine the number of zones and their boundary oxygen concentrations. The accuracy of prediction may increase as increasing the number of zones. Increasing the number of zones means that the difference between oxygen concentrations of zone boundary is reduced and the accuracy is increased. However, increasing the number of zones prolongs the computational time for flamelet calculation as the number of flamelet model is equal to the number of zones plus one. Therefore, considering the computational cost, the strategy for dividing zones should be optimized. In the following chapter, the strategy for dividing zones will be explained in more detail.

3.1.2 Strategy for dividing zones

As explained above, the key point of this combustion model is to determine the number of zones and their boundary oxygen concentrations. The strategy for dividing zones should be optimized with considering the accuracy and the computational cost. As this study focused on the emission reduction particularly NO_x and soot, the strategy for dividing zones is based on the characteristics of emission formation. Moreover, soot model which was explained in Chapter 2.4.3 is the phenomenological model, and soot is a passive scalar which means that soot

does not take part in the reactions. Therefore, soot formation is calculated at the end of each time step using the species which have been calculated from chemical reactions. As soot does not take part in the reactions, the zone strategy is based on the characteristics of NO_x formation.

Figure 3.1.3 shows the measured NO_x according to the oxygen concentration of SOI under various operating conditions. These results were obtained from a 2.2L conventional Diesel engine experiments and the operating conditions covered the new European driving cycle (NEDC) operating points and the swing of the EGR rate and main injection timing. Figure 3.1.4 shows predicted NO_x according to the oxygen concentration under variable EGR rate at the condition of 2000 rpm bmep 6 bar. The part shown in box with solid line is high EGR and low oxygen concentration area. So, the amount of NO_x emission is very low and the relation between NO_x and oxygen concentration can be assumed linear. Moreover, the area, where the oxygen concentration is less than 14 %, is heavy EGR region, so, the amount of NO_x emission is only the order of dozens ppm. Therefore, in this study, one zone is put where the oxygen concentration is less than 14 %. And there is another one zone the area between 14 % and 16 % of oxygen concentration, as the area shows still low amount of NO_x and linear relation according to oxygen concentration. On the other hand, the area over 20 % of oxygen concentration, which is shown in dotted box of Figure 3.1.4, exist low EGR region. In this area, in-cylinder stratification does not work well as there is not enough EGR gas for stratification.

The area between 16 % and 20 % of oxygen concentration is important to divide zones as NO_x emission increase exponentially according to oxygen concentration. As explained 3.1.1, the final species mass fraction of each cell is calculated by linear interpolating between the solutions of each zone's boundary. Therefore, the minimum number of zones and interval of boundaries should be found for linear interpolation between two boundaries.

3.1.3 Optimization and validation of the zone strategy

To find the optimal number of zones and the interval of boundary oxygen concentrations, simulations are carried out and the boundary oxygen concentration of each zones are varied by spaced 1 % to 0.01 %.

Figure 3.1.5 shows artificially distributed oxygen in the combustion chamber at 10 ° BTDC. The oxygen gas is linearly distributed from 18 % of oxygen to 20 % of oxygen (mass fraction). Other gases such as CO₂, H₂O, and N₂ are also linearly distributed proportionally to the O₂. 18 % of O₂ means about 39 % of EGR and 20 % of O₂ means about 24 % of EGR at AF 26. To consider this in-cylinder stratification condition, the boundary oxygen concentration of each zones are varied by spaced 1 % to 0.01 %, and the number of zones are varied from 2 to 200.

Figure 3.1.6 shows the pressure, temperature, and NO_x curves during the combustion under variable zone boundaries and number of zones conditions. The pressure and temperature are almost the same irrelevantly to the number of zones (boundary O₂). However, NO_x shows different prediction results when the number of zones is small. Nevertheless, the NO_x results are converged over 10 zones (0.2 % of oxygen mass fraction), and the trend of NO_x is well predicted under 10 zones. Figure 3.1.7 shows the calculation time for 60 CAD (10 ° BTDC ~ 50 ° ATDC). The red line indicates CFD calculation time of STAR-CD and the blue line indicates total elapsed time including calculation time of STAR-CD and FSE code. Total elapsed time increases as increasing the number of zones, but the elapsed time is similar under 20 zones. It is thought that non-linear relationship between 2, 4, and 10 zone cases occurs due to different performances of computational machines. On the other hand, the CFD time is almost constant irrelevantly to the number of zones.

From these results, it is concluded that zone which has 0.2 % of boundary oxygen concentration and number of zones less than about 20 zones are a good standard of dividing zones considering both accuracy and computational cost.

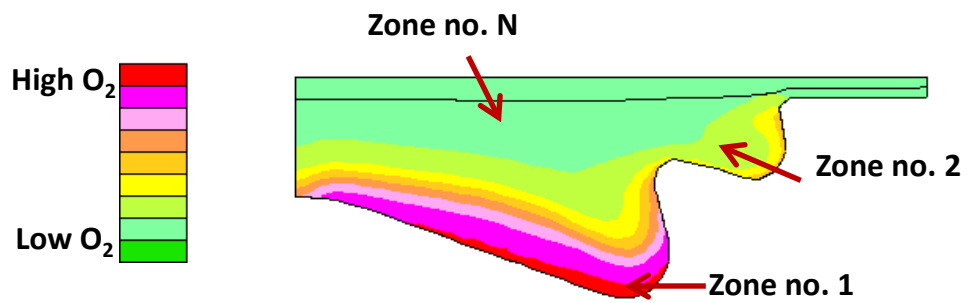


Figure 3.1.1 Combustion chamber which is divided zones by oxygen concentration.

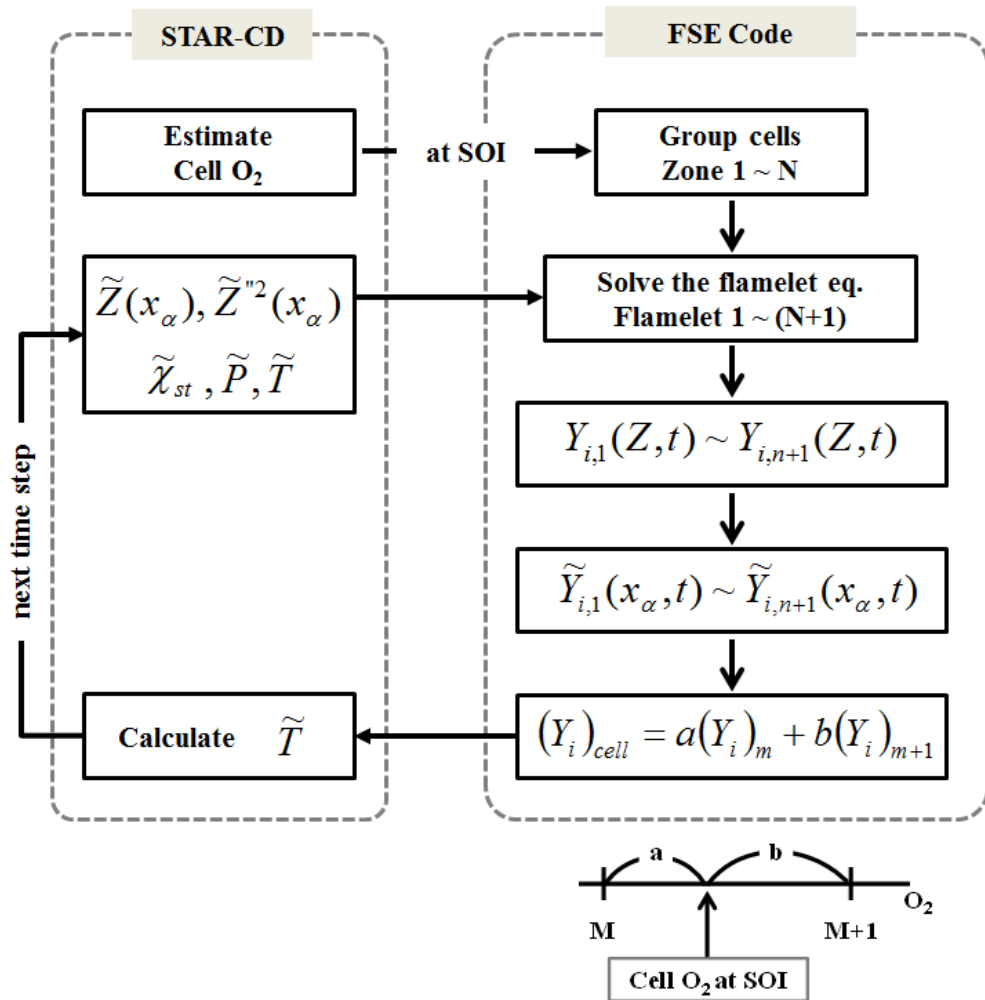


Figure 3.1.2 The procedure of calculating the combustion model for non-uniform EGR distribution.

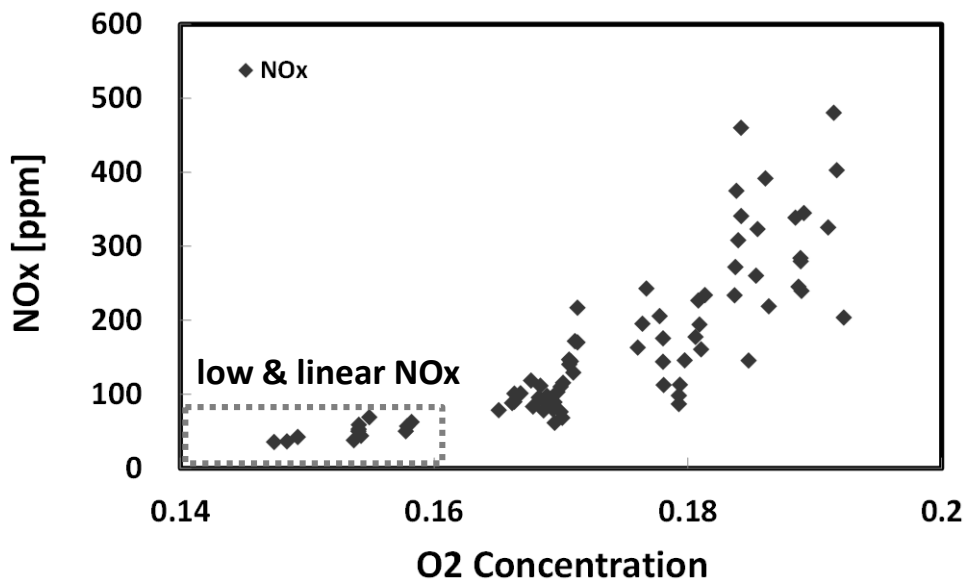


Figure 3.1.3 Measured NOx according to the oxygen concentration under conventional Diesel engine operating conditions.

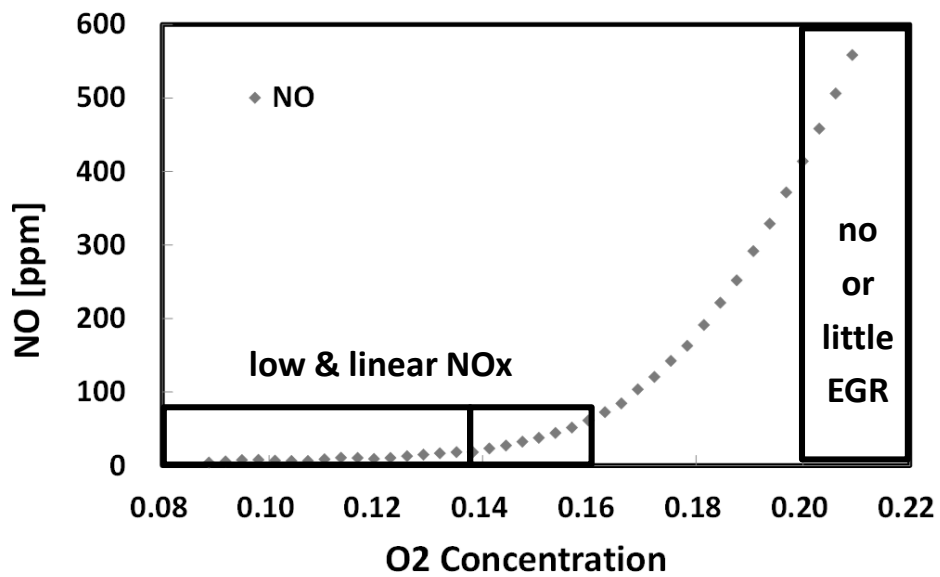


Figure 3.1.4 Predicted NOx according to the oxygen concentration under variable EGR rate at the condition of 2000 rpm bmep 6 bar.

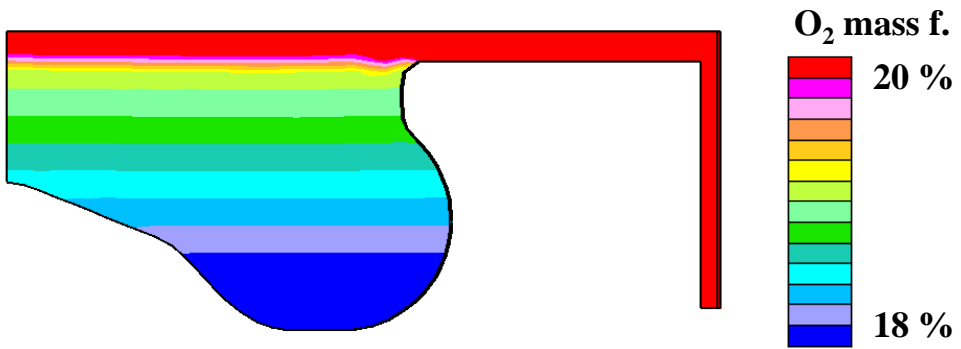


Figure 3.1.5 Artificially distributed oxygen in the combustion chamber for optimizing the number of zones.

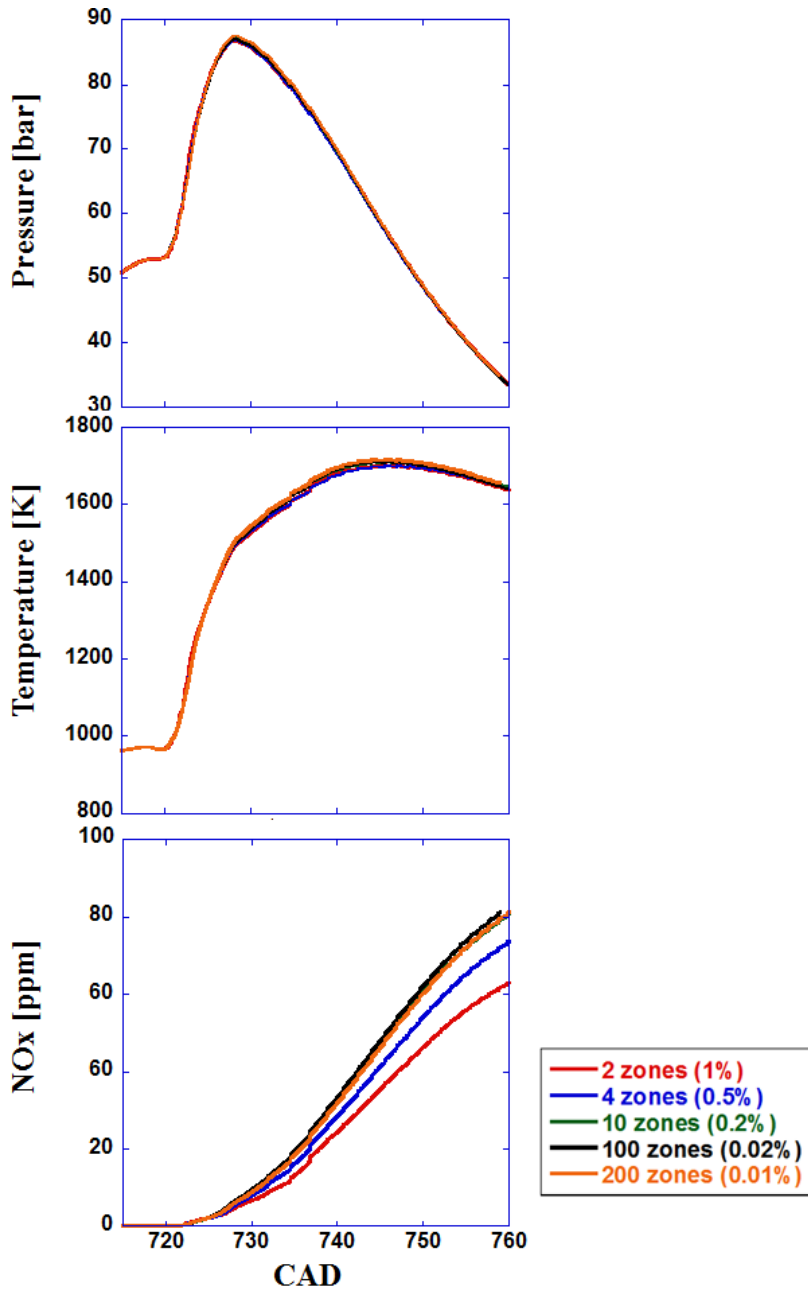


Figure 3.1.6 Pressure, Temperature, and NOx according to CAD under variable number of zones.

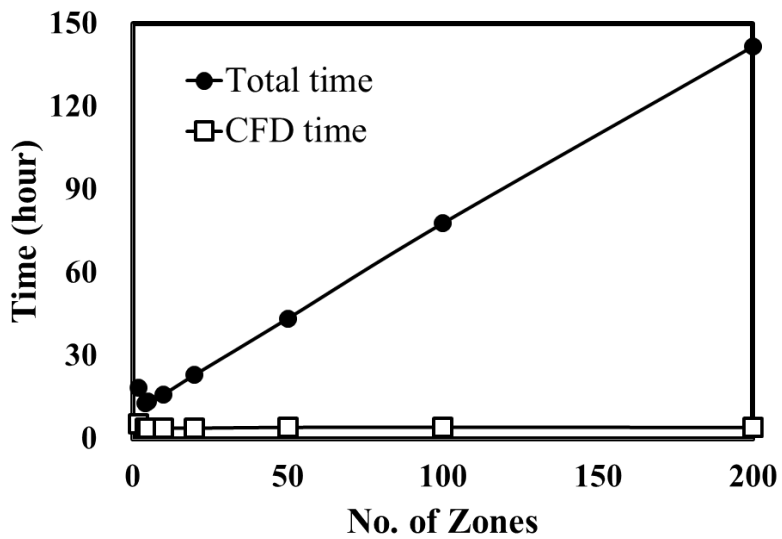


Figure 3.1.7 Calculation time during 60 CAD of simulation, total elapsed time (calculation time for STAR-CD and FSE code) and CFD time (calculation time for STAR-CD).

3.2 Verification of the Flamelet Model

As the FSE model is developed based on the flamelet model, the flamelet model is firstly validated with the experimental results.

3.2.1 Experimental and computational setup

A four-cylinder direct injection Diesel engine as shown in Figure 3.2.1 was used for experiment. This engine has a fuel injection equipment (FIE) including a piezo injector, a common rail, and a high pressure pump. Detailed specifications of engine and fuel injection equipment are shown in Table 3.2.1 and Table 3.2.2, respectively. The test engine was connected to a 340 kW AC dynamometer which is able to operate both steady-state operations and transient state operations with the dynamometer controller (AVL, PUMA). Oil and coolant temperature were controlled during the engine test using the PID controller, equipped in dynamometer control system. The quality of Diesel was preserved from a large capacity fuel tank during the entire experiment period and fuel temperature was maintained to 40 °C using the fuel temperature controller. The environment temperature of the engine test cell was controlled by an air-conditioning system.

O₂ and CO₂ from exhaust gas and NO_x, THC, CO, and soot emissions were measured during the engine experiment. NO_x, THC, CO, CO₂, and O₂ were measured by the exhaust gas analyzer (HORIBA, MEXA-7100DEGR). All species were measured in volume fraction in wet condition and the measurement principles of each emission are listed in Table 3.2.3. soot emission was measured by the smoke meter and DMS-500. The specification of the smoke meter is shown in Table 3.2.4 and the specification of the DMS-500 is listed in Table 3.2.6. The DMS-500 is used for soot measurement as the DMS-500 can measure the mass of soot and the number density of it. To monitor the AFR easily during the test, an AFR

analyzer, as shown in Table 3.2.6, was installed at the exhaust manifold. It has an O₂ sensor and calculates AFR by the O₂ balance equation. And the AFR was also calculated by using measured O₂, CO₂, CO and THC from following Spindt equation [5]:

$$AFR = \frac{(CO_2 \times 10000 + CO)}{(CO_2 \times 10000 + CO + THC)} \times (AA + BB) \quad (4.1.2)$$

where,

$$AA = \frac{11.4919 \times FC \times \left(1 + \frac{CO / (CO_2 \times 10000)}{2} + \frac{O_2}{CO_2}\right)}{\left(1 + \frac{CO}{(CO_2 \times 10000)}\right)} \quad (4.1.3)$$

$$BB = \frac{119.8074 \times (1 - FC)}{\left(3.5 + \frac{CO}{(CO_2 \times 10000)}\right)} \quad (4.1.4)$$

$$FC = \frac{12.011}{(12.011 + 1.008 \times HC_ratio)} \quad (4.1.5)$$

Pressures of each intake port and in-cylinder were measured to provide simulation the boundary conditions and to validate the computational models. The in-cylinder pressure was measured by relative pressure transducer 6055Bsp (the specifications are listed in Table 3.2.7) through the glow plug type adapter and amplified by charge amplifier, Kistler, 5019 A. The pressures of the intake ports were measured by absolute pressure transducer 4045A5 (the specifications are listed in Table 3.2.8) and amplified by piezo-resistive amplifier, Kistler, 4603. Signals from pressure transducers were recorded at every 1 CAD for 200 cycles for one case by using a data acquisition (DAQ) system. Analog signals were converted to digital by a DAQ board (the specifications are listed in Table 3.2.9) and recorded

by the in house data acquisition program. Relative pressure of cylinder was offset based on the absolute pressure of intake port at BTDC, which is called 'paging'.

For the CFD simulation a sector mesh representing 1/8th of the combustion chamber was used taking advantage of the axial symmetry of the centrally located 8-hole injector. The computational grid is shown in Figure 3.2.2 at BDC and it has approximately 64,565 cells at BDC and 16,125 cells at TDC. The calculation starts at the intake valve closing time, and the initial conditions are obtained from the experimental results.

The commercial CFD code, STAR-CD version 4.16 was used for the CFD simulations and the combustion models, flamelet model and FSE model were coupled with the STAR-CD by using user subroutines. The turbulence, chemistry, emission, and break-up models are explained in detail at Chapter 2 and the sub-models for simulation are listed in Table 3.2.10.

3.2.2 Results and discussion

The flamelet model was validated with the experimental results using the experimental apparatuses described in Chapter 3.2.1. Moreover, the ten-step phenomenological soot model was also verified and compared with the nine-step phenomenological soot model.

At first, a reference condition with 25 % EGR was applied to the experiment and simulation. The detailed operating conditions of experiment and simulation are listed in Table 3.2.11. Figure 3.2.3 shows the measured and predicted pressure curves according to the CAD of the simulation and experimental results. The ignition delay, peak pressure, and pressure trace of predicted results from the simulation agreed well with the measured results.

During the next step, various EGR conditions were applied to verify the emission trends. The EGR rate was varied as 20 %, 25 %, 30 %, and 35 %. The predicted NO_x and soot were compared to the measured emissions. As shown in Figure 3.2.4, the NO_x results of the simulation agreed well with those of the experimental results. NO_x decreased with increasing applied EGR in both the simulation and experimental results. Figure 3.2.5 shows the comparisons of soot mass and number density. The results of the 10-step soot model show good agreement with the experimental results and better prediction than the nine-step soot model, especially in soot number density results. On the basis of these results, the combustion and emission models used in this study could be useful tools to describe Diesel engine combustion and emissions in EGR conditions.

3.2.3 Comparison between the FSE model and the flamelet model

As explained in Chapter 1.3, EGR gas distributes non-uniformly in the combustion chamber even it is supplied uniformly through the intake port because of the residual gas. To consider the non-uniform EGR distribution in the combustion chamber, the simulation starts at intake valve open (IVO) and the mesh was generated including the intake and exhaust port. Figure 3.2.6 shows the computational grid for validation, and the grid was made using trimmed mesh method of the es-ice, which is a volume mesh generation tool within the STAR-CD package. To reduce computational time, exhaust ports were removed after exhaust valve close (EVC) and intake ports were also removed after intake valve close (IVC). Figure 3.2.6 (a) shows the grid with intake and exhaust ports at BDC (about 670,000 cells) and Figure 3.2.6 (b) shows the grid without ports at firing TDC (about 71,000 cells).

Figure 3.2.7 shows the oxygen distribution in the combustion chamber at SOI (5 ° BTDC). The minimum oxygen mass fraction is 0.181 and the maximum oxygen mass fraction is 0.188. The red region of Figure 3.2.7 means that there

exists high oxygen and low EGR gas and the blue region means that there exists low oxygen and high EGR gas. To solve the FSE model five zones with six boundaries were used. Figure 3.2.8 shows CO₂, NO_x, and soot distributions of the results of the FSE model and the flamelet model. As the conventional flamelet model cannot describe the spatial distribution of in-cylinder gas, the result shows only one value of CO₂ at the timing when the injection starts unlike the FSE model. Therefore the FSE model and the flamelet model predict NO_x and soot distributions differently. The FSE model predicts more NO_x than the flamelet model at upper side of the combustion chamber due to locally low EGR gas, while the model predicts less NO_x at bottom side of the combustion chamber because of locally high EGR gas. In case of soot, there exists difference between the models in distributions and the amounts; however the difference is not shown clearly unlike NO_x.

Table 3.2.1 Engine specifications.

Description	Specification
Engine Type	In-line 4 cylinder 2.2 L
Max power	200 hp / 3800 RPM
Max torque	44.5 kgm / 1800 RPM~2500 RPM
Bore x Stroke (mm)	85.4 x 96
Displacement (cc)	2200
Compression Ratio	16
Con. Rod Length (mm)	165
Valve Timing	IVO : 10 ° BTDC
	IVC : 28 ° ABDC
	EVO : 54 ° BBDC
	EVC : 4 ° ATDC

Table 3.2.2 FIE specifications.

Description	Specification
Fuel injector type	Piezoelectric type
Manufacturer	Bosch
No. of Nozzle Holes	8
Spray Angle	156 °
Nozzle Diameter (mm)	0.143

Table 3.2.3 The principle of measurement by the emission analyzer.

Emissions	Measurement principle
NO _x	Chemiluminescent Detector
THC	Flame Ionization Detector
O ₂ , CO ₂ , CO	Non Dispersive Infrared Rays

Table 3.2.4 The specifications of the smoke meter.

Item	Specification
Manufacturer	AVL
Model	AVL 415S
Measurement range	0 ~ 10 FSN / 0 ~ 32,000 mg/m ³
Resolution	0.001 FSN / 0.01 mg/m ³
Repeatability (as standard deviation)	$\sigma \leq \pm(0.005 \text{ FSN} + 3 \% \text{ of measured value})$
Reproducibility (as standard deviation)	$\sigma \leq \pm(0.005 \text{ FSN} + 6 \% \text{ of measured value})$

Table 3.2.5 The specifications of the DMS-500

Item	Specification
Particle Size Range	5 nm – 1 µm (5 nm – 2.5 µm option)
Number of Electrometers	22
Size Classification	Electrical Mobility
Dilution Factor Range	1 – 3000
Maximum Primary Dilution Temperature	150 °C
Sample Flow rate	8 slpm (1 µm range) at 0 °C + 100 kPa
Instrument Zeroing	Automatic; internal HEPA filter
Spectral Elements	16 or 32/decade
Output Data Rate	10/sec – 1/min
Time Response	T 10–90 % 200 ms T 10–90 % 300 ms with 5m heated line
Calibrations: Non-agglomerate: Agglomerate (Diesel):	By NIST traceable PSL spheres & DMA size selected NaCl/H ₂ SO ₄ , comparison with standard electrometer DMA size selected soot, comparison with standard electrometer
Calibration Interval	12 months
Max Concentration	≈10 ¹¹ dN/dlogD /cc (diluter on)

Table 3.2.6 The specifications of the AFR analyzer.

Item	Specification
Manufacturer	HORIBA
Model	MEXA-110λ
Measurement range (H/C = 1.85)	A/F 10.0 ~ 30.0
Accuracy (H/C = 1.85)	±0.3 A/F when 12.5 A/F ±0.1 A/F when 14.7 A/F ±0.5 A/F when 23.0 A/F
Exhaust gas temperature (°C)	-7 ~ 900 (recommend 200 ~800)

Table 3.2.7 The specifications of the in-cylinder pressure transducer.

Item	Specification
Manufacturer	Kistler
Model	6055Bsp
Pressure sensor type	Relative pressure
Measuring range (bar)	0 ~ 250
Overload (bar)	300
Linearity (% FSO)	< ±0.4
Sensitivity (pC/bar)	-18.3
Natural frequency (kHz)	160
Operating temperature (°C)	-20 ~ 350

Table 3.2.8 The specifications of the intake port pressure transducer.

Item	Specification
Manufacturer	Kistler
Model	4045A5
Pressure sensor type	Absolute pressure
Measuring range (bar)	0 ~ 5
Linearity (% FSO)	< ± 0.3
Natural frequency (kHz)	> 80
Operating temperature ($^{\circ}\text{C}$)	20 ~ 120 (compensated)

Table 3.2.9 The specifications of analog inputs of DAQ board.

Item	Specification
Manufacturer	IOtech
Model	Wavebook 512A
Channels	8 differential
Resolution	12 bit
Ranges (V)	Unipolar : 0 ~ +10, 0 ~ +4, 0 ~ +2 Bipolar : ± 10 , ± 5 , ± 2 , ± 1
Maximum Overvoltage (VDC)	± 35
Input Bandwidth	DC to 500 kHz
Input Impedance	Single-Ended: 5M Ohm in parallel with 30 pF Differential: 10M Ohm in parallel with 30 pF
Accuracy	$\pm 1\text{V}$ to $\pm 10\text{V}$: ± 0.03 % of reading; 0.012 % of range
Operating	0 ~ 50 $^{\circ}\text{C}$, 0 ~ 95 % RH, non-condensing

Table 3.2.10 The sub-models for CFD simulations [61].

Description	Model
CFD code	STAR-CD v.4.16
Turbulence	κ - ε RNG
Atomization	Reitz-Diwakar
Nozzle	Effective
Droplet break-up	Reitz
Droplet-wall interaction	Bai

Table 3.2.11 The conditions for validation.

Description	Model
Engine Speed	1500 rpm
bmep	6 bar
EGR rate	20, 25, 30, 35 %
Inj. pressure	665 bar
Inj. timing	5 ° BTDC
Inj. mass	22.3 mg



Figure 3.2.1 A four-cylinder Diesel engine.

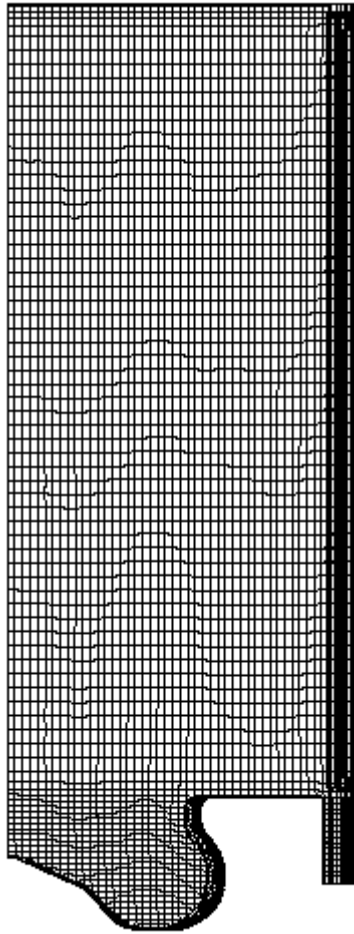


Figure 3.2.2 The Computational grid with the two-step piston at BDC (1/8 sector).

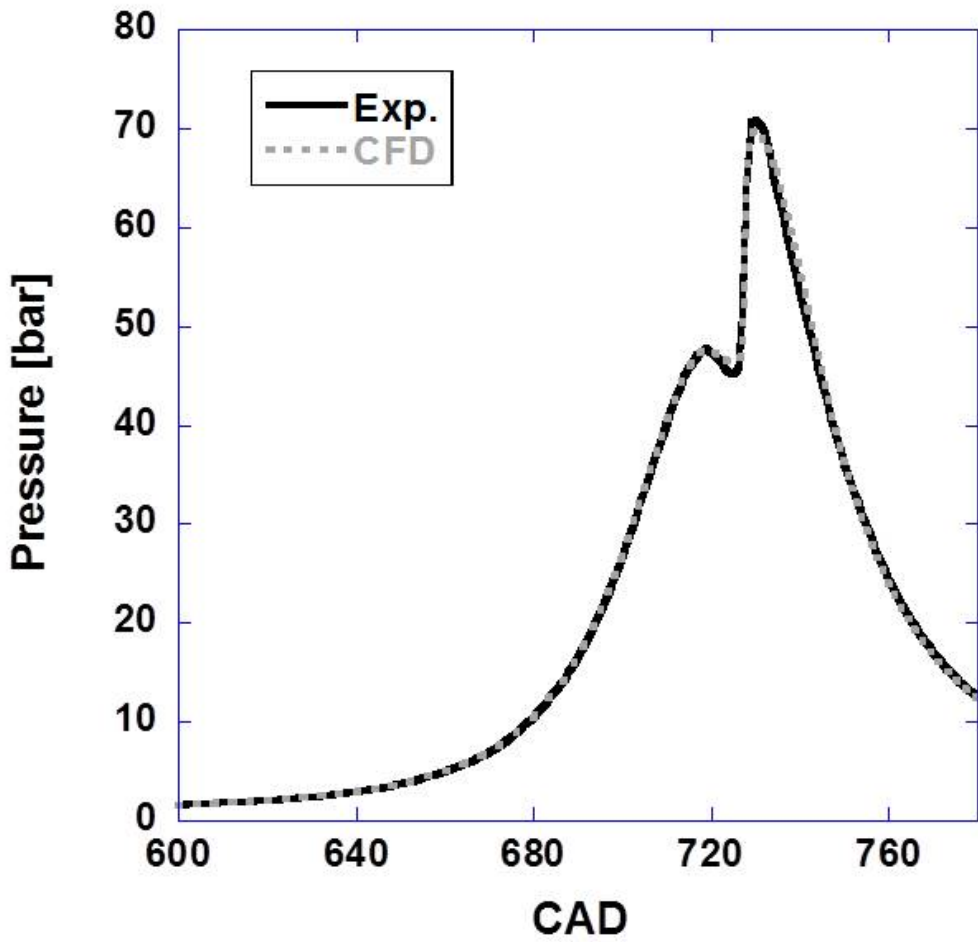


Figure 3.2.3 Pressure curves as a function of the CAD of the predicted result and measured data.

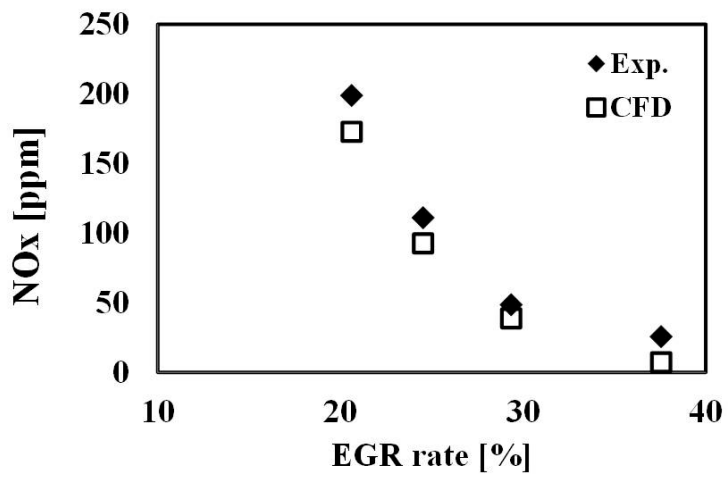


Figure 3.2.4 Comparison of the predicted results with measured data: NO.

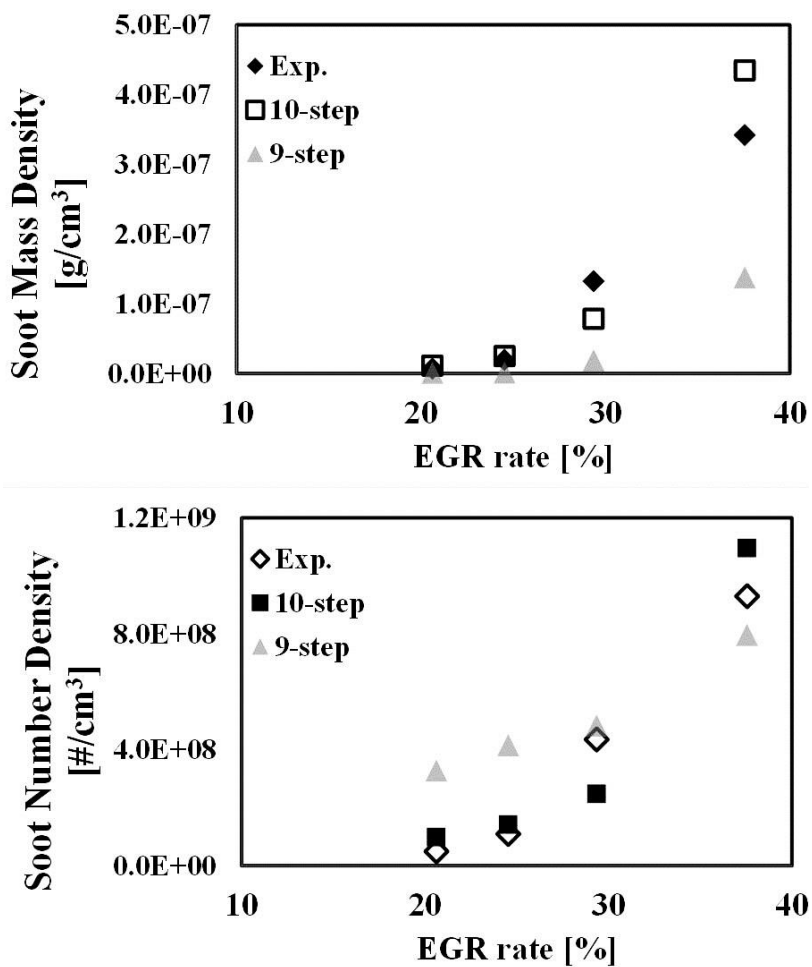


Figure 3.2.5 Comparison of the predicted results with measured data: soot mass density (top) and soot number density (bottom).

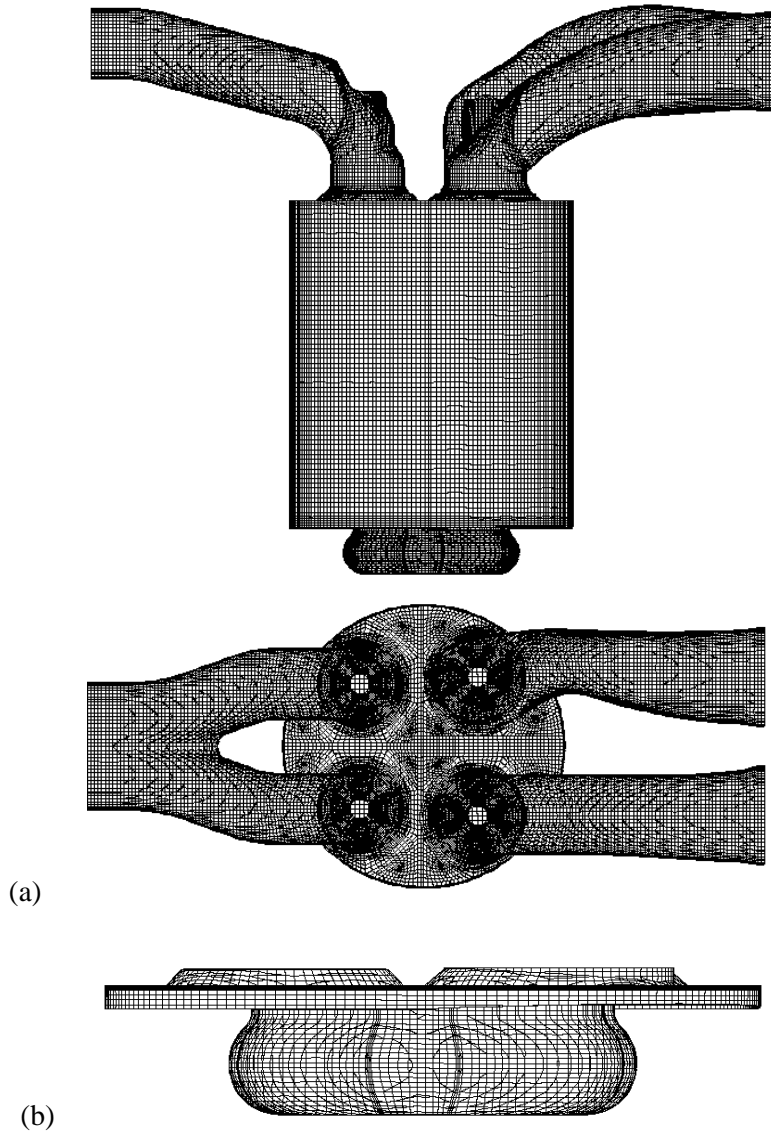


Figure 3.2.6 The computational grid (a) at BDC with intake and exhaust ports (b) at TDC without ports.

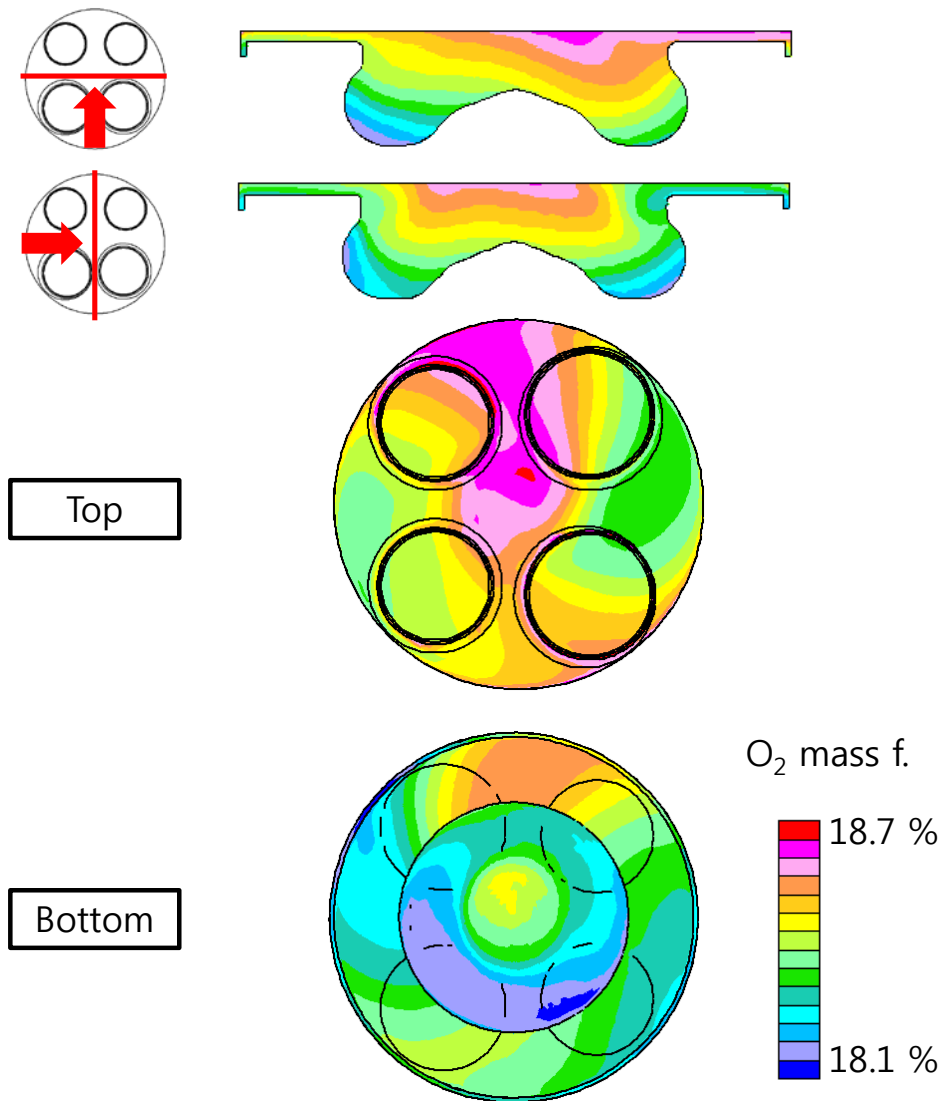


Figure 3.2.7 Oxygen distribution in the combustion chamber at 10° BTDC.

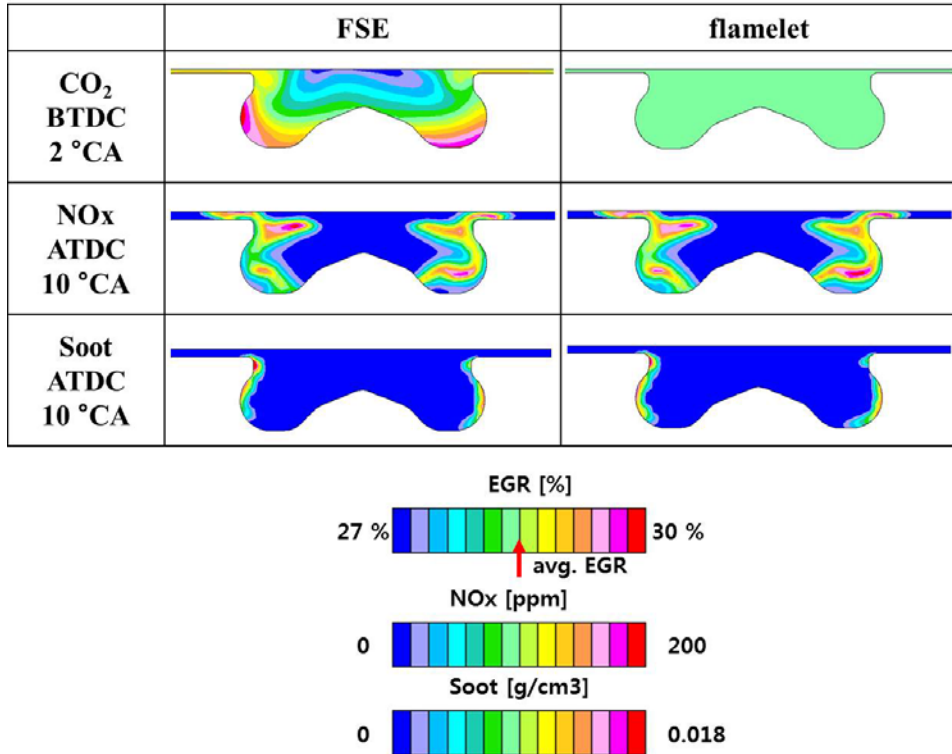


Figure 3.2.8 CO₂, NO_x, and soot distributions of the FSE model and the flamelet model.

3.3 Verification of the FSE Model

In this chapter, the FSE model is validated with the experimental results under in-cylinder EGR stratification condition.

3.3.1 Experimental and computational setup

A single-cylinder direct injection Diesel engine as shown in Figure 3.3.1 was used for stratified EGR combustion experiment [28, 90]. This engine has fuel injection equipment (FIE) including a piezo injector, a common rail and a high pressure pump, which enables injection pressure up to 1,600 bar. FIE was controlled by Bosch ECU version of EDC 16. Detailed specifications of the engine and fuel injection equipment are shown in Table 3.3.1 and Table 3.3.2, respectively. The test engine was connected to a 37 kW DC dynamometer for engine speed control and torque measurement. The specifications of dynamometer are listed in Table 3.3.3. Oil and coolant temperature were controlled during the engine test using the PID controller, equipped in dynamometer control system. The quality of Diesel was preserved from a large capacity fuel tank during the entire experiment period and fuel temperature was maintained to 40 °C using the fuel temperature controller (SAMBU, SFTC-140). The temperature of the engine test cell was controlled by an air-conditioning system. The exhaust gas emissions were measured by using the same systems which described in Chapter 3.2.1.

To realize EGR stratification in the single cylinder engine experiment, a special intake runner was designed, which can supply EGR to only left or only right port asymmetrically as shown in Figure 3.3.2 [90]. To measure temperature, pressure and gas composition, a thermocouple, a pressure transducer and a gas sampling line were installed in each side of runner. The EGR supply method for in-cylinder EGR stratification is shown in Figure 3.3.3. In conventional EGR supply, EGR is supplied to the most upstream of the runner before the separated point. In

this case, fresh air and external EGR are well mixed and the left and right intake ports have the same gas composition. In stratified EGR (S-EGR), EGR is supplied to the EGR inlet of left port. So the left port has the composition of high EGR. In contrast, only air is supplied to the right port.

To consider the non-uniform EGR distribution in the combustion chamber, the simulation starts at IVO and the mesh is generated including the intake and exhaust port. Figure 3.3.4 shows the computational grid for validation. To reduce computational time, exhaust ports are removed after EVC and intake ports are also removed after IVC. The engine operating conditions were 1500 rpm, bmep 4 bar, and single injection (5 ° BTDC). EGR rate were changed from 28 % to 44 % by 8 % increase.

3.3.2 Results and discussion

Figure 3.3.5 shows comparisons of the predicted results with measured data under in-cylinder EGR stratification conditions (EGR supplied method is described in Figure 3.3.3 S-EGR). The FSE model shows good prediction both NO_x and soot.

Figure 3.3.6 shows the effect of in-cylinder EGR stratifications. B-EGR means EGR and fresh air are supplied at well-mixed as shown in Figure 3.3.3 B-EGR and S-EGR. From the measured data, S-EGR shows 4.3 % of NO_x reduction and 25.7 % of soot reduction compared with the B-EGR, and from the predicted results S-EGR shows 2.4 % of NO_x reduction and 37.2 % of soot reduction compared with the B-EGR. The rates of emission reduction of experiment and FSE model are not exactly the same but both show similar trend and simultaneous reduction of NO_x and soot.

Table 3.3.1 Engine Specifications [28, 90].

Description	Specification
Engine Type	4-stroke DI
Bore x Stroke (mm)	83 x 92
Displacement (cc)	497
Compression Ratio	15.5
Con. Rod Length (mm)	145.8
Valve Timing	IVO: 7 ° BTDC
	IVC: 43 ° ABDC
	EVO: 52 ° BBDC
	EVC: 6 ° ATDC

Table 3.3.2 FIE (Fuel injection equipment) Specifications [28, 90].

Description	Specification
Manufacturer	Bosch
No. of Nozzle Holes	7
Spray Angle	153 °
Nozzle Diameter (mm)	0.128
HFR (cc/100 bar/30 s)	380
High Pressure Pump (Max. P)	CP3.2 (1,600 bar)
ECU Version	EDC 16 P373_V60

Table 3.3.3 Dynamometer specifications [28, 90]

Description	Specification
Manufacturer	DAVID McClure LIMITED
Model	G-Cussions
Capacity	37 KW
Type	DC
Max. rpm	7,000
Cooling type	Air cooling
Weight	396 kg



Figure 3.3.1 Single cylinder Diesel engine [28, 90].

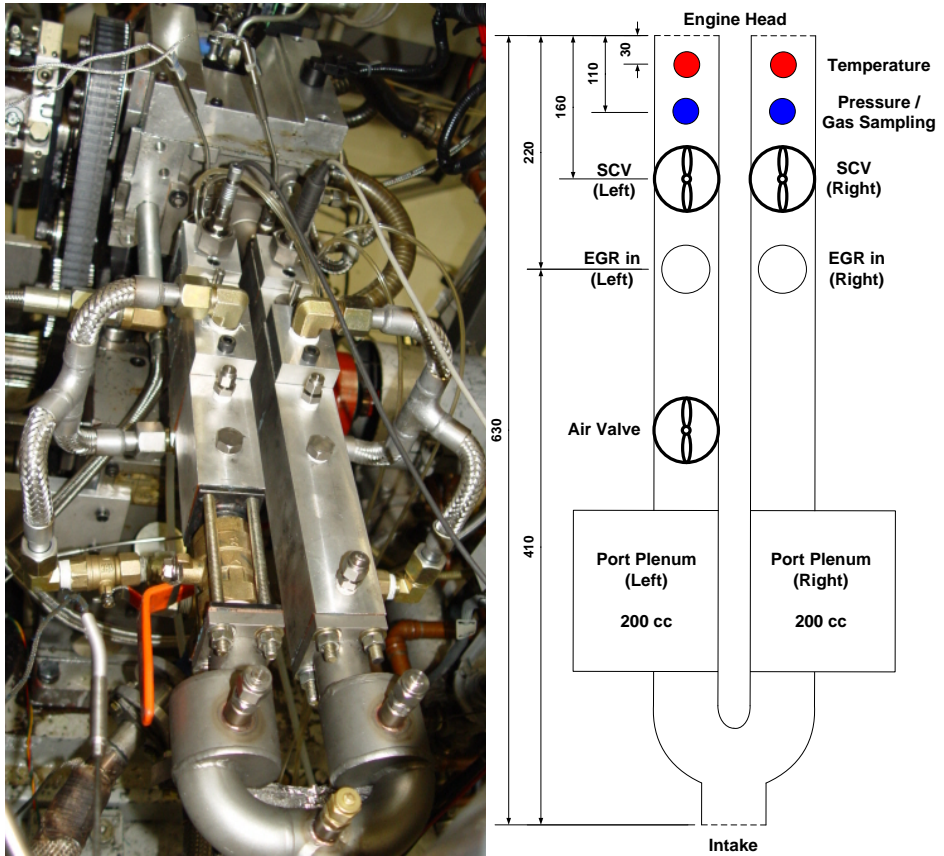


Figure 3.3.2 Picture (left) and simple figure (right) of intake runner [28, 90].

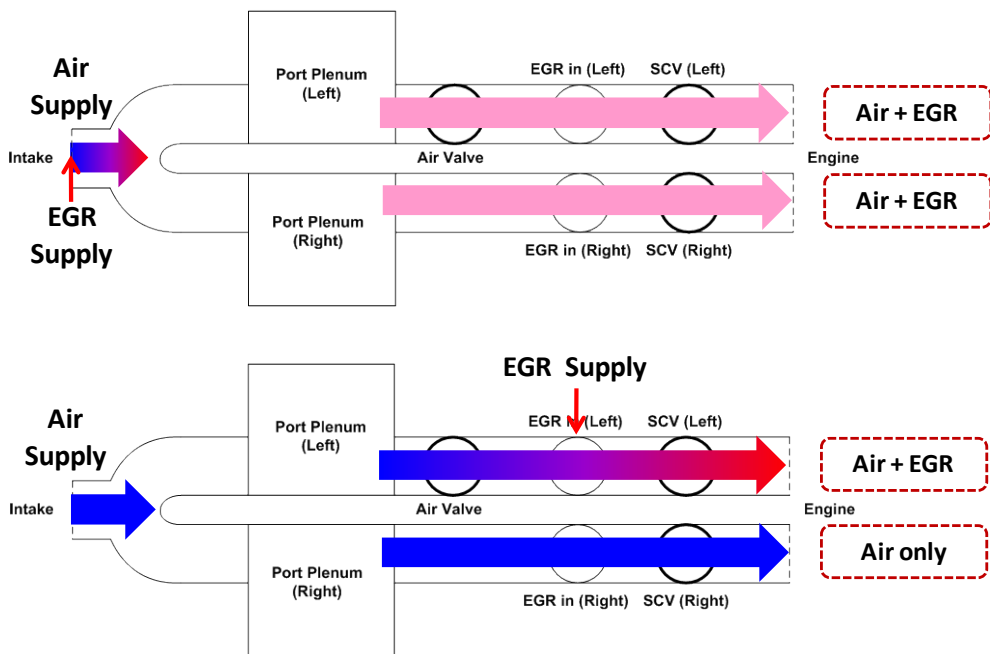


Figure 3.3.3 EGR supply methods: conventional EGR (B-EGR, up) and stratified EGR (S-EGR, down) [28, 90].

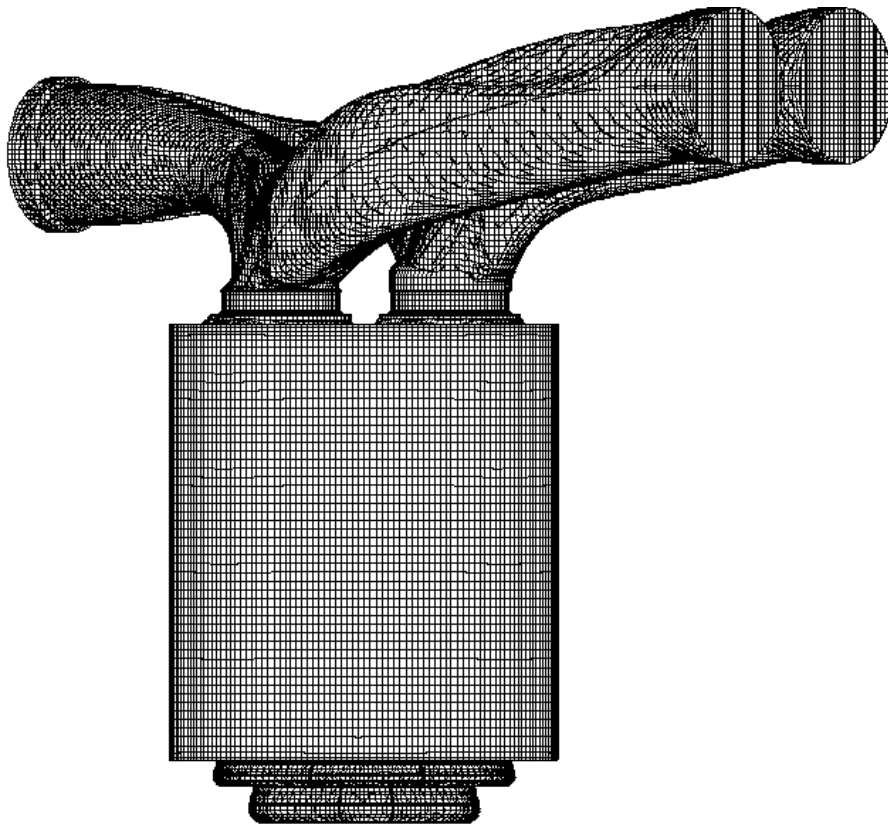


Figure 3.3.4 The Computational grid with the two-step piston at BDC.

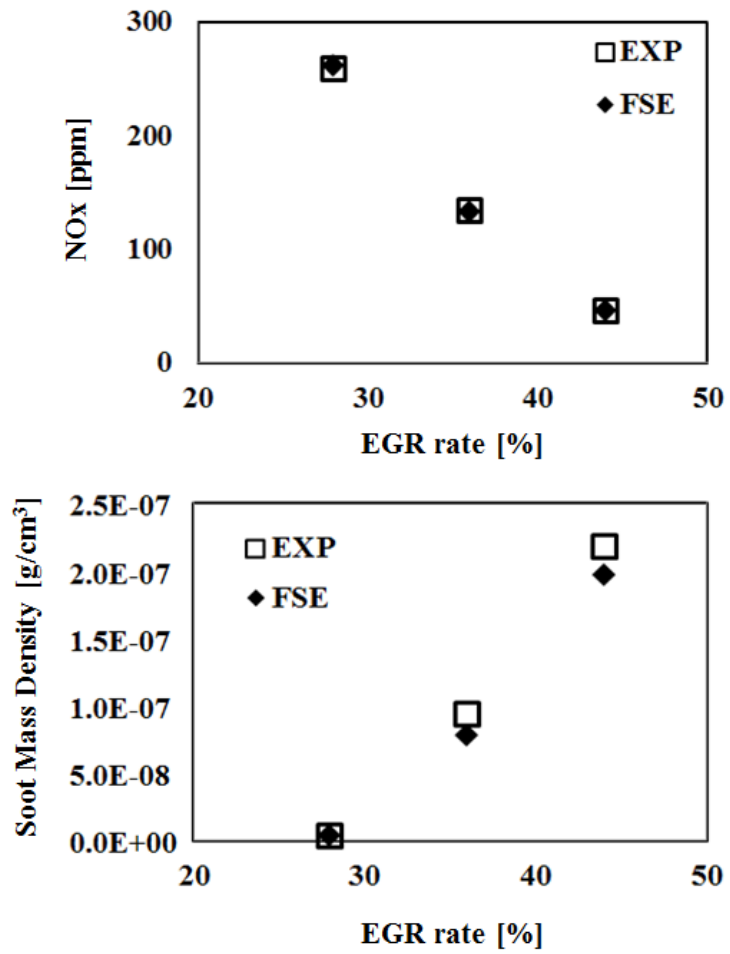


Figure 3.3.5 Comparison of the predicted results with measured data: NOx (top) and soot mass density (bottom).

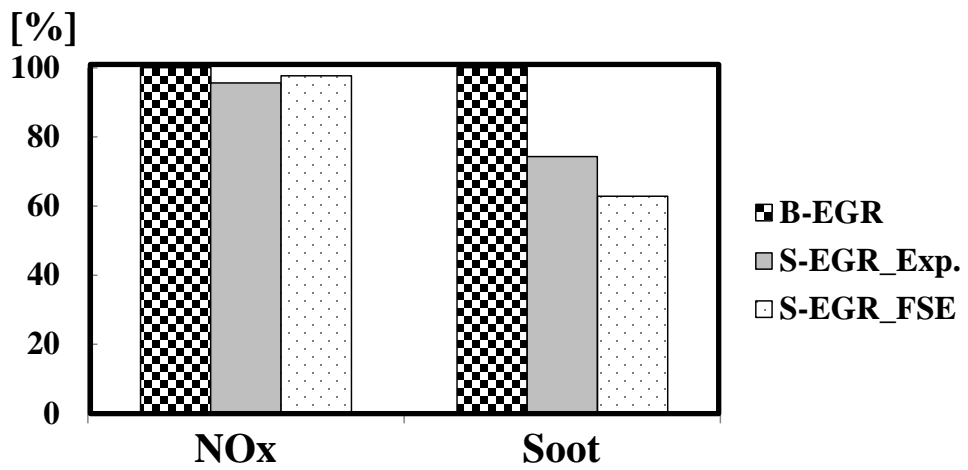


Figure 3.3.6 Comparison of the predicted results with measured data: the effect of in-cylinder EGR stratification.

Chapter 4. Application of the FSE Model

In this chapter, the FSE model applied to investigate the potential of in-cylinder EGR stratification.

4.1 Implementation of In-cylinder EGR Stratification to a Diesel Engine

To achieve simultaneous reduction of NO_x and soot, EGR gas has to be distributed at desirable location of the combustion chamber. However, it is not easy to control the position of the incoming gases during the intake and compression strokes because the velocity of the incoming gases is very fast, and turbulent flow is strong in the cylinder. The easiest way to separate the incoming gases into the EGR gas and fresh air is to supply them separately. Generally, there are two intake ports in conventional Diesel engines (the top view of the Diesel engine is shown in Figure 4.1.1). Figure 4.1.1 also shows the supply method of external EGR gas for EGR stratification. In this configuration, the in-cylinder EGR stratification can be achieved by an asymmetrical external EGR supply. This prevents the mixing of fresh air and EGR gas by supplying EGR gas through one port and fresh air through the other port. Simulation results like Figure 1.3.4 showed that in-cylinder EGR could be stratified via asymmetrical external EGR supply.

Two main concerns for in-cylinder EGR stratification are determining which EGR stratification pattern is the most favorable and determining how to inject fuel into the high EGR region. Park et al. carried out the engine combustion simulations to find out the favorable EGR stratification pattern and the possibility of combustion and emission control [22]. A one over seven sector mesh, which has about 16,000 cells at TDC and 54,000 cells at BDC, was constructed, and a cyclic boundary was applied for the symmetry shown in Figure 4.1.2. The ideal stratified

EGR distributions were formed artificially, as shown in Figure 4.1.3, and compared with the uniform EGR distribution case. The conventional (Figure 4.1.3 (a)) and two-step (Figure 4.1.3 (b)) pistons were used to verify the piston shape effects on combustion and emissions. The ideal S-EGR case 1 shows a locally high EGR rate in the upper region, and the ideal S-EGR case 2 shows a locally high EGR rate in the upper and center regions. The total EGR rate was 30 % for both the uniform and stratified EGR cases. The maximum EGR rate of the ideal S-EGR case 1 was 36.3 %, and that of the stratified EGR case 2 was 100 %.

NO and soot decreased in both stratified EGR cases with the two-step piston. NO decreased by 39 % in the ideal S-EGR case 1 and 7 % in the ideal S-EGR case 2. Soot decreased by 3 % in the ideal S-EGR case 1 and 49 % in the ideal S-EGR case 2. Under stratified EGR conditions, the emissions were not reduced in the same proportion, but the NO_x-soot trade-off relationship is avoidable. In the ideal S-EGR case 1, combustion starts in the high EGR region, so the ignition delay is prolonged, and the peak cylinder pressure and temperature are decreased. High NO reduction is achieved by the locally low oxygen concentration in the combustion region and the decrease in initial reaction rate, which decreases the peak cylinder pressure and combustion temperature. Soot generation increases because of the locally high EGR region, but soot oxidation also increases at the end of the reaction by mixing with the locally high oxygen region. In the ideal S-EGR case 2, combustion starts in the high oxygen region at the side of the first floor of the piston, so the ignition delay is shorter than in the U-EGR and the ideal S-EGR case 1. Moreover, because the region where combustion starts has locally high oxygen and additional soot oxidation occurs at the end of the reaction due to mixing with the locally high oxygen region, the soot decreases by approximately 50 %. The NO production rate is higher than the U-EGR at the first stage. However, the high concentration EGR gas in the center is mixed with the fuel during injection, and it suppresses NO generation.

From the previous research, it is concluded that the locally high EGR region due to EGR stratification effectively influences the combustion characteristics. Horizontally and centrally stratified EGR have the potential to reduce NO and soot emissions at the same time without compromising engine performance. However, ideal EGR distribution is not realistic in the actual engine flow condition. In the actual engine, EGR distribution in the combustion chamber is determined by an interaction between intake ports and a piston. Therefore, it is important to optimize the intake ports and the piston to obtain the favorable EGR stratification pattern. Choi et al. improved the EGR stratification pattern using the offset chamfer as shown in Figure 4.1.5. However, as they used a conventional engine head, the modification was limited. Moreover, for the fuel injection, fuel should not be spread over a piston as shown in Figure 4.1.6 (a). Choi et al. designed a two-step piston (Figure 4.1.6 (b)) and changed the chamfer shape of the intake port to obtain a favorable EGR distribution pattern and to inject fuel into the high EGR region, which increases the effects of EGR stratification on combustion and emissions [22, 90].

In this study, variable intake port, chamfer, and piston were designed to obtain the favorable EGR distribution pattern and to inject fuel into the high EGR region, for maximizing the effects of EGR stratification.

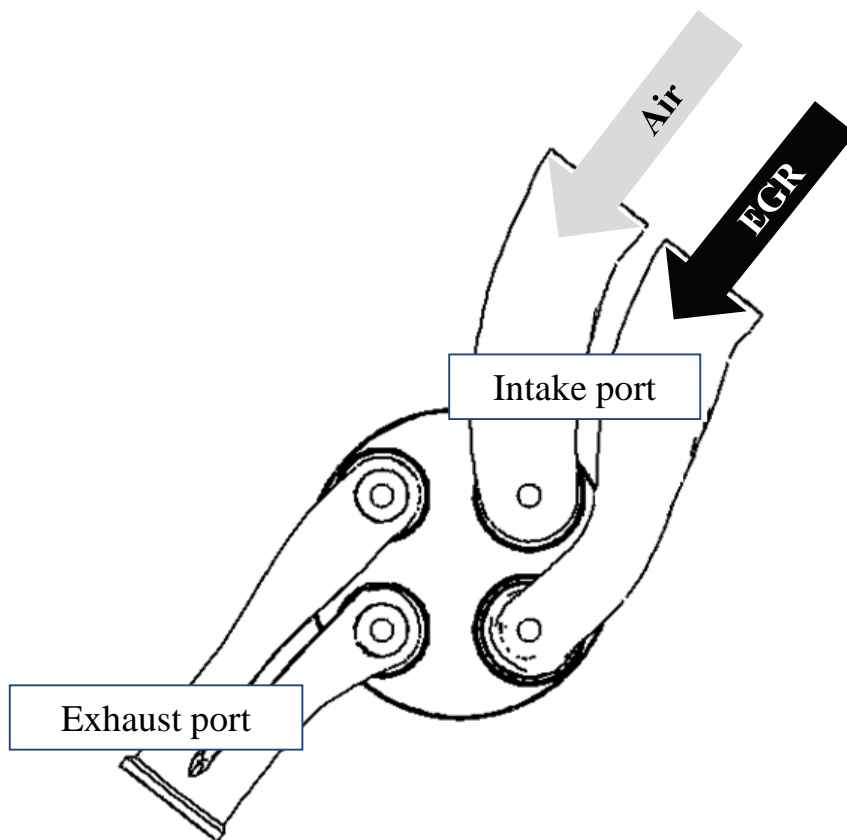


Figure 4.1.1 Top view of Diesel engine and the EGR supply method [22].

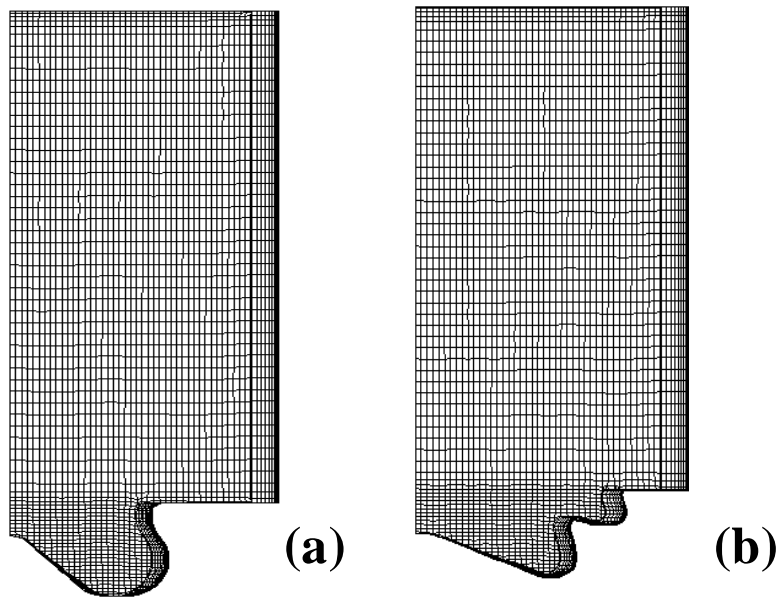


Figure 4.1.2 Shape of one over seven sector mesh (a) conventional piston (b) two-step piston [22].

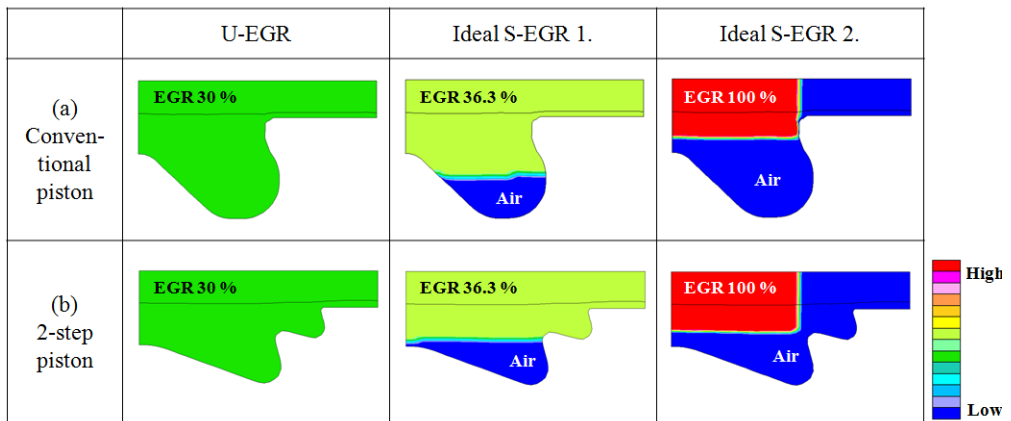


Figure 4.1.3 EGR distributions of each EGR case: (a) conventional piston, (b) two-step piston [22].

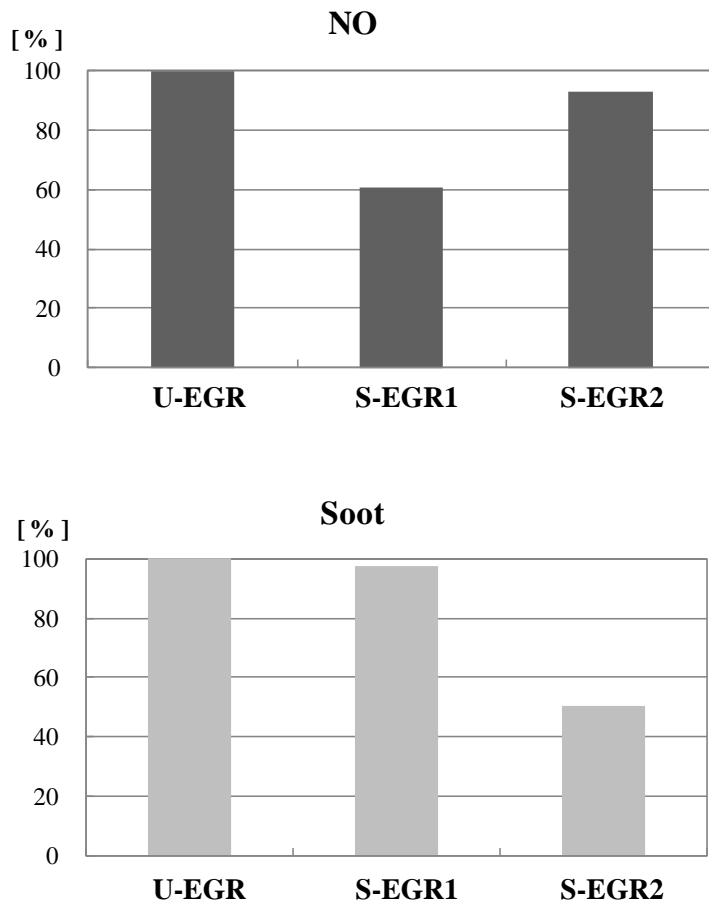


Figure 4.1.4 NO and soot reduction under Ideal S-EGR condition [22].

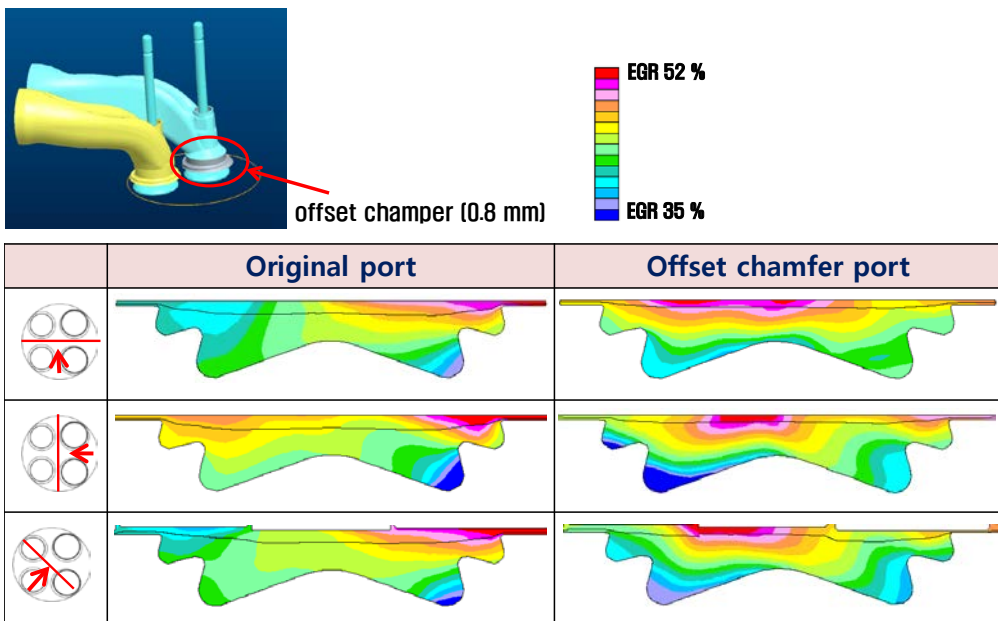


Figure 4.1.5 Change of the chamfer [90]

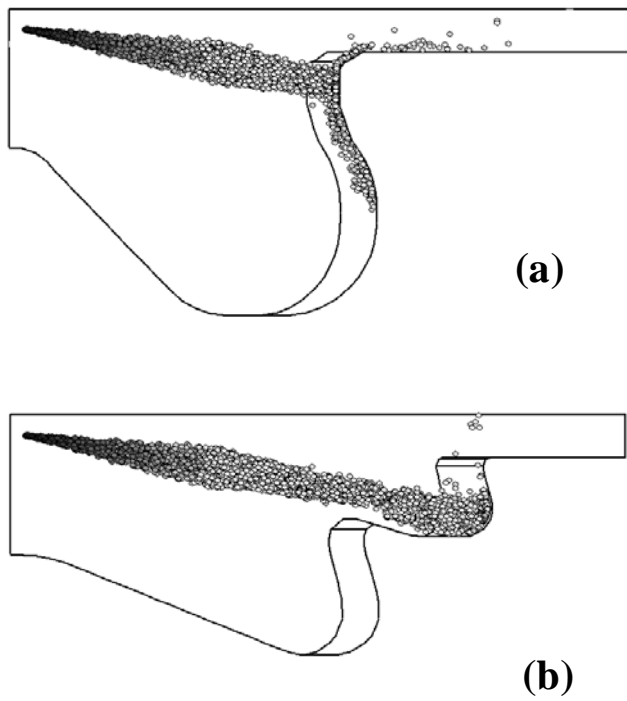


Figure 4.1.6 Droplet distributions: (a) the conventional piston and (b) the two-step piston [22].

4.2 Hardware Optimization

4.2.1 Intake port optimization

To achieve simultaneous reduction of NO_x and soot, EGR gas is distributed at a desirable location of the combustion chamber. To do this, it is need to prevent the mixing of fresh air and external EGR. Figure 4.1.1 shows the supply method of fresh air and external EGR gas for EGR stratification. This method can reduce the mixing of fresh air and EGR gas by supplying EGR gas through one port and fresh air through the other port. However, it is not easy to control the position of the incoming gases during the intake and compression strokes because the velocity of the incoming gases is very fast, and turbulent flow is strong in the cylinder. The location of the incoming gases is determined by interactions of the intake port, chamfer, and piston. Therefore, in this study, modifications of those parts were carried out to make the favorable EGR distribution.

As explained in Chapter 4.1, it was shown that horizontally and centrally stratified EGR have the potential to reduce NO_x and soot at the same time without compromising engine performance. To get horizontally and centrally stratified EGR, the EGR gas should be located in the center and upper region of the combustion chamber and the air should be placed in the bottom region of it. Therefore, an air supply port was designed as a straight type port to send air in the bottom region of the combustion chamber and an EGR supply port was a bended type port which has curvature to swirl-direction to place EGR gas in the upper region with increasing a swirl motion there to reduce the eccentricity of the EGR distribution. Figure 4.2.1 shows conceptual diagram of the intake ports and the gas supply.

Moreover, as the intake ports are located closely, even though the air and EGR are separately supplied, the air and EGR gas are mixing during the intake process as shown in Figure 4.2.2. To prevent mixing between fresh air and EGR gas, the

geometry of the intake chamfer was modified. Parameters of ports and chamfers are described in Figure 4.2.3. Five kinds of parameters for intake ports such as the curvature of EGR port, length of intake ports, height and angle of intake ports, and the position of valve center were varied. Then, three kinds of offset chamfer shape were tested.

From the parameter study, two different types of EGR supply ports with a straight type of an air supply port were designed as shown in Figure 4.2.4. Figure 4.2.4 (a) shows the bended type port with a helix shape and Figure 4.2.4 (b) shows the bended type port without a helix shape. To investigate the effect of port shapes on in-cylinder EGR distribution, CFD flow simulations were conducted under 1500 rpm EGR 35 % condition. Figure 4.2.5 shows CO₂ distributions at 10 ° BTDC with the helix shape intake port which is described in Figure 4.2.4 (a). As CO₂ is only from the EGR gas, the CO₂ distribution is same as the EGR distribution. And Case 1 to Case 3 show the effect of chamfer shapes. Case 3 shows better distributions than Case 1 and 2, but there still exists locally low EGR region at the right-upper side of the combustion chamber. As NO_x forms a lot at this locally low EGR region, it reduces the effect of the in-cylinder EGR stratification. Figure 4.2.6 shows a velocity distribution of Case 3 at 270 ° BTDC. To reduce the eccentricity of the EGR distribution, incoming EGR should move toward the ‘B’-direction which is described Figure 4.2.6, however, EGR gas moves toward ‘A’-direction because of the helix shape at the EGR port.

Figure 4.2.7 shows CO₂ distributions at 10 ° BTDC with the non-helix shape intake port which is described in Figure 4.2.4 (b) and the chamfer is the same with the Case 3 of Figure 4.2.5. The non-helix shape port shows lower degree of the EGR stratification than the helix shape port, but it shows better EGR distribution than the helix shape port. As shown in top view of Figure 4.2.7, there exists CO₂ over averaged CO₂ mass fraction (EGR rate) unlike top view of Figure 4.2.5 (there exist blue color region which means that the local CO₂ mass fraction is lower than the 85 % of the averaged CO₂ mass fraction).

4.2.1 Piston optimization

In Diesel engines, air motions such as swirl, squish flow, and turbulence play a very important role in fuel-air mixing, combustion, and emission formation during the fuel injection [5]. Swirl motion is firstly generated by the intake port design, then the swirl-squish interaction produces a turbulent flow field at the end of compression process [91, 92]. Most of the in-cylinder gas is compressed into a smaller diameter combustion chamber around TDC; as a result, the speed of rotation increases by conservation of angular momentum. Moreover, re-entrant chamber shows that the intensification of swirl and turbulence are higher than cylindrical chamber, so it leads higher NO_x and less soot and HC [92-94]. Therefore, in piston optimization, these air motions are important, and there are many researches about the effect of piston geometries on air motions and emission characteristics [95-97].

Park et al. suggested that the two-step piston to maximize the stratified EGR effects by obtaining a favorable EGR distribution pattern and injecting fuel into the high EGR region [22, 90]. The two-step piston shows the improved results of the EGR distribution on stratification as described in Figure 4.2.8. However, the two-step piston has a concave shape between the first floor and the second floor, as a results, it prevents mixing of gases which locate the first floor and the second floor during the expansion stroke. Moreover, as the swirl ratio of the two step piston is lower than that of the conventional piston, the two-step piston has disadvantage at soot formation. Therefore, in this study, new two-step pistons were designed and tested the effect on in-cylinder EGR stratification.

Parameters of the piston optimization are described in Figure 4.2.10 and Figure 4.2.11 shows geometries of (a) a conventional engine piston and (b-d) newly developed pistons. The newly developed pistons have a first and second floor, but the height and diameter of each floor is different. All these pistons have the same

volume, so they have a same compression ratio. To investigate the effect of piston geometries on in-cylinder EGR distribution, CFD flow simulations were conducted under 1500 rpm EGR 35 % condition and the non-helix shape intake port which is described in Figure 4.2.4 (b) was used. Figure 4.2.12 shows CO₂ distributions at 10 ° BTDC. Even though same intake port was used, the results show quite different CO₂ distributions according to the piston geometries.

Figure 4.2.13 shows swirl ratios and the swirl ratio can be defined as (dimensionless) [61],

$$\text{Swirl Ratio} = \frac{M_z}{I_z} = \frac{\sum_{cells} \rho_i V_i [(X_i - X_m)v_i - (Y_i - Y_m)u_i]}{2\pi \frac{N}{60} \sum_{cells} \rho_i V_i [(X_i - X_m)^2 + (Y_i - Y_m)^2]} \quad (4.2.1)$$

where:

X_i, Y_i, Z_i : Centroid coordinate of cell i [m]

X_m, Y_m, Z_m : Centre of mass of the cylinder [m]

u_i, v_i : Velocity at cell i [m/sec]

N : engine speed [rpm]

M_z : Angular momentum about the z-axis [kg·m²/sec]

I_z : Mass moment of inertia about the z-axis [kg·m²/sec].

The conventional piston has the highest swirl ratio near the TDC and Piston B > Piston C > Piston A are followed. Moreover, the two-step pistons show the higher swirl ratio than the conventional piston during the expansion stroke.

Combustion simulations were carried out investigating the effect of the pistons on emission reduction under 1500 rpm, 15 mg of fuel, and 25.0 % of external EGR rate. Figure 4.2.14 shows the method of fresh air and EGR gas supply. In case of B-EGR, external EGR and fresh air were well mixed and supplied through both intake

ports, while, in case of S-EGR, EGR gas was supplied through only one of the intake port. To investigate the effect of in-cylinder EGR stratification, other conditions such as the injection timing, fuel mass, boost pressure, etc. except gas supply method, were fixed. Moreover, the overall EGR rate of B-EGR and S-EGR in the combustion chamber were same even the EGR gas distributions were different.

Figure 4.2.15 shows the effect of the pistons on emission reduction under S-EGR compared with B-EGR. In case of NO_x, the Piston A, the Piston B, and the Piston C show the 19.3 %, 11.4 %, and 22.0 % of NO_x reduction respectably under S-EGR compared with B-EGR. The Piston C shows the largest NO_x reduction. In case of soot, the Piston A and the Piston B show 4.4 % and 12.7 % of soot increase compared with B-EGR and only the Piston C shows 17.8 % of soot decrease. Therefore, the Piston C was chosen as the optimized piston because the Piston A and the Piston B show trade-off relationship under in-cylinder EGR stratification conditions.

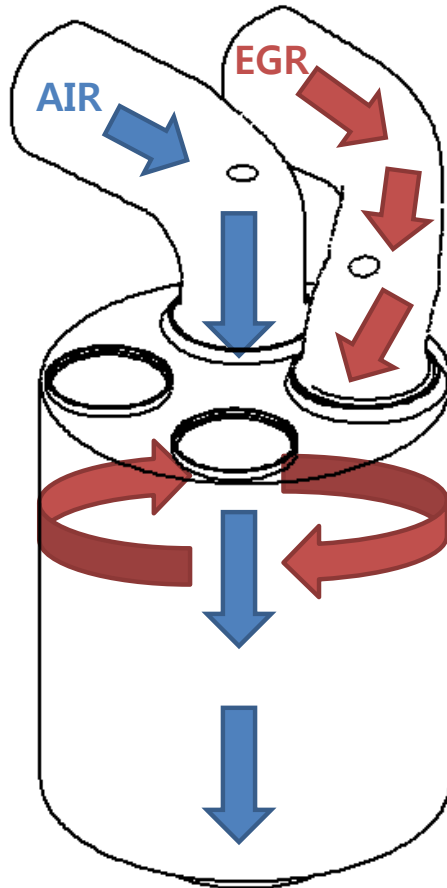


Figure 4.2.1 The concept of intake ports optimization.

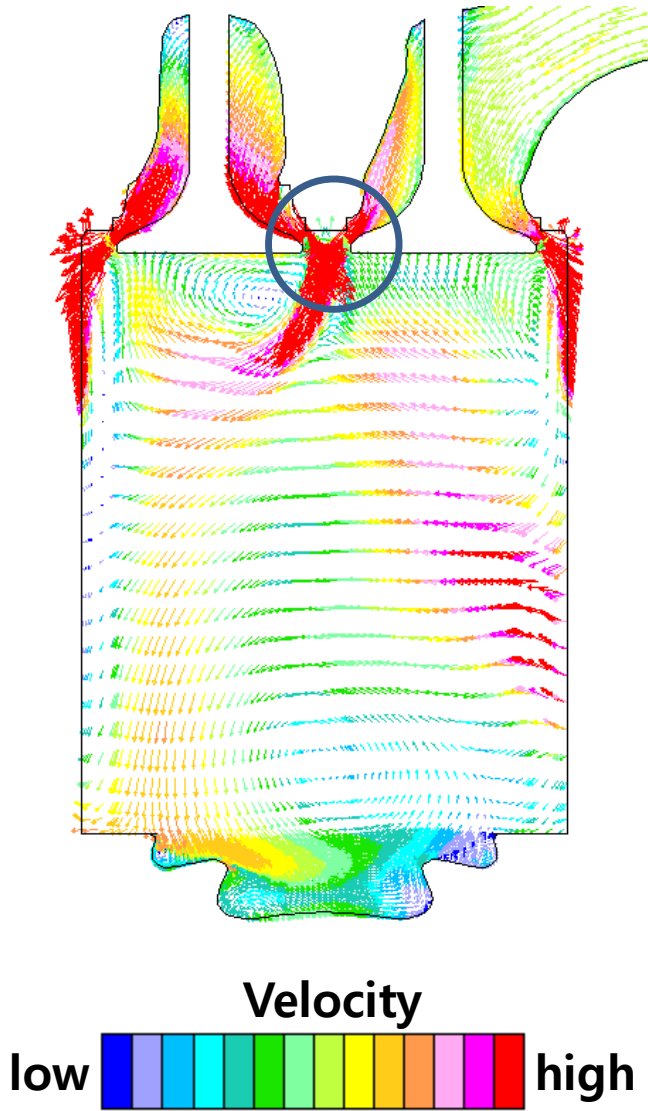


Figure 4.2.2 Velocity distribution at ABDC 90 °.

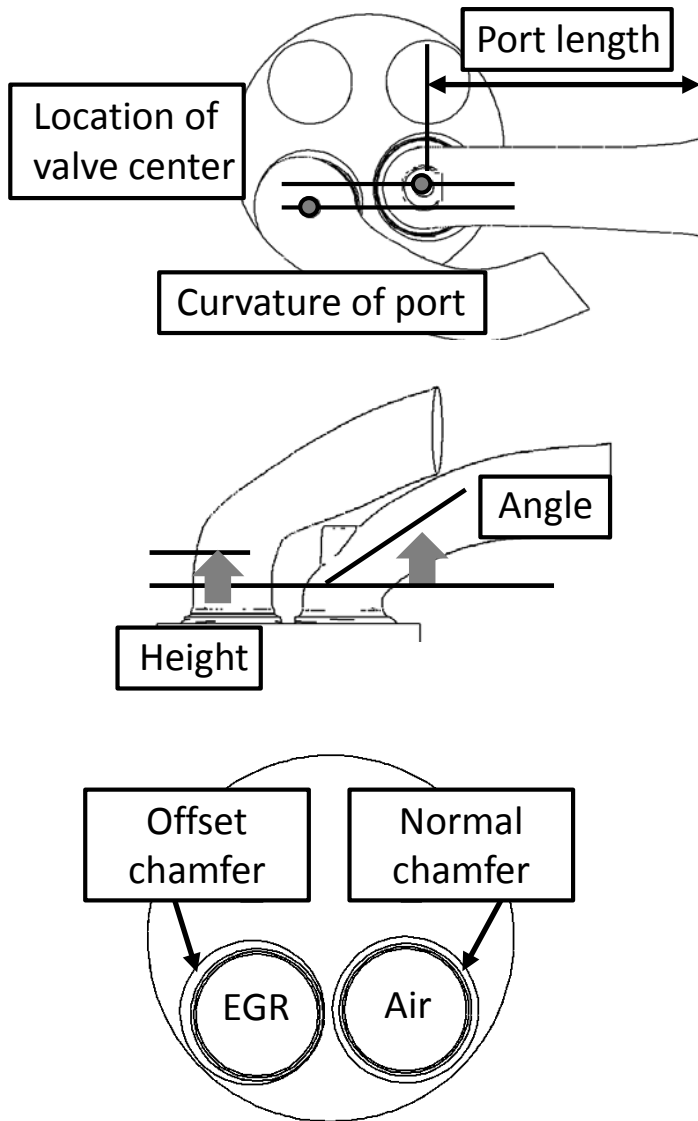


Figure 4.2.3 Parameters of ports and chamfers optimization

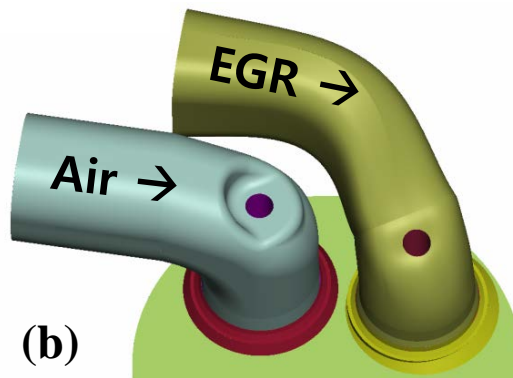
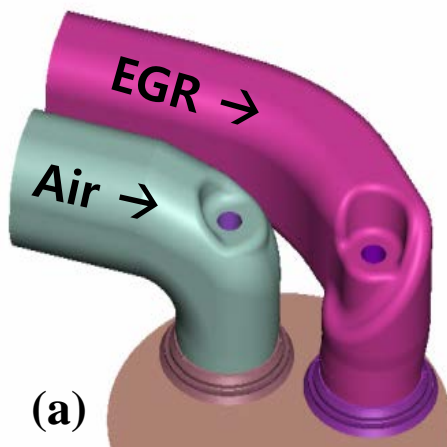


Figure 4.2.4 Geometries of the intake ports (a) helix shape (b) non-helix shape.

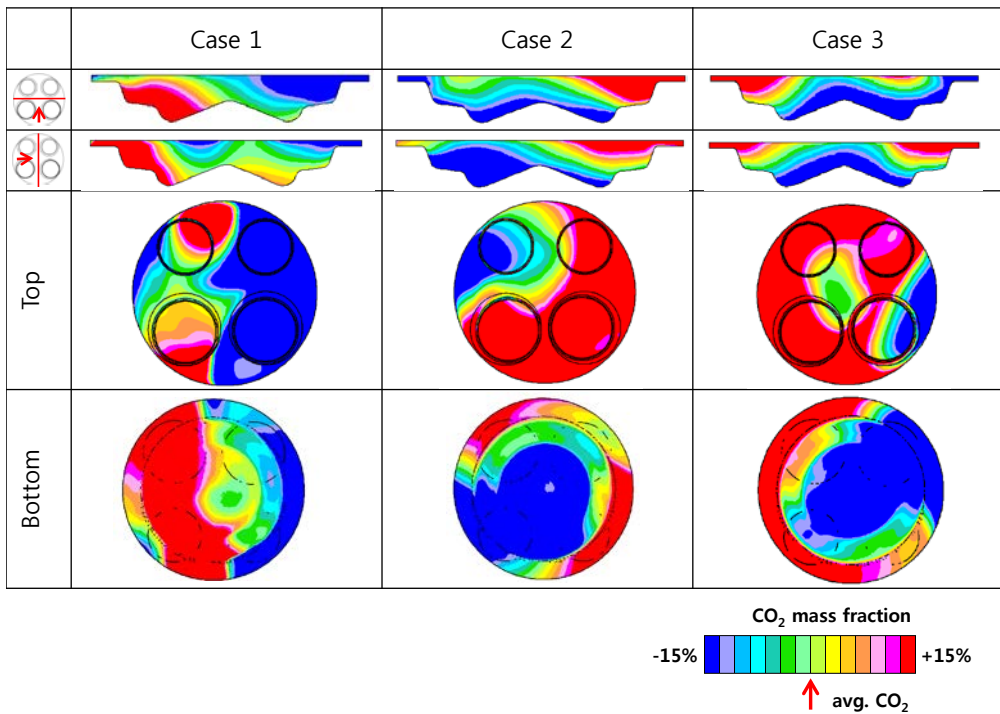


Figure 4.2.5 CO₂ (EGR) distributions at 10 ° BTDC (helix shape port).

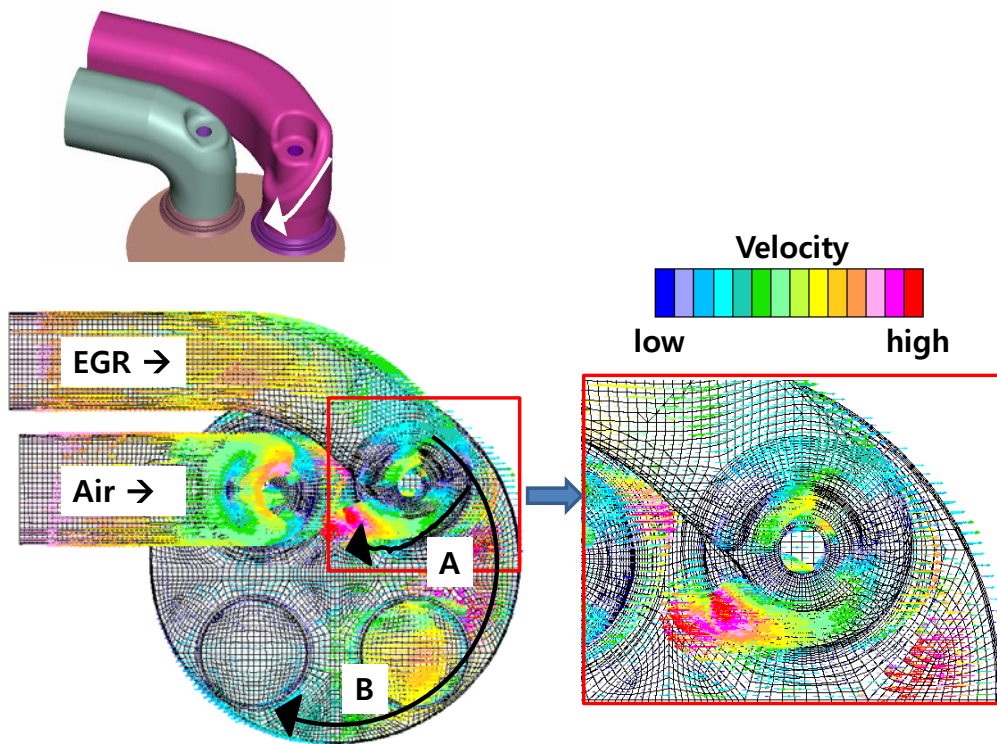


Figure 4.2.6 Velocity distribution at 270 ° BTDC (helix shape port).

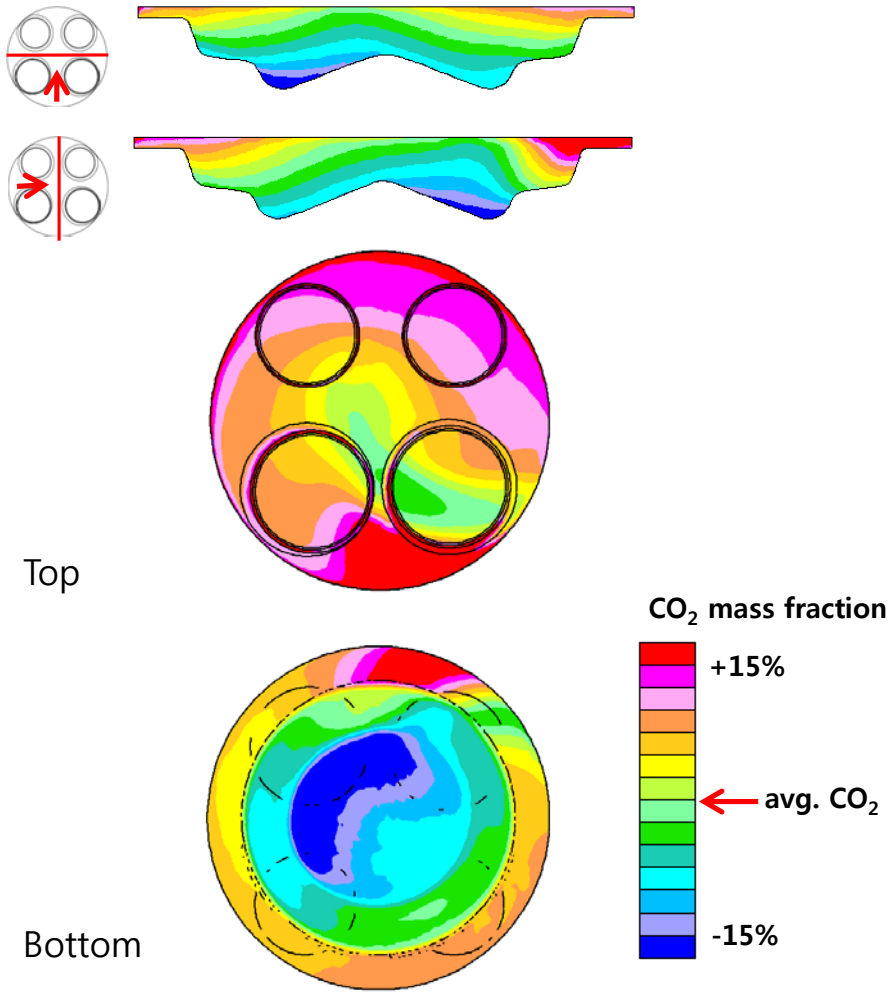


Figure 4.2.7 CO₂ (EGR) distributions at 10 ° BTDC (non-helix shape port).

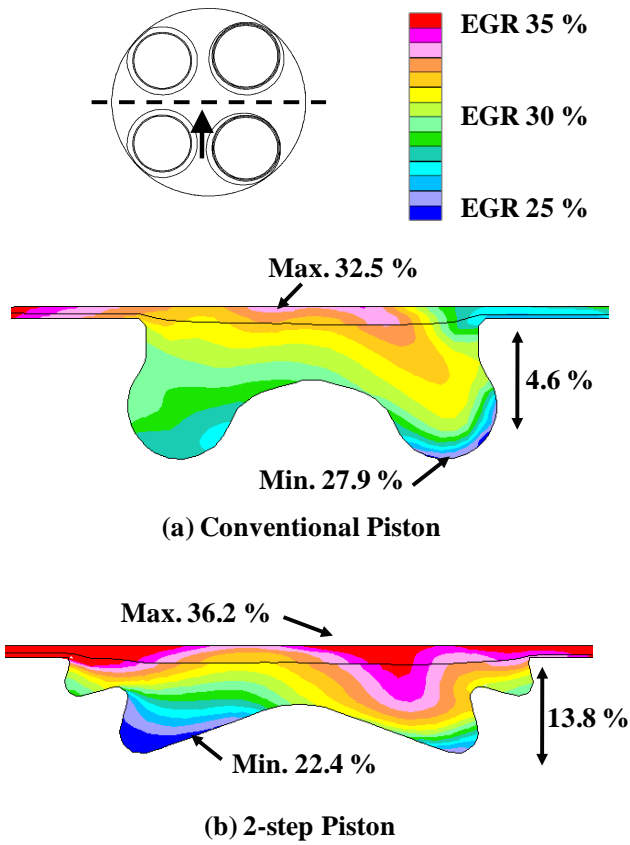


Figure 4.2.8 EGR distributions of (a) conventional piston and (b) two-step piston [22, 90].

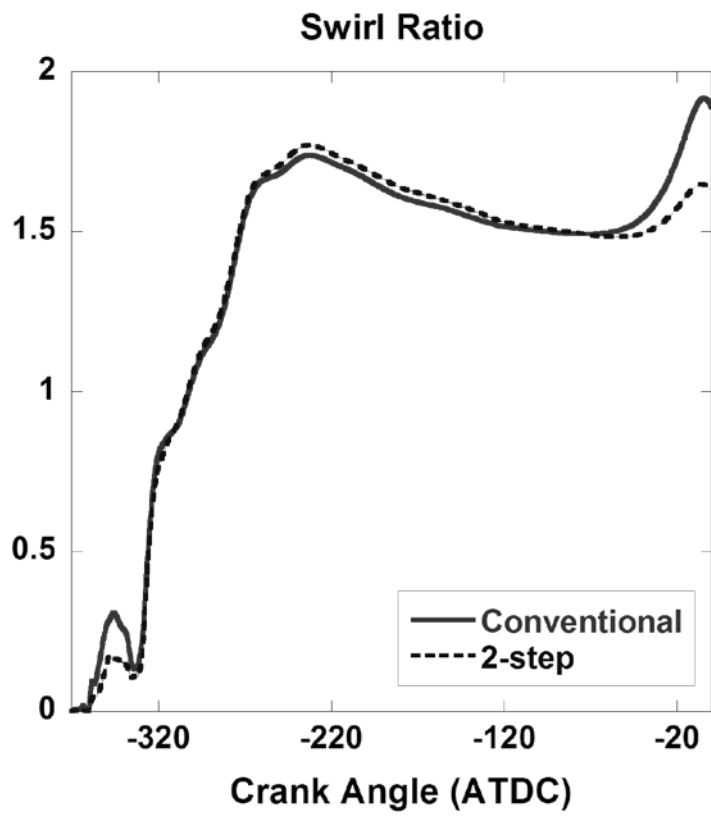


Figure 4.2.9 Comparison of the swirl ratio [23].

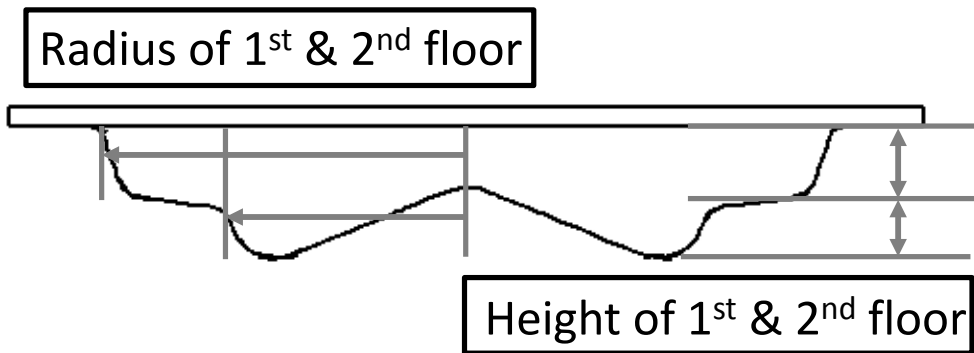


Figure 4.2.10 Parameters of the piston optimization.

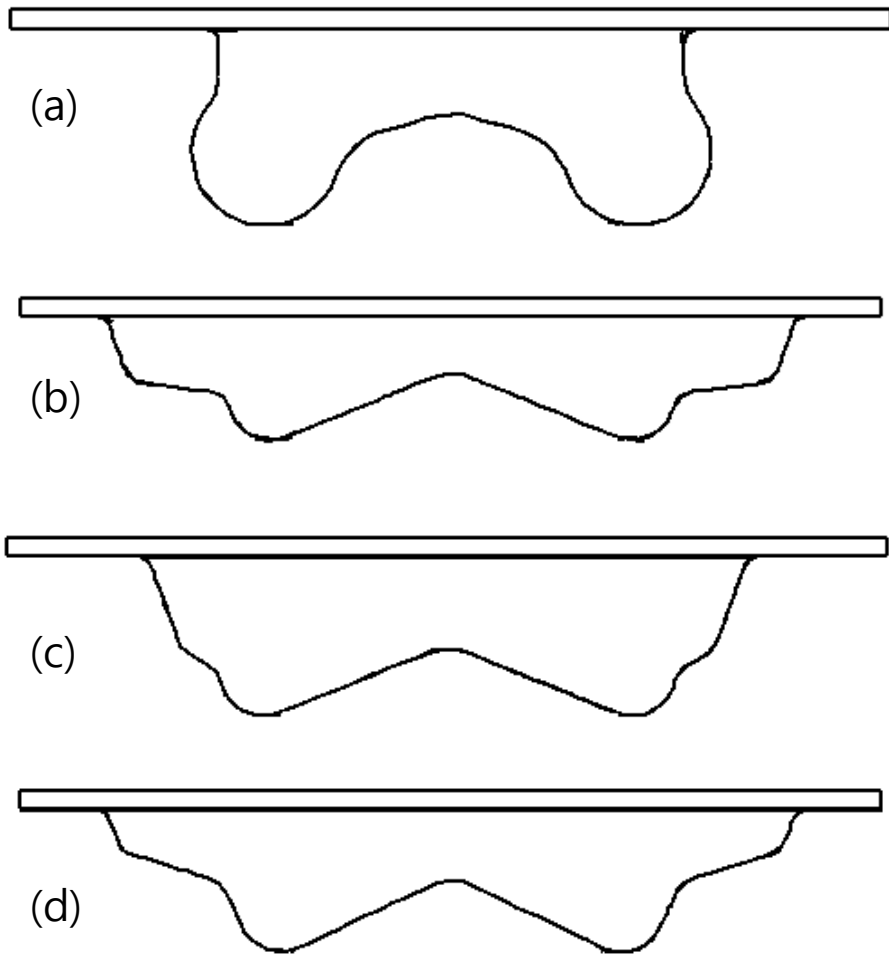


Figure 4.2.11 Piston Geometries (a) Standard Piston, (b) Piston A, (c) Piston B, and (d) Piston C.

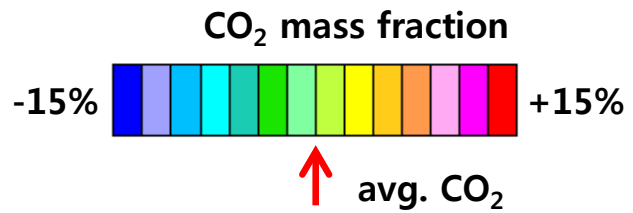
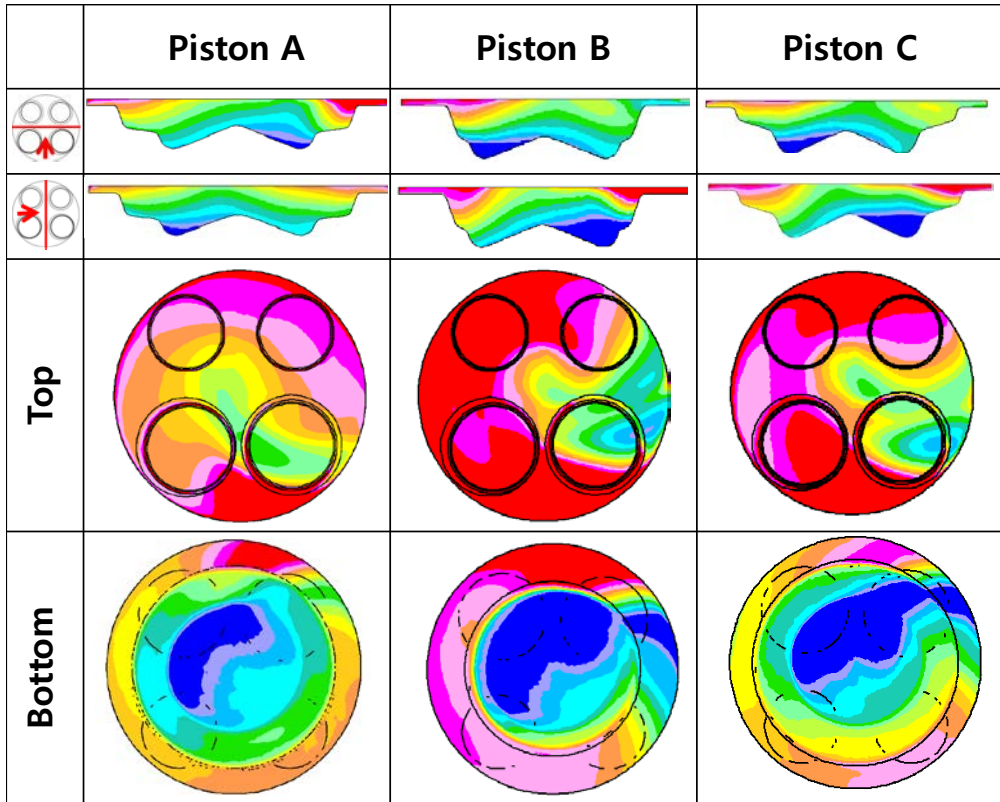


Figure 4.2.12 CO₂ (EGR) distributions at 10 ° BTDC.

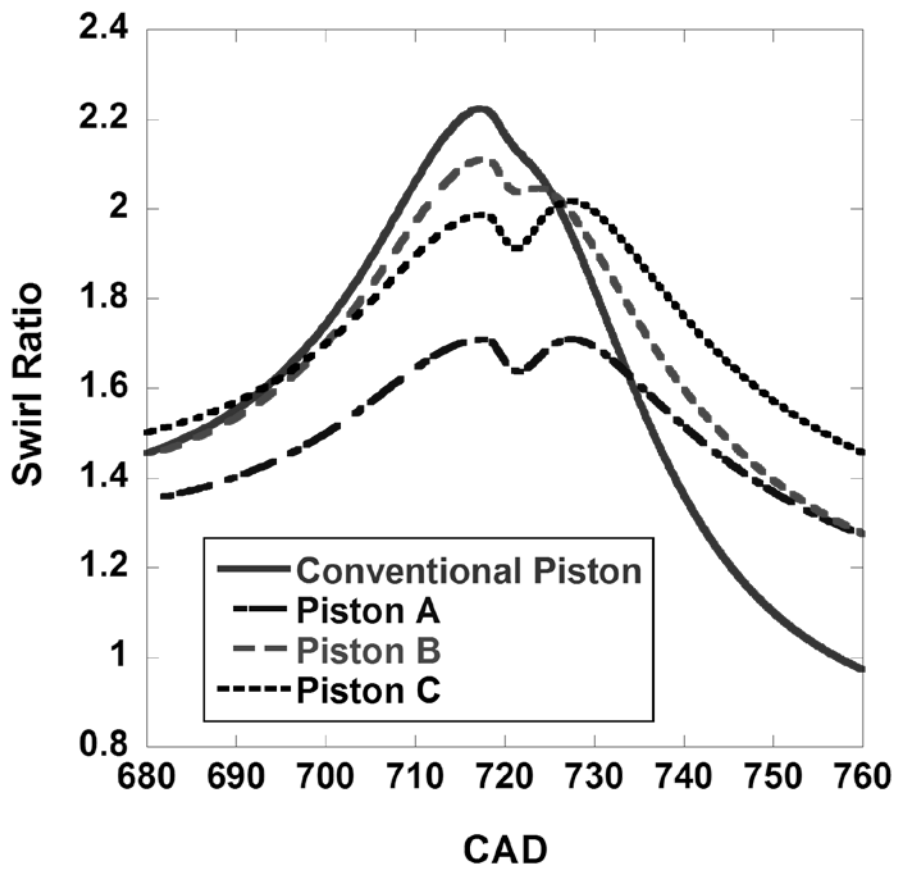


Figure 4.2.13 Comparisons of the swirl ratio.

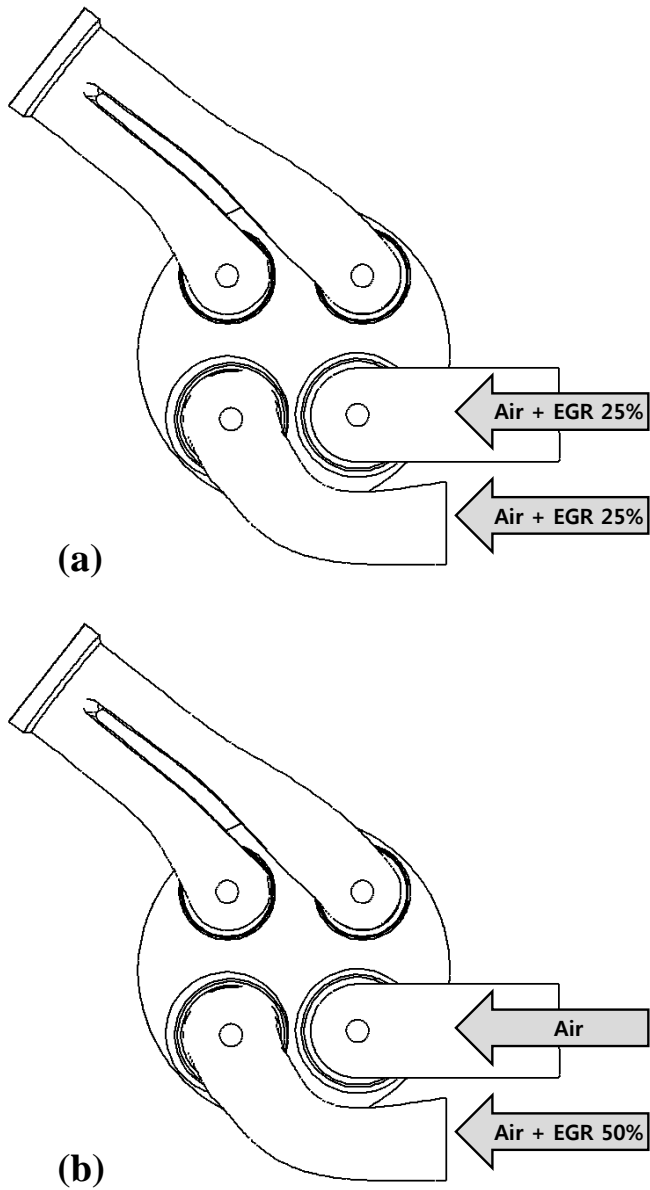


Figure 4.2.14 The method of Air and EGR supply: (a) B-EGR, (b) S-EGR.

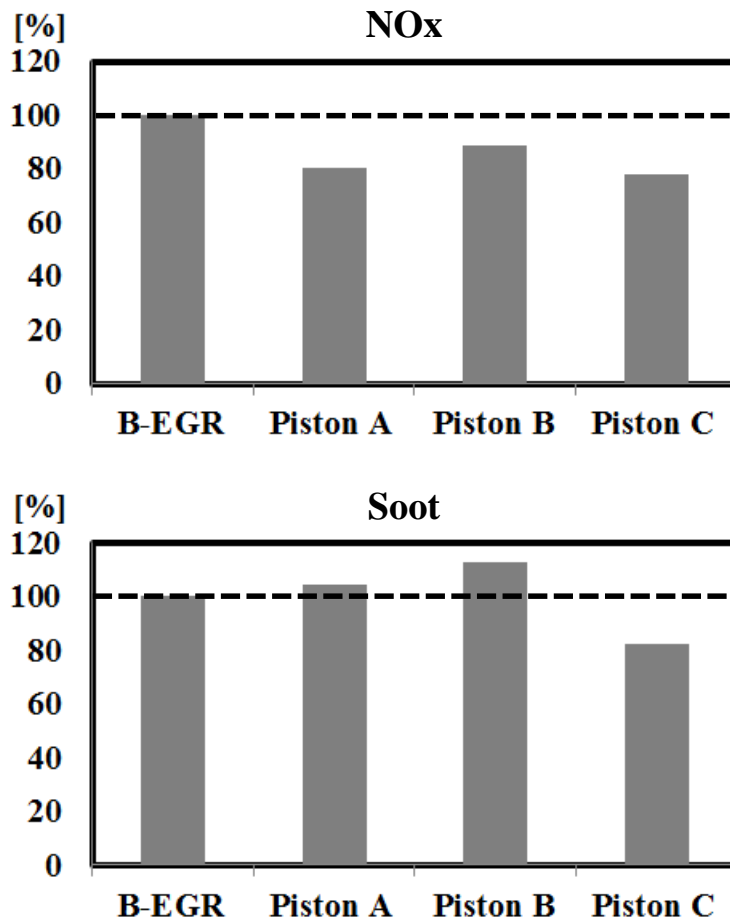


Figure 4.2.15 Effect of pistons on emission reduction.

4.3 Potential of In-cylinder EGR stratification

4.3.1 Computational Setup

To investigate the potential of the in-cylinder EGR stratification flow and combustion simulations were carried out using the FSE model and the optimized geometries. The non-helix type port and piston C which were described at Chapter 4.2 were used for simulation. The computational grid is shown in Figure 4.3.1 at BDC and it has approximately 684,200 cells at BDC and 77,400 cells at TDC. The calculation starts at the IVO, and the initial conditions are obtained from the experimental results. The turbulence, chemistry, emission, and break-up models are explained in detail at Chapter 2 and the sub-models for simulation are listed in Table 4.3.1 and the engine operating conditions are listed in Table 4.3.2.

The EGR supply method which explained Figure 4.2.14 was used and the overall EGR rates of B-EGR and S-EGR in the combustion chamber were same even the EGR gas distributions were different.

4.3.2 Results and Discussion

Figure 4.3.2 shows the prediction results of in-cylinder EGR distribution at 10° BTDC under 1500 rpm, 15 mg of fuel, and 25.0 % of external EGR rate. In case of B-EGR, the air and external EGR gas is supplied uniformly through the intake port assuming well-mixed condition. However, there exists non-uniformity of EGR distribution because of the residual gas, where locally high EGR region locates at the bottom of the combustion chamber and locally low EGR region exists at the top of it as shown in Figure 4.3.2 (a). The maximum EGR rate of B-EGR is 28.5 % and the minimum EGR rate of it is 25.5 %, where the overall EGR rate is 27.0 % (the overall EGR rate, 27.0 % is higher than supplied external EGR rate, because of

about 4 % of the residual gas fraction). Moreover, in case of S-EGR, the non-uniformity of EGR distribution increases as shown in Figure 4.3.2 (b) and the locally high EGR region locates the top of the combustion chamber in contrast to B-EGR. The maximum EGR rate of S-EGR is 32.3 % and the minimum EGR rate of it is 20.0 %, where the overall EGR rate is same with B-EGR. To simulate these non-uniform EGR distribution conditions, 4 zones and 5 flamelets were used for B-EGR and 12 zones and 13 flamelets were used for S-EGR.

Figure 4.3.3 shows pressure curves of B-EGR and S-EGR at 1500 rpm, 15 mg of fuel, and 25 % external EGR condition. Pressure curve of S-EGR is almost the same with B-EGR except the peak pressure. The maximum pressure of S-EGR is less than B-EGR by 1.3×10^5 Pa (1.8 % of the peak pressure). Figure 4.3.4 shows averaged temperature curves of B-EGR and S-EGR. The averaged in-cylinder temperature of S-EGR is lower than that of B-EGR during the combustion. In the case of S-EGR most of the combustion starts in the high EGR region as shown in Figure 4.3.2 (b), so the ignition delay is prolonged, and the peak of the cylinder pressure, temperature, and heat release rate are decreased. Therefore, NO_x reduction is achieved due to the locally low oxygen concentration in the combustion region and the decrease in the initial reaction rate, which decreases the peak cylinder pressure and combustion temperature. Figure 4.3.5 shows temperature distributions and Figure 4.3.6 shows NO distributions at 15 ° after SOI (10 ° ATDC). Because of locally high EGR region at the upper part of the combustion chamber, the temperature of S-EGR around the high EGR region is lower than B-EGR about 100 K. NO shows similar distribution with the temperature as NO formation is strongly affected by the burned gas temperature. For these reasons, the NO_x is reduced 22.0 % compared to the B-EGR as shown in Figure 4.3.7.

In case of soot mass, soot generation increases because of the locally high EGR region, but soot oxidation also increases at the end of reaction by mixing with the locally high oxygen region as shown in Figure 4.3.8. Therefore, 17.8 % of soot

mass reduction compared to the B-EGR was achieved as described in Figure 4.3.7. However, 4.5 % of soot number density (SND) was increased under S-EGR compared to B-EGR. It is because soot oxidation occurs at the surface of soot and reduces mass of soot particle but does not remove soot particle directly.

Furthermore, the robustness of the effect of in-cylinder EGR stratification was verified in the various EGR rate, injection timings, engine speeds, and loads. First, external EGR rate was increased to 35 % at 1500 rpm and 15 mg of fuel condition. Figure 4.3.9 shows NO_x and soot results under S-EGR compared with B-EGR. 27.3 % of NO_x was reduced while 4.9 % of soot was increased than B-EGR. In case of 35 % EGR, there is not less oxygen than 25 % EGR condition due to the high overall EGR rate; as a result soot oxidation is not enough during the expansion stroke as shown in Figure 4.3.10.

Second, the injection timing was changed from 7 ° BTDC to 3 ° BTDC at 1500 rpm, 15 mg of fuel, and 25 % of external EGR conditions. As shown in Figure 4.3.11 NO_x increases as SOI moves forward while soot decreases under both EGR conditions. Effect of NO_x reduction is biggest at 5 ° BTDC condition and effect of soot reduction is largest at 3 ° BTDC condition.

Last, the engine speed and load were changed from 1500 rpm and bmep 4 bar (15 mg of the fuel mass) to 2000 rpm and bmep 6 bar (23 mg of the fuel mass) under 25 % of external EGR condition. Figure 4.3.12 shows EGR distribution at 10 ° BTDC at 2000 rpm and bmep 6 bar condition. EGR distributions of 1500 rpm / bmep 4 bar (Figure 4.3.2 (b)) and 2000 rpm / bmep 6bar (Figure 4.3.12) show similar pattern but the degree of EGR stratification at 2000 rpm / bmep 6bar is less than 1500 rpm / bmep 4 bar. Therefore NO_x reduction is reduced from 22.0 % to 8.7 % while soot reduction is increased from 17.8 % to 32.9 % as shown in Figure 4.3.13.

Although the levels of emission reduction are different, NO_x and soot were simultaneously reduced under the stratified EGR condition. From these results, the potential of in-cylinder EGR stratification for the simultaneous NO_x and soot reduction was confirmed.

Table 4.3.1 The sub-models for CFD simulations

Description	Model [62]
CFD code	STAR-CD v.4.16
Turbulence	κ - ε RNG
Atomization	Reitz-Diwakar
Nozzle	Effective
Droplet break-up	Reitz
Droplet-wall interaction	Bai

Table 4.3.2 The conditions for calculation.

Description	Model
Engine Speed	1500, 2000 rpm
Overall EGR rate	25, 35 %
AFR	22
Inj. timing	3, 5, 7 ° BTDC
Inj. mass	15 mg, 23 mg

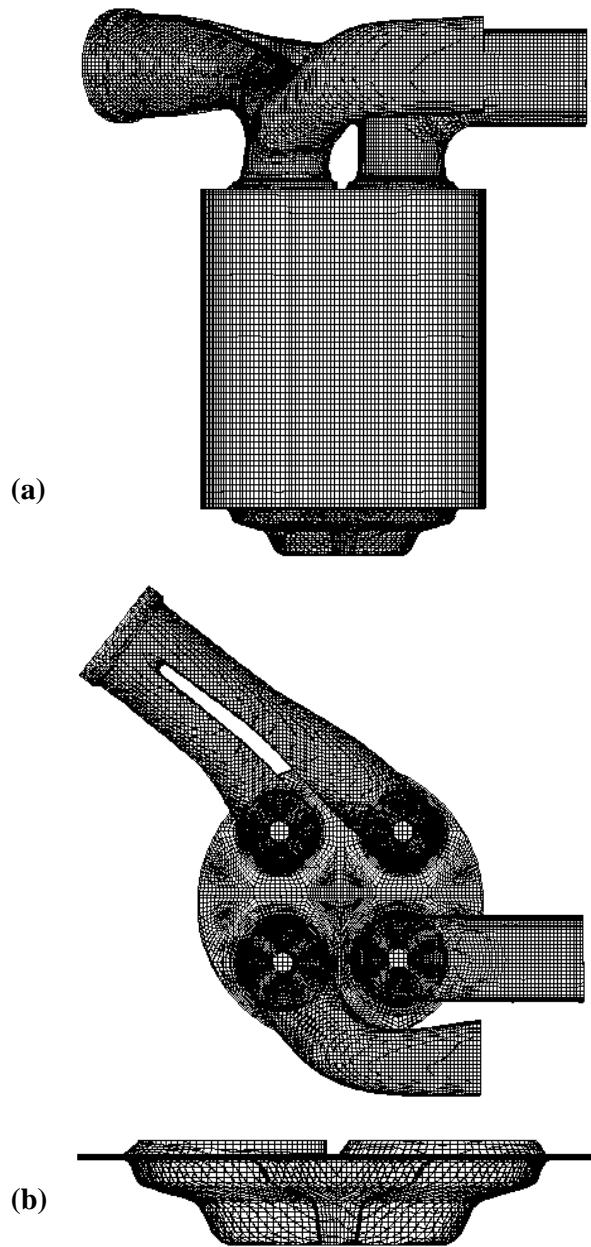
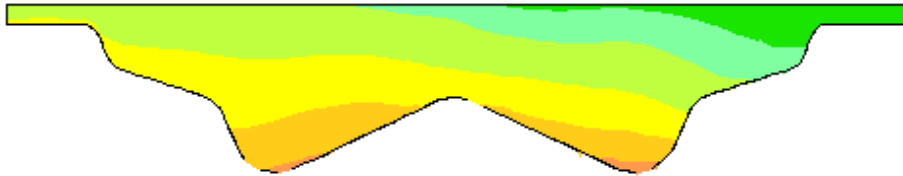
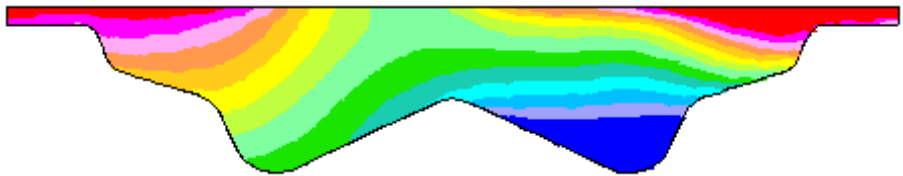


Figure 4.3.1 The optimized computational grid: (a) at BDC with intake and exhaust ports, (b) at TDC without ports.



(a) B-EGR



(b) S-EGR

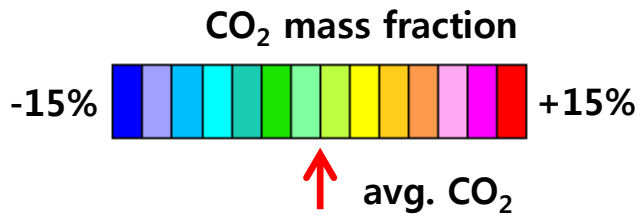


Figure 4.3.2 EGR distributions at 10 ° BTDC: (a) B-EGR, (b) S-EGR.

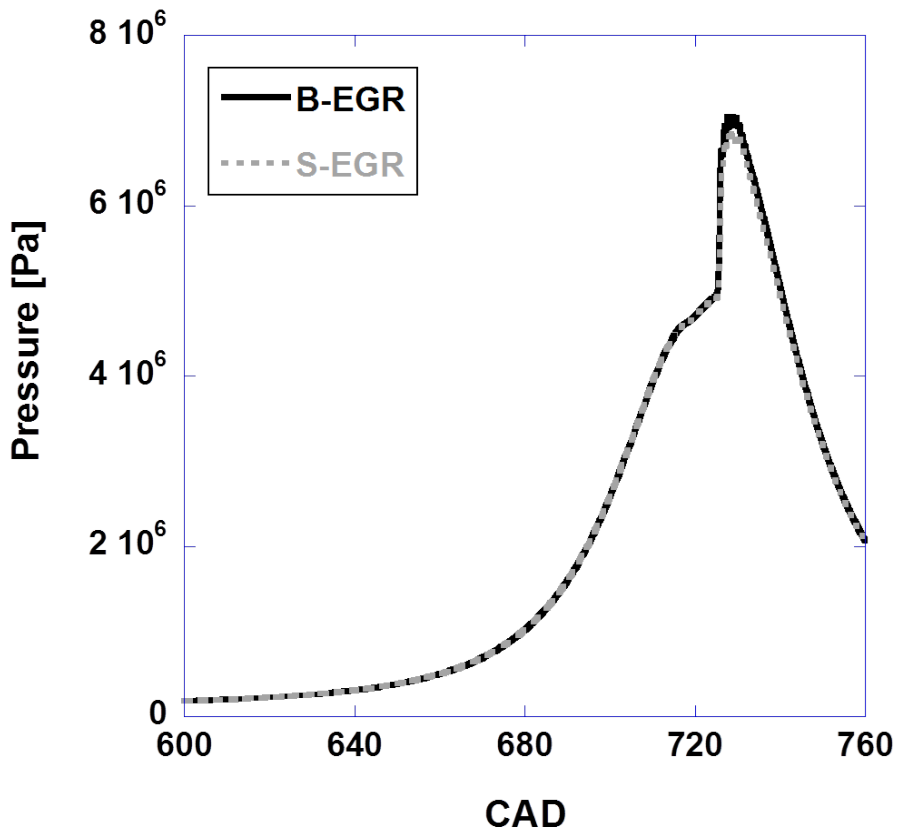


Figure 4.3.3 In-cylinder pressure curves of B-EGR and S-EGR.

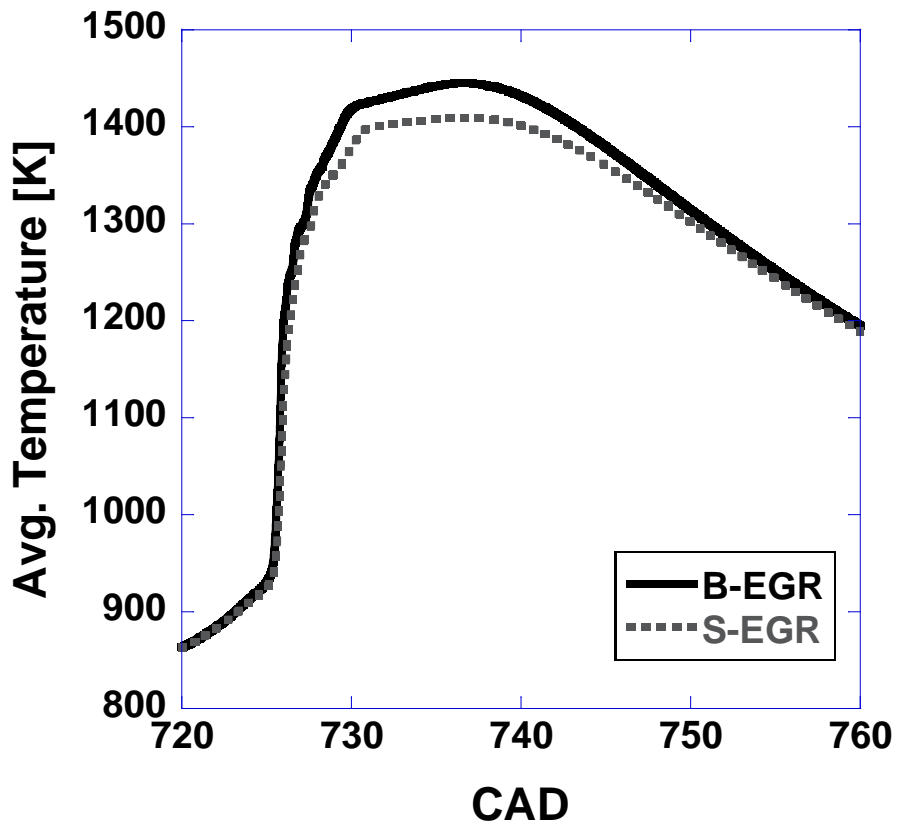
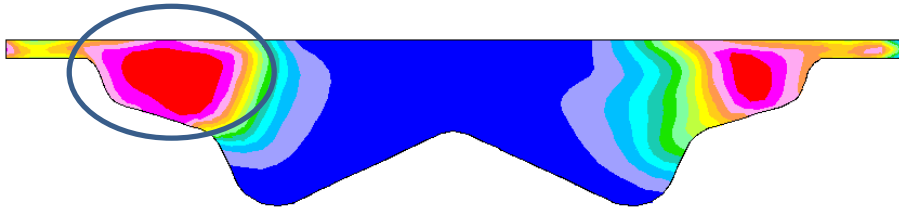
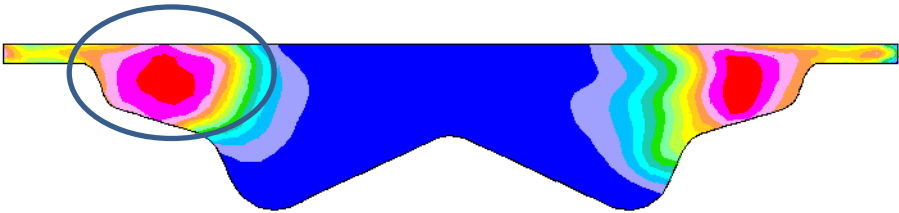


Figure 4.3.4 Averaged in-cylinder temperature curves of B-EGR and S-EGR.



(a) B-EGR



(b) S-EGR

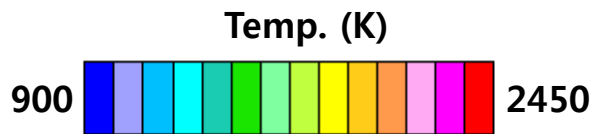
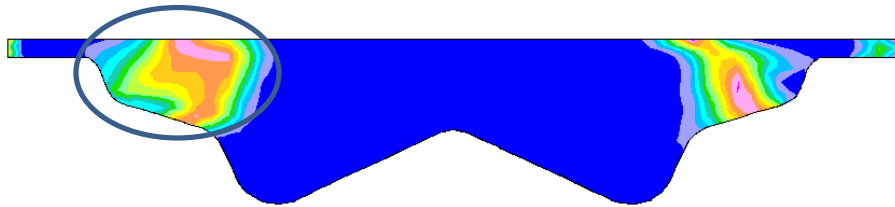
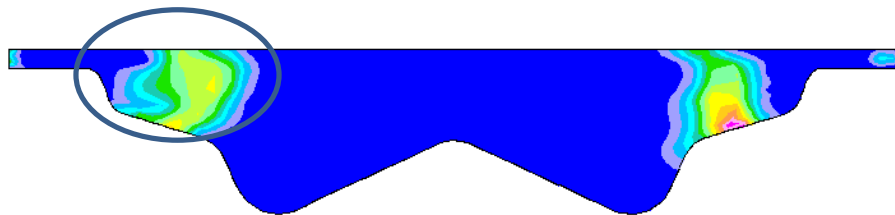


Figure 4.3.5 Temperature distributions at 15 ° after SOI (10° ATDC).



(a) B-EGR



(b) S-EGR

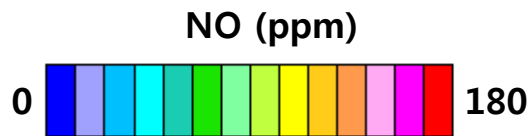


Figure 4.3.6 NO distributions at 15 ° after SOI (10° ATDC).

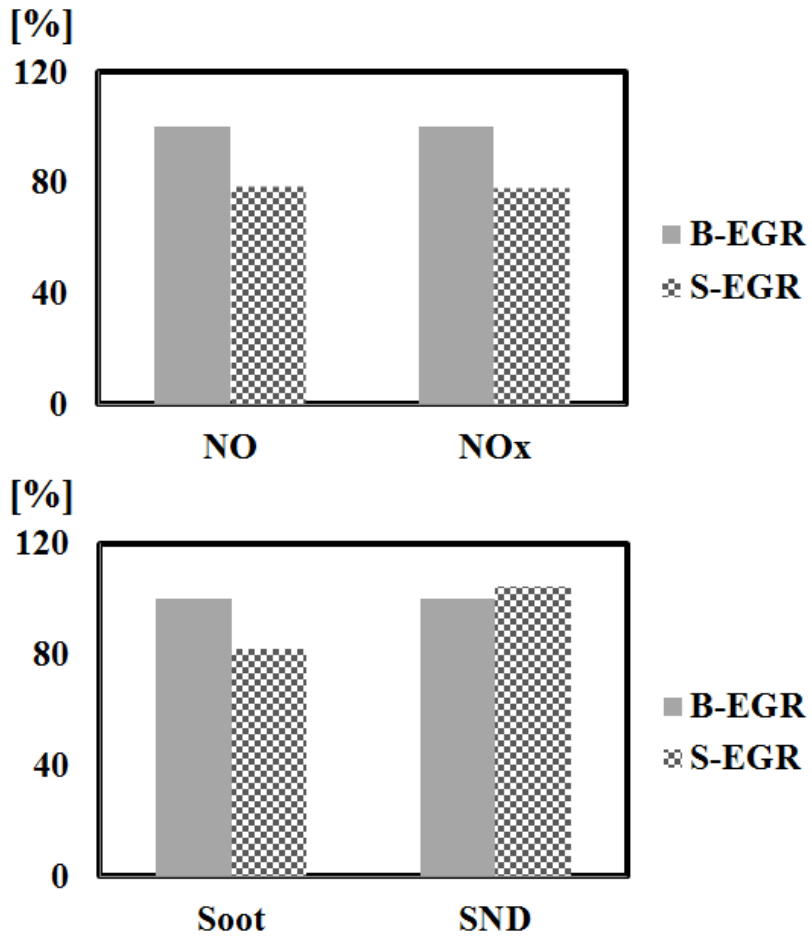


Figure 4.3.7 Comparison of predicted emissions of B-EGR and S-EGR at EGR 25 % condition.

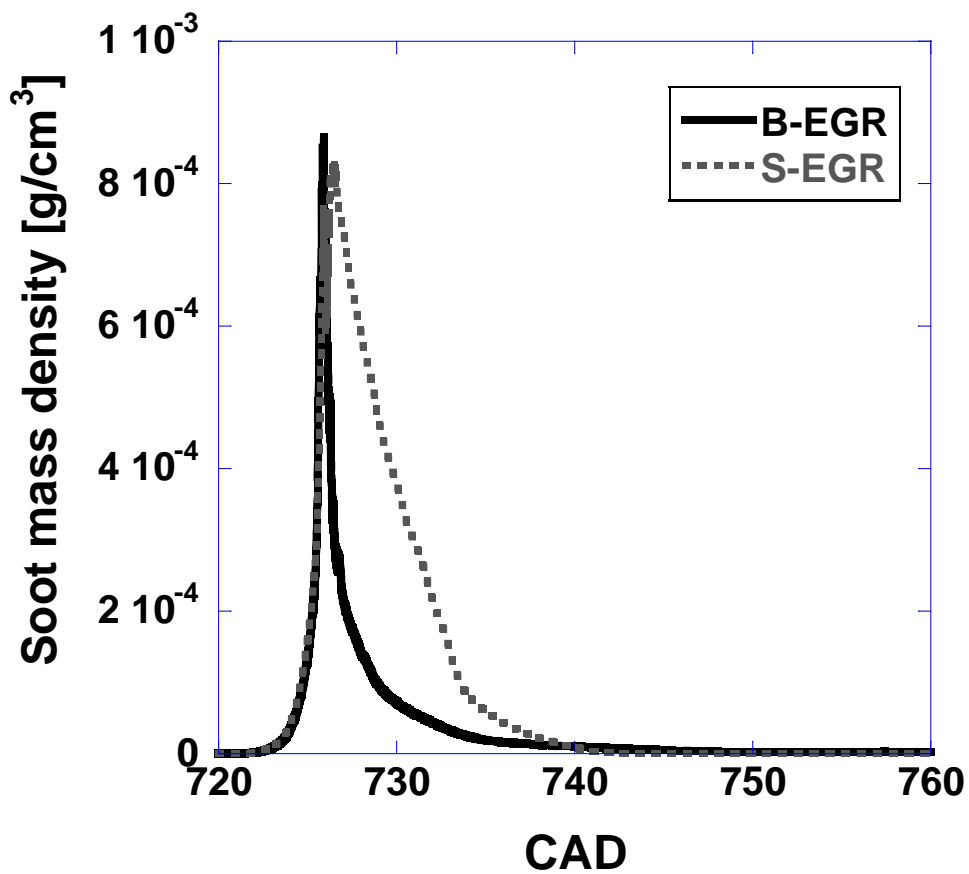


Figure 4.3.8 Soot mass density curves of B-EGR and S-EGR at EGR 25 % condition.

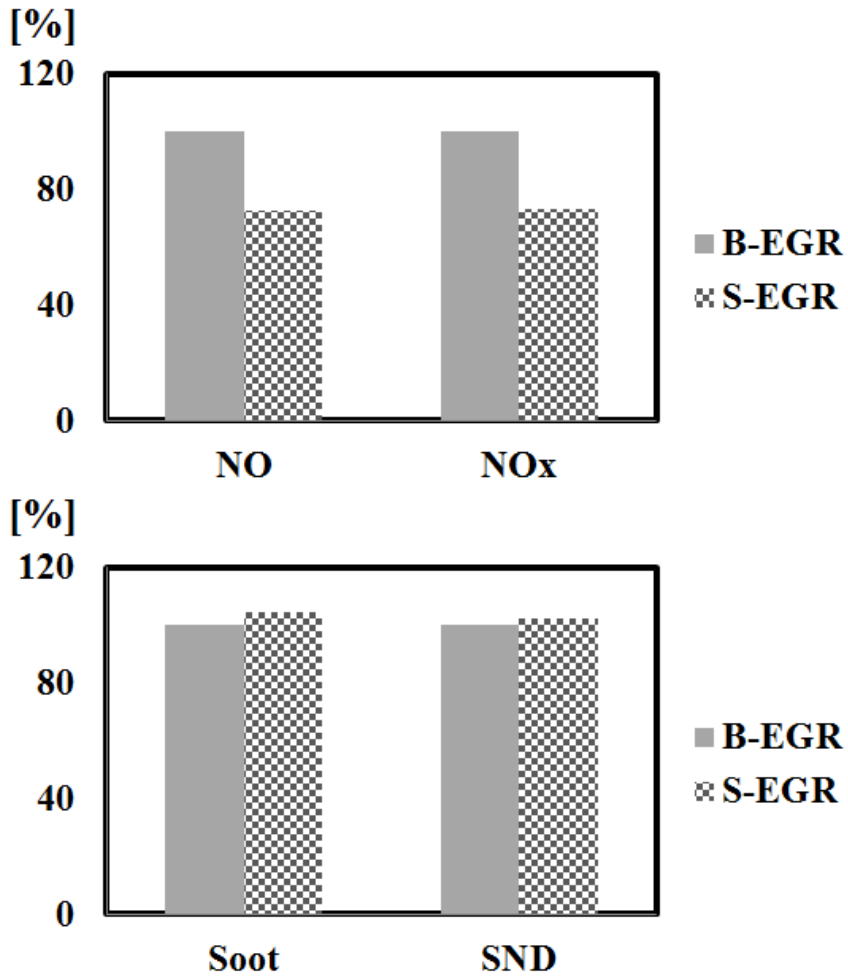


Figure 4.3.9 Comparison of predicted emissions of B-EGR and S-EGR at EGR 35 % condition.

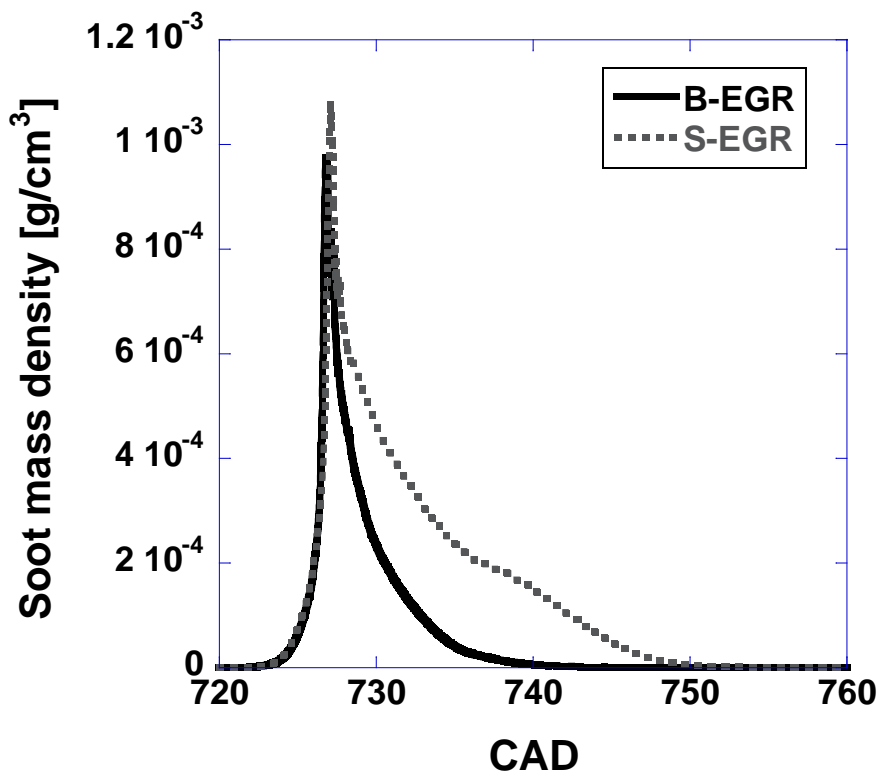


Figure 4.3.10 Soot mass density curves of B-EGR and S-EGR at EGR 35 % condition.

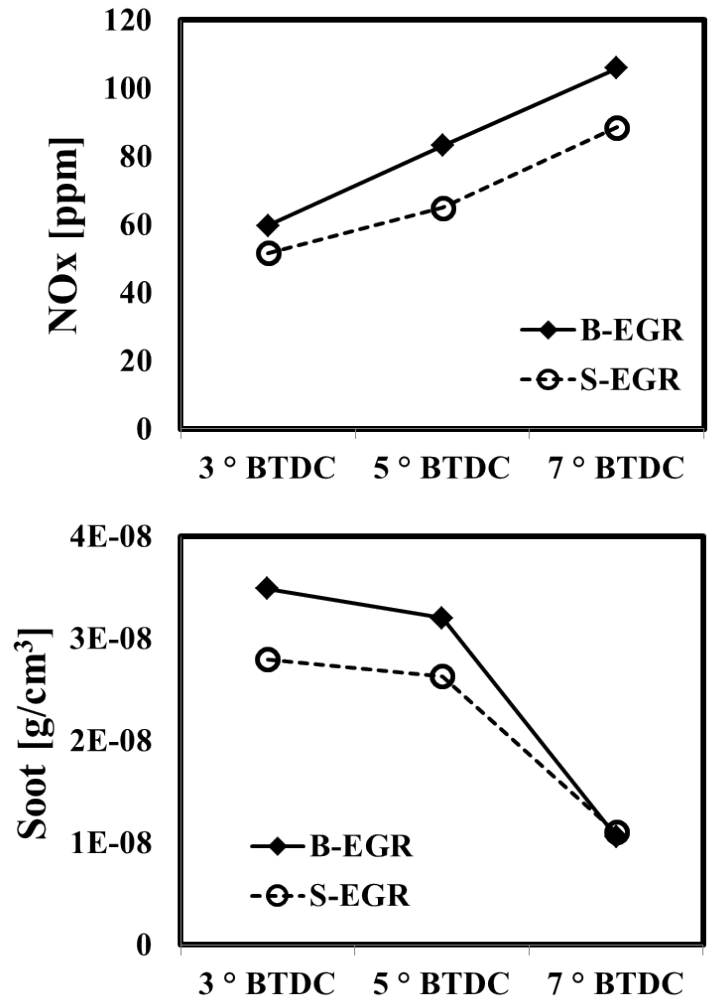


Figure 4.3.11 Comparison of predicted emissions of B-EGR and S-EGR under variable injection timings.

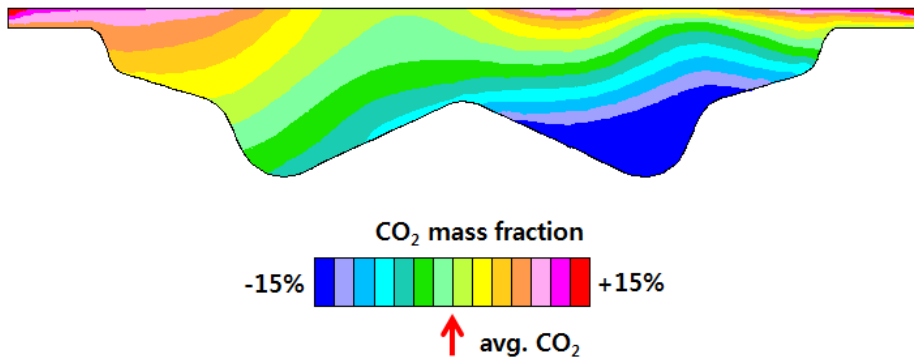


Figure 4.3.12 EGR distribution at 10 ° BTDC at S-EGR

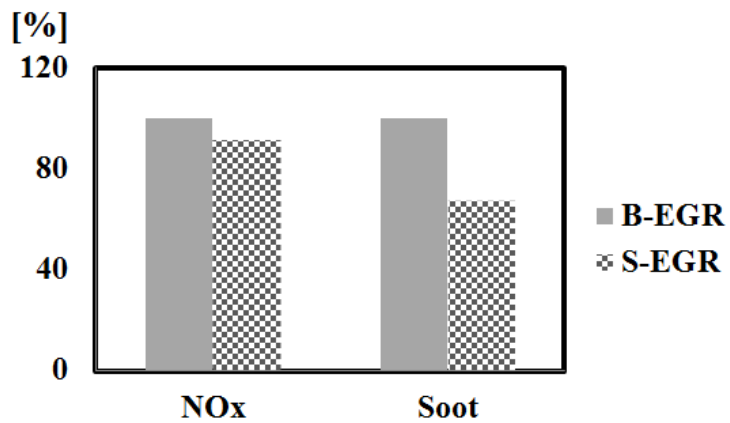


Figure 4.3.13 Comparison of predicted emissions of B-EGR and S-EGR under variable speed and load conditions.

Chapter 5. Conclusions

In this study, a new combustion model, Flamelet for Stratified EGR (FSE) model, was developed to consider the non-uniform or stratified in-cylinder gas distribution based on the chemical kinetics. Then, the FSE model was used to investigate the potential of in-cylinder EGR distributions.

The concept of the FSE model is utilizing multiple flamelet models based on the multi-zone concept. To describe this non-uniform gas distribution, the combustion chamber is divided into several zones by oxygen concentration at SOI. Then, the flamelet equations are solved at the boundary of each zone. Final species mass fraction of each cell is calculated by linear interpolation between two results from the adjacent boundaries.

The key point of this FSE model is to determine the number of zones and their boundary oxygen concentrations. The strategy for dividing zones should be optimized by considering both the computational cost and the accuracy. To find the optimal number of zones and the interval of boundary oxygen concentrations, simulations are carried out and the boundary oxygen concentration of each zones are varied by spaced 1 % to 0.01 %. And it is concluded that zone with 0.2 % of boundary oxygen concentration is a good standard of dividing. Then, the FSE model was validated under variable engine operating conditions including in-cylinder EGR stratification conditions and the model shows good agreement with the experimental results.

The FSE model not only has the advantages of the flamelet model for emission prediction but can consider the non-uniform EGR distribution, which cannot be described by using the flamelet model. The comparison results between the FSE model and the flamelet model show the importance of considering the non-uniform

EGR distribution during the emission prediction. Moreover, to study the potential of the in-cylinder EGR stratification, the FSE model should be used.

Then the potential of in-cylinder EGR stratification was studied by using the FSE model. The objective of the in-cylinder EGR stratification is to reduce the NO_x and soot simultaneously in a Diesel engine by separating the EGR gas and fresh air in the combustion chamber. The EGR gas has to be located where combustion occurs to reduce NO_x, and fresh air has to be placed at the other side of the combustion chamber to oxidize the soot during the expansion stroke. However, it is difficult to obtain desirable in-cylinder EGR distribution. Therefore, in this study the combustion system such as intake ports, chamfers, and a piston were optimized to get the suitable EGR distribution and to enhance the effect of in-cylinder EGR stratification.

To get desirable EGR distribution in the combustion chamber, the EGR gas should be located in the center and upper region of the combustion chamber and the air should be placed in the bottom region of it. Therefore, an air supply port was designed as a straight type port to send air in the bottom region of the combustion chamber. An EGR supply port was designed as a bended type port which has curvature to the swirl-direction to place EGR gas in the upper region with increasing a swirl motion there to reduce the eccentricity of the EGR distribution. The non-helix shape ports with the offset chamfer shows lower degree of the EGR stratification than the helix shape port, but it shows better EGR distribution than the helix shape port. The two-step pistons were also designed to maximize the effect of in-cylinder EGR stratification by obtaining a desirable EGR distribution pattern and injecting fuel into the high EGR region. The piston C shows good in-cylinder EGR distributions and high swirl ratio.

Finally, to investigate the potential of the in-cylinder EGR stratification for emission reduction flow and combustion simulations were carried out using the FSE model and the optimized geometries. The non-helix type port with the offset

chamfer and the piston C were used for simulation. In the case of S-EGR, most of the combustion starts in the high EGR region, so the ignition delay is prolonged, and the peak of the cylinder pressure, temperature, and heat release rate are decreased. NO_x reduction is achieved due to the locally high EGR gas in the combustion region as the locally high EGR gas decrease the oxygen concentration, initial reaction rate, and combustion temperature. For these reasons, the NO_x is reduced 22.0 % compared with the B-EGR under 1500 rpm, bmep 4 bar, and 25 % external EGR conditions. In case of soot mass, soot generation increases because of the locally high EGR region, but soot oxidation also increases at the end of reaction by mixing with the locally high oxygen region. Therefore, 17.8 % of soot mass reduction compared to the B-EGR was achieved. Moreover, the robustness of the effect of in-cylinder EGR stratification was verified under the various injection timings, engine speeds, and roads. Although the levels of emission reduction are different, NO_x and soot were simultaneously reduced under the stratified EGR condition. From these results, the potential of in-cylinder EGR stratification for the simultaneous NO_x and soot reduction was confirmed.

Bibliography

- [1] Badami M, Mallamo F, Millo F, Rossi E. Influence of multiple injection strategies on emissions, combustion noise and BSFC of a DI common rail diesel engine. SAE paper, 2002-01-0503. 2002.
- [2] Benajes J, Molina S, Garcia J. Influence of pre-and post-injection on the performance and pollutant emissions in a HD diesel engine. SAE paper, 2001-01-0526. 2001.
- [3] Chen SK. Simultaneous reduction of NO_x and particulate emissions by using multiple injections in a small diesel engine. SAE paper, 2000-01-3084. 2000.
- [4] Mori K, Matsuo S, Nakayama S, Shiino S, Kawatani T, Nakashima K, et al. Technology for environmental harmonization and future of the diesel engine. SAE Paper, 2009-01-0318. 2009.
- [5] Heywood JB. Internal combustion engine fundamentals. 1988.
- [6] Jacobs T, Assanis D, Filipi Z. The impact of exhaust gas recirculation on performance and emissions of a heavy-duty diesel engine. SAE paper, 2003-01-1068. 2003.
- [7] Ladommatos N, Abdelhalim S, Zhao H, Hu Z. The Dilution, Chemical, and Thermal Effects of Exhaust Gas Recirculation on Diesel Engine Emissions-Part 4: Effects of Carbon Dioxide and Water Vapour (971660). PROGRESS IN TECHNOLOGY. 2002;89:173-92.
- [8] Ladommatos N, Abdelhalim SM, Zhao H, Hu Z. Effects of EGR on heat release in diesel combustion. SAE paper, 980184. 1998.
- [9] Maiboom A, Tauzia X, Hétet JF. Influence of high rates of supplemental cooled EGR on NO_x and PM emissions of an automotive HSDI diesel engine using an LP EGR loop. International Journal of Energy Research. 2008;32(15):1383-98.
- [10] Nitu B, Singh I, Zhong L, Badreshany K, Henein N, Bryzik W. Effect of EGR on autoignition, combustion, regulated emissions and aldehydes in DI diesel engines. SAE paper, 2002-01-1153. 2002.
- [11] Lee K, Lee C, Ryu J, Kim H. An experimental study on the two-stage combustion characteristics of a direct-injection-type HCCI engine. Energy & fuels.

- 2005;19(2):393-402.
- [12] Lee Y, Huh K. Simulation of HCCI combustion with spatial inhomogeneities via a locally deterministic approach. *International Journal of Automotive Technology*. 2010;11(1):19-26.
- [13] Najt PM, Foster DE. Compression-ignited homogeneous charge combustion. SAE paper, 830264. 1983.
- [14] Thring R. Homogeneous-Charge Compression-Ignition(HCCI) Engines. SAE paper, 892068. 1989.
- [15] Akihama K, Takatori Y, Inagaki K, Sasaki S, Dean AM. Mechanism of the smokeless rich diesel combustion by reducing temperature. SAE paper, 2001-01-0655. 2001.
- [16] Kimura S, Aoki O, Kitahara Y, Aiyoshizawa E. Ultra-clean combustion technology combining a low-temperature and premixed combustion concept for meeting future emission standards. SAE paper, 2000-01-0200. 2001.
- [17] www.dieselnet.com.
- [18] www.seekingalpha.com.
- [19] Siewert RM, Krieger RB, Huebler MS, Baruah PC, Khalighi B, Wesslau M. Modifying an Intake Manifold to Improve Cylinder-to-Cylinder EGR Distribution in a DI Diesel Engine Using Combined CFD and Engine Experiments. SAE paper, 2001-01-3685. 2001.
- [20] Siewert RM, Krieger RB, Huebler MS, Baruah PC, Khalighi B, Wesslau M. Modifying an Intake Manifold to Improve Cylinder-to-Cylinder EGR Distribution in a DI Diesel Engine Using Combined CFD and Engine Experiments. SAE paper, 2001-01-3685. 2001:01-3685.
- [21] Fuyuto T, Nagata M, Hotta Y, Inagaki K, Nakakita K, Sakata I. In-cylinder stratification of external exhaust gas recirculation for controlling diesel combustion. *International Journal of Engine Research*. 2010;11(1):1-15.
- [22] W. Park SL, S. Choi, K. Min. Potential of in-cylinder exhaust gas recirculation stratification for combustion and emissions in diesel engines. *Proceedings of the Institution of Mechanical Engineers, Part D: Journal of Automobile Engineering*. 2012;226(4):547-59.

- [23] Park W, Lee S, Choi S, Min K. Study on the Effects of the In-Cylinder EGR Stratification on NO_x and Soot Emissions in Diesel Engines. SAE paper, 2011-24-0021. 2011.
- [24] Groves WN, Bjorkhaug M. Stratified exhaust gas recirculation in a SI engine. SAE paper, 860318. 1986.
- [25] Han SaC, W. K. Design and Demonstration of a Spark-Ignition Engine Operating in a Stratified-Egr Mode. SAE paper, 980122. 1998.
- [26] Jackson NS, Stokes, J., Lake, T. H., Sapsford, S. M., Heikal, M. and Denbratt, I. Understanding the Ccvs Stratified Egr Combustion System. SAE paper, 960837. 1996.
- [27] Xu M, Chen, G. S., Daniels, C. and Dong, M. Numerical Study on Swirl-Type High-Dilution Stratified EGR Combustion System. SAE paper, 2000-01-1949. 2000.
- [28] Choi S, Park W, Lee S, Min K, Choi H. Methods for in-cylinder EGR stratification and its effects on combustion and emission characteristics in a diesel engine. Energy. 2011.
- [29] Castagne M, Cheve E, Dumas J, Henriot S, Castagné-IFP M, Chevé-IFP E, et al. Advanced tools for analysis of gasoline directinjection engines. SAE paper, 2000-01-1903. 2000.
- [30] Ge H, Shi Y, Reitz R, Wickman D, Willems W. Engine development using multi-dimensional CFD and computer optimization. SAE paper, 2010-01-0360. 2010.
- [31] Sinha N, Cavallo P, Hosangadi A, Lee R. Efficient CFD Simulations for In-Cylinder Flows Using Hybrid Grids. SAE paper, 1999-01-1184. 1999.
- [32] Splitter D, Wissink M, Kokjohn S, Reitz R. Effect of Compression Ratio and Piston Geometry on RCCI Load Limits and Efficiency. SAE paper, 2012-01-0383. 2012.
- [33] Colin O, Benkenida A. The 3-zones extended coherent flame model (ECFM3Z) for computing premixed/diffusion combustion. Oil & gas science and technology. 2004;59(6):593-609.
- [34] Spalding DB. The combustion of liquid fuels. Symposium (International) on Combustion. 1953;4(1):847-64.
- [35] Magnussen BF, Hjertager BH. On mathematical modeling of turbulent combustion with special emphasis on soot formation and combustion. Symposium (International) on Combustion. 1977;16(1):719-29.

- [36] Abraham J, Bracco F, Reitz R. Comparisons of computed and measured premixed charge engine combustion. *Combustion and flame*. 1985;60(3):309-22.
- [37] Patterson MA, Kong S-C, Hampson GJ, Reitz RD. Modeling the effects of fuel injection characteristics on diesel engine soot and NOx emissions. SAE paper, 940523. 1994.
- [38] Colin O, Benkenida A, Angelberger C. 3D modeling of mixing, ignition and combustion phenomena in highly stratified gasoline engines. *Oil & gas science and technology*. 2003;58(1):47-62.
- [39] Béard P, Colin O, Miche M. Improved Modelling of DI Diesel Engines Using Sub-grid Descriptions of Spray and Combustion. SAE paper, 2003-01-0008. 2003.
- [40] Colin O, Pires da Cruz A, Jay S. Detailed chemistry-based auto-ignition model including low temperature phenomena applied to 3-D engine calculations. *Proceedings of the Combustion Institute*. 2005;30(2):2649-56.
- [41] Pitsch H, Barths H, Peters N. Three-Dimensional Modeling of NOx and Soot Formation in DI-Diesel Engines Using Detailed Chemistry Based on the Interactive Flamelet Approach. SAE paper, 9602057. 1996.
- [42] Park W, Lee J, Min K, Yu J, Park S, Cho S. Prediction of real-time NO based on the in-cylinder pressure in Diesel engines. *Proceedings of the Combustion Institute*. 2012.
- [43] Priesching P, Ramusch G, Ruetz J, Tatschl R. 3D-CFD Modeling of Conventional and Alternative Diesel Combustion and Pollutant Formation—A Validation Study. SAE Paper, 2007-01-1907. 2007.
- [44] Shi X, Li G. Numerical Simulation of Combustion Process for DI Diesel Engine Based on Coherent Flame Model. *Vehicle Engine*. 2007;170(4).
- [45] Shi X, Li G, Zhou L. DI diesel engine combustion modeling based on ECFM-3Z model. SAE paper, 2007-01-4138. 2007:01-4138.
- [46] Peters N. Laminar diffusion flamelet models in non-premixed turbulent combustion. *Progress in Energy and Combustion Science*. 1984;10(3):319-39.
- [47] Pitsch H, Wan YP, N. P. Numerical Investigation of Soot Formation and Oxidation under Diesel Engine Conditions. SAE paper, 952357. 1995.
- [48] Wan Y, Pitsch H, Peters N. Simulation of autoignition delay and location of fuel sprays

- under diesel-engine relevant conditions. SAE paper, 971590. 1997.
- [49] Hergart C, Barths H, Peters N. Modeling the combustion in a small-bore diesel engine using a method based on representative interactive flamelets. SAE paper, 1999-01-3550. 1999.
- [50] Hasse C, Bikas G, Peters N. Modeling DI-diesel combustion using the eulerian particle flamelet model (EPFM). SAE paper, 2000-01-2934. 2000.
- [51] Hasse CW. A two-dimensional flamelet model for multiple injections in diesel engines: Cuvillier Verlag, 2004.
- [52] Hasse C, Peters N. A two mixture fraction flamelet model applied to split injections in a DI diesel engine. *Proceedings of the Combustion Institute*. 2005;30(2):2755-62.
- [53] Lim J, Lee S, Min K. Combustion Modeling of Split Injection in HSDI Diesel Engines. *Combustion Science and Technology*. 2010;183(2):180-201.
- [54] Lim J. A Study on the Combustion Behavior of Multiple Injection in HSDI Diesel Engine Using Simplified Two-dimensional Flamelet Model. South Korea: Seoul National University, 2007.
- [55] Barths H, Antoni C, Peters N. Three-dimensional simulation of pollutant formation in a DI-diesel engine using multiple interactive flamelets. SAE paper, 982459. 1998.
- [56] Felsch C, Gauding M, Hasse C, Vogel S, Peters N. An extended flamelet model for multiple injections in DI Diesel engines. *Proceedings of the Combustion Institute*. 2009;32(2):2775-83.
- [57] Hamosfakidis V. A two conserved scalar model for HCCI and PPCI engine applications: University of Michigan, 2007.
- [58] Hamosfakidis V, Kobiera A, Assanis DN. A Regenerative Multiple Flamelet Model for non-Premixed Combustion with non-Uniform EGR. Conference A Regenerative Multiple Flamelet Model for non-Premixed Combustion with non-Uniform EGR, Athens, Greece.
- [59] Zheng M, Reader GT, Hawley JG. Diesel engine exhaust gas recirculation—a review on advanced and novel concepts. *Energy Conversion and Management*. 2004;45(6):883-900.
- [60] Lee J, Lee S, Park W, Min K, Song HH, Choi H, et al. The development of real-time

- NOx estimation model and its application. SAE paper, 2013-01-0243. 2013.
- [61] CD-adapco. STAR-CD methodology 2011.
- [62] Warsi Z. Conservation form of the Navier-Stokes equations in general nonsteady coordinates. AIAA Journal. 1981;19:240-2.
- [63] Lee S. Modeling of Combustion and Emission Characteristics in a Dual-fuel Engine by Combining Diffusion and Premixed Combustion. Seoul, Korea: Seoul National University, 2013.
- [64] Yakhot V, Orszag SA. Renormalization group analysis of turbulence. I. Basic theory. Journal of scientific computing. 1986;1(1):3-51.
- [65] Yakhot V, Orszag S, Thangam S, Gatski T, Speziale C. Development of turbulence models for shear flows by a double expansion technique. Physics of Fluids A: Fluid Dynamics. 1992;4(7):1510-20.
- [66] Peters N. Laminar flamelet concepts in turbulent combustion. Conference Laminar flamelet concepts in turbulent combustion, vol. 21. Elsevier, p. 1231-50.
- [67] Peters N, Williams F. The asymptotic structure of stoichiometric methane-air flames. Combustion and Flame. 1987;68(2):185-207.
- [68] Hergart C, Peters N. Applying the representative interactive flamelet model to evaluate the potential effect of wall heat transfer on soot emissions in a small-bore direct-injection diesel engine. Journal of engineering for gas turbines and power. 2002;124:1042.
- [69] Peters N, Williams FA. Lift-off characteristics of turbulent jet diffusion flames. AIAA Pap;(United States). 1982;82(CONF-820106-).
- [70] Barths H, Hasse C, Peters N. Computational fluid dynamics modelling of non-premixed combustion in direct injection diesel engines. International Journal of Engine Research. 2000;1(3):249-67.
- [71] Peters N. Four lectures on turbulent combustion. Aachen, Germany 1997.
- [72] Jia M, Peng Z, Xie M. Evaluation of Breakup Models and Application to the Mixture Preparation Process for Diesel HCCI Engines. SAE paper, 2008-01-0023. 2008.
- [73] Nicholls J. Stream and droplet breakup by shock waves. NASA SP-194. 1972:126-8.
- [74] Reitz R, Diwaker R. Effect of drop breakup on fuel sprays. SAE paper, 860469. 1986.

- [75] Patel A, Kong S-C, Reitz RD. Development and Validation of a Reduced Reaction Mechanism for HCCI Engine Simulations. SAE paper, 2004-01-0558. 2004.
- [76] Seiser R, Pitsch H, Seshadri K, Pitz W, Gurran H. Extinction and autoignition of n-heptane in counterflow configuration. Proceedings of the Combustion Institute. 2000;28(2):2029-37.
- [77] Kong S-C, YONG S, Rietz RD. Modeling diesel spray flame liftoff, sooting tendency, and NOx emissions using detailed chemistry with phenomenological soot model. Journal of engineering for gas turbines and power. 2007;129(1):245-51.
- [78] Smith GP, Golden DM, Frenklach M, Moriarty NW, Eiteneer B, Goldenberg M, et al. <http://www.me.berkeley.edu/gri-mech>. 2000.
- [79] Turns SR. An introduction to combustion. New York: McGraw-hill, 2000.
- [80] Tree DR, Svensson KI. Soot processes in compression ignition engines. Progress in Energy and Combustion Science. 2007;33(3):272-309.
- [81] Ranzi E, Sogaro A, Gaffuri P, Pennati G, Westbrook C, Pitz W. A new comprehensive reaction mechanism for combustion of hydrocarbon fuels. Combustion and flame. 1994;99(2):201-11.
- [82] Curran HJ, Gaffuri P, Pitz W, Westbrook C. A comprehensive modeling study of iso-octane oxidation. Combustion and flame. 2002;129(3):253-80.
- [83] Curran H, Pitz W, Westbrook C, Callahan G, Dryer F. Oxidation of automotive primary reference fuels at elevated pressures. Conference Oxidation of automotive primary reference fuels at elevated pressures, vol. 27. Elsevier, p. 379-87.
- [84] Flynn PF, Durrett RP, Hunter GL, zur Loye AO, Akinyemi O, Dec JE, et al. Diesel combustion: an integrated view combining laser diagnostics, chemical kinetics, and empirical validation. SAE paper 1999-01-0509. 1999.
- [85] Westbrook C, Pitz W, Boercker J, Curran H, Griffiths J, Mohamed C, et al. Detailed chemical kinetic reaction mechanisms for autoignition of isomers of heptane under rapid compression. Proceedings of the combustion institute. 2002;29(1):1311-8.
- [86] Westbrook CK, Dryer FL. Chemical kinetic modeling of hydrocarbon combustion. Progress in Energy and Combustion Science. 1984;10(1):1-57.
- [87] Appel J, Bockhorn H, Frenklach M. Kinetic modeling of soot formation with detailed

- chemistry and physics: laminar premixed flames of C_2 hydrocarbons. *Combustion and Flame*. 2000;121(1):122-36.
- [88] Bockhorn H. Soot formation in combustion(mechanisms and models). Springer series in chemical physics. 1994.
- [89] Tao F, Reitz RD, Foster DE, Liu Y. Nine-step phenomenological diesel soot model validated over a wide range of engine conditions. *International Journal of Thermal Sciences*. 2009;48(6):1223-34.
- [90] Choi S. The Effects of In-Cylinder EGR Stratification on Combustion and Emission Characteristics in a Diesel Engine. Seoul, Korea: Seoul National University, 2010.
- [91] Brandl F R, Cartellieri W, Dent JC. Turbulent air flow in the combustion bowl of a DI diesel engine and its effect on engine performance. SAE paper, 790040. 1979.
- [92] Prasad B, Sharma C, Anand T, Ravikrishna R. High swirl-inducing piston bowls in small diesel engines for emission reduction. *Applied Energy*. 2011;88(7):2355-67.
- [93] Payri F, Benajes J, Margot X, Gil A. CFD modeling of the in-cylinder flow in direct-injection Diesel engines. *Computers & fluids*. 2004;33(8):995-1021.
- [94] T S, Y D, N U, N I. Effects of combustion chamber geometry on diesel combustion. SAE paper, 861186. 1986.
- [95] Hiroshi Ogawa YM, Shuji Kimura, and Junichi Kawashima. Three-Dimensional Computation of the Effects of the Swirl Ratio in Direct-Injection Diesel Engines on NO_x and Soot Emissions. SAE paper, 961125. 1996.
- [96] Michael J. Bergin RDR, Seungmook Oh, Paul C. Miles, Leif Hildingsson, and Anders Hultqvist. Fuel Injection and Mean Swirl Effects on Combustion and Soot Formation in Heavy Duty Diesel Engines. SAE paper, 2007-01-0912. 2007.
- [97] Jaichandar S, Annamalai K. Effects of open combustion chamber geometries on the performance of pongamia biodiesel in a DI diesel engine. *Fuel*. 2012;98:272-9.

초 록

환경에 대한 관심이 높아지고 배기 규제 관련 법규가 강화됨에 따라 디젤 엔진의 배기 배출물, 특히, 질소산화물과 입자상 물질을 동시에 저감하기 위해 다양한 연구들이 진행되고 있다. 엔진에서 발생하는 배출물을 줄이기 위한 신연소 기법으로는 저온 연소, 연소실 내 배기재순환가스 성층화 등이 있다. 다양한 연구 방법 중에서도 3 차원 전산유체해석을 활용한 연구방법은 실험에서 직접적으로 관측이 어려운 연소 과정에 대한 모사가 가능하기 때문에, 신연소 기법 연구에 있어 중요한 부분을 차지하고 있다.

3 차원 전산유체해석을 이용하여 디젤 엔진 신연소 기법의 배출물 저감 가능성에 대한 연구를 하기 위해서는 배출물의 생성을 정확하게 예측하는 것이 필요하다. 디젤 엔진에서 배출물 생성을 정확하게 예측하기 위해서는 배출물 생성에 영향을 미치는 연소실 내부의 국부적인 당량비 분포, 연료 및 배출물의 생성에 관련된 화학반응에 대한 고려가 가능한 연소모델을 사용해야 한다. 화염편(flamelet) 모델은 화학반응을 연동하여 연소를 계산할 수 있는 연소 모델로 디젤 엔진의 연소 및 배출물 생성을 계산하는 데 널리 사용되고 있는 모델이다. 그러나 화염편 모델은 배기재순환가스 성층화와 같은 연소실 내부의 불균일한 기체의 분포를 고려할 수 없는 한계가 있다. 따라서 본 연구에서는 화학 반응과 연동이 가능하며, 연소실 내의 불균일한 기체의 분포까지 고려할 수 있는 새로운 연소모델, Flamelet for Stratified EGR (FSE) model, 을 개발하였다. 또한, 개발된 FSE 모델을 활용하여 연소실내 배기 재순환가스 성층화기법의 질소산화물과 입자상 물질 동시 저감 가능성에 대해 연구하였다.

FSE 모델의 컨셉은 multi-zone 컨셉을 바탕으로 여러 개의 화염편 방정식을 사용하는 것이다. 연소실 내의 불균일한 배기재순환가스 분포를 모사하기 위하여, 연소실은 연료 분사 시작 시점의 산소 농도에

따라서 여러 개의 영역으로 나뉘어 지게 된다. 화염편 방정식은 각 영역의 경계에서 각각 계산되며, 화학종의 질량 분율은 인접한 두 경계에서 계산된 화염편 방정식의 결과를 선형적으로 보간하여 구할 수 있다. 따라서 FSE 모델은 기존 화염편 모델이 가지고 있는 장점들을 그대로 가지고 있을 뿐만 아니라, 기존 화염편 모델의 한계였던 연소실 내의 불균일한 배기재순환가스 분포까지도 모사가 가능하다. 본 연구에서는 화염편 모델을 이용한 해석 결과 및 실험 결과의 비교를 통하여 FSE 모델을 검증하였다.

또한 본 연구에서는 개발된 FSE 모델을 이용하여 연소실 내 배기재순환가스 성층화 기법의 배출물 저감 가능성에 대해 연구하였다. 연소실 내 배기재순환가스 성층화 기법은 연소실 내의 불균일한 배기재순환 가스 분포를 이용하여 디젤엔진에서 질소산화물과 입자상 물질을 동시에 저감하는 새로운 연소 기법이다. 두 배출물을 동시에 저감할 수 있는 적절한 배기재순환가스 분포를 얻기 위하여, 흡기 포트, 피스톤, 챔퍼 등의 형상을 최적화 하였다. 최적화된 연소시스템을 사용한 해석 결과, 배기재순환 가스 성층화 기법을 사용한 경우, 1500 rpm, bemp 4 bar, EGR 25 % 조건에서 22.0 % 의 질소산화물과 17.8 % 의 입자상 물질이 동시에 저감되는 것을 확인하였다. 또한 다양한 엔진 속도, 부하, 분사시기 등의 조건에 대해 연소실 내 배기재순환 가스 성층화 기법의 배출물 저감 가능성을 확인하였다.

주요어: 디젤 엔진, 질소산화물, 입자상 물질, 연소실 내 배기 재순환 가스 성층화, 불균일한 배기재순환 가스 분포, 화염편 모델

학번: 2007-22981